Universidade do Minho
Escola de Engenharia

Inês Adelaide Mota Cardoso

Development of shape-tunable Metal-Organic Framework nanosystems for cancer immunotherapy

Outubro de 2023

Development of shape-tunable Metal-Organic Framework nanosystems for cancer immunotherapy

Inês Adelaide Mota Cardoso

UMinho | 2023

Universidade do Minho
Escola de Engenharia
University of Groningen
University Medical Center Groningen

Inês Adelaide Mota Cardoso

Development of shape-tunabe Metal-Organic Framework nanosystems for cancer immunotherapy

Dissertação de Mestrado
Mestrado Integrado em Engenharia Biomédica
Mestrado em Engenharia Clínica

Trabalho efetuado sob a orientação do
Professora Doutora Lígia Raquel Marona Rodrigues
Universidade do Minho

Professor Doutor Hélder Almeida Santos
University Medical Center Groningen

Outubro de 2023

Direitos de Autor e Condições de Utilização do Trabalho por Terceiros

Este é um trabalho académico que pode ser utilizado por terceiros desde que respeitadas as regras e boas práticas internacionalmente aceites, no que concerne aos direitos de autor e direitos conexos. Assim, o presente trabalho pode ser utilizado nos termos previstos na licença abaixo indicada. Caso o utilizador necessite de permissão para poder fazer um uso do trabalho em condições não previstas no licenciamento indicado, deverá contactar o autor, através do RepositóriUM da Universidade do Minho.

Licença concedida aos utilizadores deste trabalho

Atribuição-NãoComercial-SemDerivações

CC BY-NC-ND

https://creativecommons.org/licenses/by-nc-nd/4.0/

Acknowledgments

Firstly, I would like to express my deepest gratitude to my supervisor in Groningen, Professor Doctor Hélder Almeida Santos, who always provided me with exceptional mentorship. His contributions and discussions enriched my knowledge and made this research experience rewarding. Secondly, I would like to acknowledge my supervisor in Portugal, Professor Doctor Lígia Rodrigues, and the Ph.D. students in Santos' Lab, Han Gao, and Ruoyu Cheng, for all the support and invaluable guidance throughout this journey. I am genuinely grateful for your patience, availability, and dedication. I would also like to thank the entire research group, as well as all the lab members and technicians for their valuable insights, camaraderie, and collaborative spirit. I'll be forever grateful and proud to work with such professional persons.

I want to extend my heartfelt gratitude to Maria, Micaela, and Soraia, my Erasmus family. I'm sure that we became way more than only colleagues at work, we became friends. From all the help that you gave me inside the lab to all the moments of happiness and friendship we spent outside of it, I'm forever grateful for that.

Catarina, you also deserve my words of gratitude. This experience changed my life, but it would be nothing without you by my side during those six months. It was amazing to spend that time with you. Thank you for all the times that you supported and understood me, and for all the good times we spent together far away from our home, you were my rock.

It's impossible to forget the wonderful friends I have made throughout the last five years who have welcomed me into their lives and made my own a lot brighter. Margarida, Manuel, Tiago, and Pedros, this journey would not have been possible without you.

Mom and Dad, I'm extremely grateful for all the love and support given to me for every decision I made so far and for providing me with everything I needed. There are no words to express how much it meant to me to have you by my side. I'm also very much thankful to my sister, Ana, for being present in all of my best and worst moments and for being a constant source of inspiration. To my lovely nephews, Manuel and José Rui, you are my inspiration to achieve greatness. Your love is what has gotten me through when I wanted to give up. Rui, thanks for your friendship, patience, comprehension, and love. You were crucial for both my academic and personal development, cheering me up when I was feeling down and celebrating each of my accomplishments.

Thanks, Groningen, you were not just a house, you became a home.

Lastly, I would like to give a special thanks to everyone else who, in any way was a part of this journey. You won't ever be forgotten.

"What we know is a drop, what we don't know is an ocean."

— Isaac Newton

Statement of Integrity

I hereby declare having conducted this academic work with integrity. I confirm that I have not used plagiarism or any form of undue use of information or falsification of results along the process leading to its elaboration. I further declare that I have fully acknowledged the Code of Ethical Conduct of the University of Minho.

Resumo

Título: Desenvolvimento de nanossistemas de Estrutura Metalo-Orgânica com forma ajustável para imunoterapia do cancro

O microambiente tumoral (TME) desempenha um papel crítico enquanto nicho ecológico essencial para o desenvolvimento e progressão do tumor, essencialmente devido à alta prevalência de células imunossupressoras, sendo os macrófagos associados a tumores (TAMs) os principais mediadores envolvidos no processo patológico do cancro. Os TAMs podem ser divididos em dois estados de polarização antagónicos: os macrófagos M1, pró-inflamatórios, e os M2, anti-inflamatórios. De acordo com as suas funções, os TAMs presentes no TME são geralmente classificados como macrófagos do tipo fenotípico M2. Nos últimos anos, mais atenção tem sido direcionada para a reestruturação e coordenação de um TME inflamatório, e os TAMs surgiram como um paradigma para a compreensão da ligação entre a inflamação e o cancro. Uma extensão dessa perspetiva terapêutica reuniu esforços destinados a repolarizar os TAMs, induzindo a alteração do fenótipo M2 para o fenótipo M1. Em resposta a vários estímulos do microambiente, os macrófagos podem adotar diferentes fenótipos e funções. As nanopartículas de estrutura metalo-orgânicas (MOF NPs) têm sido amplamente utilizadas como sistemas controlados de libertação de fármacos e agentes terapêuticos para o cancro, devido às suas excelentes propriedades intrínsecas, tais como a alta capacidade de ajuste da sua forma. No entanto, a resposta imune celular modulada pelo ajuste da forma das NPs ainda não está clara. Neste estudo, quatro formas diferentes de MOF NPs de cobre foram sintetizadas (agulha, hexágono, quadrado e esférica) através do ajuste das condições de síntese, seguindo-se uma avaliação sistemática das suas propriedades físico-químicas, biocompatibilidade e respetiva capacidade de reprogramação imunológica. As diferentes formas das Cu MOF NPs apresentaram respostas imunes distintas. As NPs em forma de quadrado e agulha promoveram a polarização dos macrófagos para o fenótipo M1, enquanto as NPs com forma esférica e hexagonal melhoraram o perfil de expressão de biomarcadores de macrófagos tipo-M2. De um modo geral, este estudo oferece *insights* práticos sobre as interações entre as NPs e as células imunes, o que pode ter potenciais implicações na imunoterapia antitumoral baseada em NPs.

Palavras-chave: Imunoterapia do Cancro; Estrutura Metalo-Orgânica; Nanopartículas com forma ajustável; Sistema Imunitário; Polarização de Macrófagos.

Abstract

Title: Development of shape-tunable Metal-Organic Framework nanosystems for cancer immunotherapy

The tumor microenvironment (TME) plays a crucial role as an essential ecological niche for the onset and progression of cancer, the high prevalence of immunosuppressive cells, with tumor-associated macrophages (TAMs), are major contributing mediators in the pathological process of tumor. TAMs can be divided into two antagonistic polarization states: pro-inflammatory M1 and anti-inflammatory M2 macrophages. Consistent with their functions, TAMs are typically classified as M2-like macrophage phenotypes in the TME. Over the past few years, more attention has been focused on how to restructure and coordinate an inflammatory TME, and TAMs have emerged as a paradigm for understanding the link between inflammation and cancer. An extension of this therapeutic perspective has led to efforts aimed at repolarizing TAMs, shifting them from the M2-like macrophage phenotype to the M1 phenotype. In response to various microenvironmental stimuli, macrophages can adopt different phenotypes and functions. Metal-organic framework nanoparticles (MOF NPs) have been widely used as controlled drug delivery systems and cancer therapy agents due to their intrinsic superior properties, such as a highly structure-tunable capability. Yet, the cellular immune response modulated by tuning the shape of NPs remains unclear. Here, four distinct Cu MOF NPs with different shapes (needle, hexagon, square, and spherical) were synthesized by tuning the synthetic conditions, followed by systematically evaluating the physicochemical properties, biocompatibility, and immune-reprogramming capabilities. Cu MOF NPs with different shapes showed distinct immune responses. Square and needle-shaped NPs promoted macrophage polarization into M1 phenotype, whereas spherically and hexagonally shaped NPs enhanced the expression profile of M2 biomarkers. Overall, this study offers practical insights into the interface interactions between NPs and immune cells, which might have potential implications for NP-based immunotherapy.

Keywords: Cancer Immunotherapy; Metal-Organic Framework; Shape-tunable nanoparticles; Immune response; Macrophage Polarization.

Table of Contents

List of Abbreviations and Acronyms

A

AR.	Aspect Ratio
Arg1.	Arginase-1
ATP.	Adenosine Triphosphate

B

BDC.	Benzenedicarboxylate
BTC.	Benzene tri- or tetra- carboxylate

C

CT.	Computerized Tomography
CuBDC.	Copper-Terephthalic Acid

D

DCs.	Dendritic Cells
DLS.	Dynamic light scattering
DMEM.	Dulbecco's Modified Eagle Medium
DMF.	Dimethylformamide
DNA.	Deoxyribonucleic Acid
DOX.	Doxorubicin

E

EDX.	Energy dispersive X-ray
ELISA.	Enzyme-linked Immunosorbent Assays

F

FBS.	Fetal Bovine Serum
FDA.	Food and Drug Administration

G

GAPDH.	Glyceraldehyde-3-phosphate dehydrogenase
GM-CSF.	Granulocyte-macrophage Colony-Stimulating Factor

H

HEK 293.	Human embryonic kidney 293 cell line

I

IARC.	International Agency for Research on Cancer
IFN-γ.	Interferon-γ
IL.	Interleukin
iNOS.	Inducible Nitric Oxide synthase

IONPs. Iron Oxide Nanoparticles

L

LDH. Lactate dehydrogenase

LPS. Lipopolysaccharide

M

MDP. Muramyl Dipeptide

MIM. 2-Methylimidazole

MOF. Metal Organic Framework

MPS. Mononuclear Phagocytic System

MRI. Magnetic Resonance Imaging

N

NP. Nanoparticle

NTA. Nanoparticle Tracking Analysis

P

PBS. Phosphate Buffered Saline

PCR. Polymerase Chain Reaction

PDGF. Platelet-derived Growth Factor

PMA. Phorbol-12-myristate-13-acetate

PS. Penicillin-Streptomycin

R

RNA. Ribonucleic Acid

ROS. Reactive Oxygen Species

S

SEM. Scanning Electron Microscopy

T

TAM. Tumor-Associated Macrophage

TEM. Transmission Electron Microscopy

TGF-β. Transforming Growth Factor Beta

TME. Tumor Microenvironment

TNF-α. Tumor Necrosis Factor Alpha

V.

VEGF. Vascular Endothelial Growth Factor

List of Figures

List of Tables

1. Introduction

1.1 Context and Motivation

In recent years, immunotherapy has gradually become a new standard therapy for cancer, since it can stimulate the immune system to recognize and attack tumor cells. However, the therapeutic effect of most immunotherapy strategies can be weakened as a result of the immunosuppressive tumor microenvironment (TME), which is caused by the presence of immunosuppressive cells and tumor-associated macrophages (TAMs) account for the highest proportion. TAMs usually display the tumor promoting M2 phenotype rather than the tumoricidal M1 phenotype. However, in response to various stimuli in TME, the TAM population shows a state of constant transition between these two major forms, M1 and M2-like phenotypes, that exhibit different functions. Therefore, in the last few years, more attention has been given on how to promote the polarization of TAMs to the M1 type.

Current clinical trials use bacterial cell wall components, lipopolysaccharide (LPS) or muramyl dipeptide (MDP), and cytokines like interferon-γ (IFN-γ) and granulocyte-macrophage colony-stimulating factor (GM-CSF) to activate macrophages towards M1 phenotype as a novel immunotherapeutic approach. However, the short duration of action of IFN-γ and MDP, primarily due to their rapid clearance, along with the challenge of systemic administration of LPS without inducing toxicity *in vivo*, have collectively hindered their progression as viable clinical alternatives. To overcome this hurdle, a nanoparticle (NP)-based strategy can provide a viable alternative to immunomodulatory therapies. For instance, metal-organic framework (MOF) nanoparticles provide a possible solution to overcome the above challenge. MOF nanoparticles consist of crystalline hybrid materials built up from the coordination between metal (transition metal or lanthanide metal) ions and organic ligands (carboxylates, azolates, and phosphonates). Furthermore, MOF nanoparticles have emerged as promising candidates for biomedical applications due to their low toxicity, structural flexibility, and safe biodegradation in a physiological environment. However, the biological effects of nanoparticles are largely dictated by their unique physicochemical properties, for example, chemical composition, shape, size, and surface properties. In fact, previous studies have shown an effect of NP shape on modulating macrophage phagocytosis, revealing it to be an important parameter for regulating the immune response. Thus, investigating how the shape of NPs affects macrophage

polarization, can aid the optimal NPs design to elicit a robust immune response and, consequently, provide new solutions for treating cancer and other types of diseases.

1.2 Aim of the Work

The main objective of the present study was to investigate the impact of shape-tunable MOF NPs on modulating macrophage phenotype. For this purpose, Cu-based MOF NPs with different shapes have been fabricated, characterized, and further incubated with macrophages to evaluate their capability on polarizing macrophage phenotypes.

The specific aims of this thesis were:

i. To study the effect of the synthesis conditions of Cu MOF NPs on their physical-chemical properties.
ii. To evaluate the biocompatibility of Cu MOF NPs by using different cell lines.
iii. To evaluate the polarization effect of Cu MOF NPs on immune cells.

1.3 Project Outline

This thesis includes four chapters, namely the State of the Art, Materials and Methods, Results and Discussion, and finally Main Conclusions. The State of Art (chapter 2) describes the current advances of NPs for biomedical applications and cancer immunotherapy. The Materials and Methods (chapter 3) is composed of a brief summary of methods, equipment, and analytical software used during the project development. Chapter 4 presents the results and respective discussion in this study. Finally, chapter 5, highlights the major conclusions and emphasizes limitations and future perspectives.

2. State of the Art

2.1 Nanotechnology in Medicine

Nanotechnology has introduced innovative and promising approaches for manipulating various diseases in contrast to conventional therapies. Traditionally, nanotechnology includes materials, devices, and systems with the size of 1 to 100 nm, but many nanomedicines are within the submicron size of 100-1000 nm (Pillai et al., 2013). These nanoparticles are regarded as nano-sized tools for the diagnosis, prevention, monitoring, and treatment of various diseases (Astruc, 2016). For instance, nanotechnology solutions have been shown to be beneficial for the treatment of neurodegenerative (Silva Adaya et al., 2017), cardiovascular (Karimi et al., 2016; Kratz et al., 2016), and autoimmune diseases (Gharagozloo et al., 2015), osteoporosis (Ahmad et al., 2022; Barry et al., 2016; Mora-Raimundo et al., 2017) and against bacterial infections (Hajipour et al., 2021; Yeh et al., 2020). Indeed, the more prominent applications of nanotechnology in medicine are in imaging techniques, tissue-engineered constructs, implants, and drug delivery systems, particularly in the field of cancer therapy (Zhang et al., 2023). To date, a set of nanomaterials has been developed and approved for clinical use (Sim et al., 2021).

2.1.1 Nanoparticles for Biomedical Applications

Nanoparticles (NPs) have been tremendously adopted in important biomedical applications such as imaging, drug delivery, and immunotherapy (Guo et al., 2021). For example, gold NPs decorated with a prostate-specific membrane antigen RNA aptamer have been shown a higher computed tomography (CT) density for prostate cancer cell imaging (Kim et al., 2010). Moreover, super-paramagnetic iron oxide nanoparticle (SPIONs) surfaces decorated with a high-affinity anti-EGFR antibody have been shown to target lung tumors by MRI imaging (Wang et al., 2017).

Besides imaging, one of the most promising applications of NPs is the possibility to specifically target their content, delivering small drugs as well as macromolecules like proteins, peptides, or genes, and exhibiting improved drug bioavailability, uptake of low solubility drugs and decreased toxicity (Sim et al., 2021). For example, metallic NPs can be conjugated with a fluorescent marker for drug delivery and imaging in magnetic resonance (Khodabandehloo et al., 2016; Mirza et al., 2014). Cationic liposomal systems are also

employed in drug delivery because of their capacity to transport charged structures, such as DNA and RNA, via the electrostatic interactions between the positively charged phospholipids and the negatively charged nucleic acids (Sercombe et al., 2015). Other hydrophilic polymers, such as dextran-based polysaccharide, consists of hydrophilic and neutral chains at the NPs surface, repelling plasma proteins (Al-Musawi et al., 2020).

For cancer immunotherapy, NPs play a vital role in activating the host's immune system. Accordingly, different types of NPs have been and are being widely used in cancer immunotherapy, such as polymeric NPs (Li et al., 2018), liposomes (Yoshizaki et al., 2017), mesoporous silica NPs (Thakur et al., 2020), micelles (Zeng et al., 2017), and nanosized metal-organic frameworks (Ni et al., 2020) (**Figure 1**).

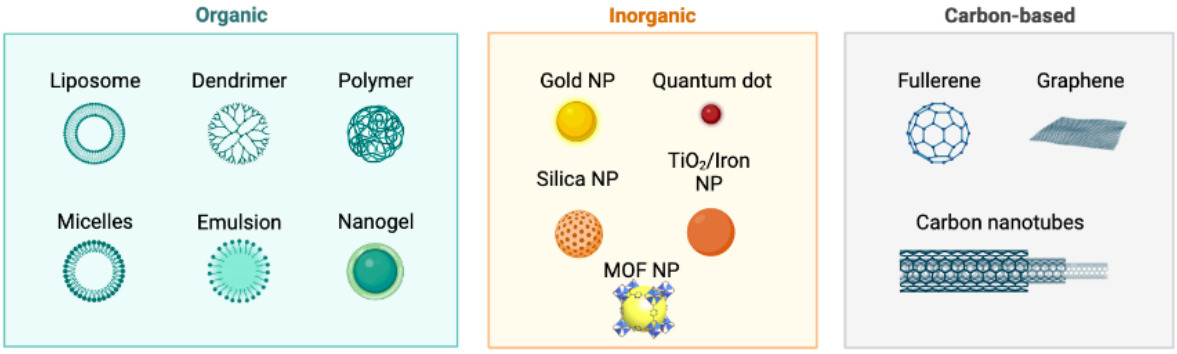

Figure 1. Overview of commonly used nanoparticle types, classified as organic, inorganic or carbon-based structures. Created with BioRender.com.

2.1.1.1 Metal-Organic Framework Nanoparticles

Metal-organic framework nanoparticles (MOF NPs) are one type of NPs that have gained considerable relevance in preclinical and clinical settings, including gas storage and separations (Venna et al., 2015), chemical sensing (Kreno et al., 2012), catalysis (Dhakshinamoorthy et al., 2018), drug delivery (Zhuang et al., 2014), among others. MOF NPs consist of crystalline hybrid materials built up from the coordination between metal (transition metal or lanthanide metal) ions and organic ligands (carboxylates, azolates, and phosphonates) (Wang et al., 2018) (**Figure 2**). MOF NPs have unique properties that cannot be found in organic or inorganic systems due to their hybrid nature, namely their consistency in physicochemical properties unrivaled by conventional structures (Burtch et al., 2018; Li et al., 2022). Indeed, MOF NPs exhibit controlled surface chemistry, unparalleled

surface areas, pore volumes, and reversible structural flexibility (Sun et al., 2020), allowing the efficient prediction of their physiological metabolism and functions *in vivo* (Li et al., 2022). Then, these unique properties of MOF NPs, including their porous structure, large surface area, flexibility of the coordination between organic ligands and nodes, and inherent photo-responsive features provide significant advantages for a wide range of biological applications, including cancer phototherapy and immunotherapy (Fernandes et al., 2023). Moreover, these properties enable the development of suitable MOF-based systems that can be modified for a variety of therapeutic purposes while ensuring good compatibility (Liu et al., 2022; Yang et al., 2020). MOF NPs can also be synthesized with functional nodes and linkers (such as peptides and fluorescence) that possess inherent antitumor and photosensitizer properties (Gao et al., 2021), acting directly as immunotherapy agents. Even without extra loading of functional drugs, the ligands or metal ions in MOF NPs can also be employed for immune activation or biological imaging (Lan et al., 2018). MOF NPs have been designed and functionalized as on-demand therapeutics that are activated by either external energy stimuli or endogenous triggers to generate reactive oxygen species (ROS), inducing immunogenic cell death of tumor cells (Ni et al., 2020). Thus, the flexible topological structure, large specific surface area, high porosity, and multiple encapsulation strategies of MOF NPs endow them with the ability to deliver antitumor drugs ensuring high drug loading capacities and controllable release rates (Luo et al., 2021;Wu et al., 2017). Drugs with different properties, such as hydrophobic and hydrophilic drugs, can be effectively loaded into MOF NPs (Cheng et al., 2022). For example, in a relatively recent study, a hollow MOF drug delivery system loaded with 5-fluorouracil (5-FU) was used in order to verify its targeted antitumor drug transport abilities, demonstrating high drug loads and sustaining its drug release behavior (Gao et al., 2016).

However, challenges in employing MOF NPs for some biomedical applications remain. The main synthetic challenge in the synthesis of MOF NPs is their low stability towards water. Reducing the contact between water molecules and MOF host frameworks, particularly the coordination bonds, was considered to be an effective strategy to improve MOF stability (Lv et al., 2019). For instance, to address this issue, polytopic rigid linkers that favor strong coordination bonds are used for their construction. Aromatic phenylene or acetylene-based linkers are traditionally employed in combination with strongly coordinating carboxylate linkers and high oxidation state metal ions (Ahmed et al., 2022). Moreover, by

introducing hydrophobic pore surfaces or blocked metal ions, water molecules are prevented from approaching the framework. Therefore, to sustain the framework robustness in the presence of an aqueous medium, some MOF NPs have been specifically functionalized by introducing nonpolar alkyl functional, fluorinated, or methyl groups (Ahmed et al., 2022). Another existing challenge, if the unreacted precursors cannot be rapidly depleted, is that the generated nucleus will continuously grow, generating microparticles rather than NPs. These microparticles normally exhibit limited accumulation in the tumor tissues compared to the NPs administered by intravenous injection. In addition, although MOF NPs are fabricated by coordinating metal ions and organic ligands, massive ions and proteins in the circulation system will also interact with the metal ions or organic ligands of the MOF, causing degradation or aggregation. Therefore, developing a strategy to increase MOF NP accumulation in tumor tissues is necessary to achieve enhanced therapeutic effects (Cheng et al., 2022).

To prepare large-scale uniform MOF crystals for practical applications, numerous synthetic schemes have been developed, including water/solvothermal synthesis (Zou et al., 2019), microwave-assisted and ultrasonic-assisted methods (Bakhshi et al., 2021), microemulsion-based synthesis (Sun et al., 2016), and direct mixing method (Wang et al., 2013). For example, the preparation of MOF crystals through water/solvothermal synthesis is straightforward and simple to perform. It involves the dissolution of the metal ions and organic ligands in solvents, followed by their incubation in a reactor. The MOF crystals are obtained after a set amount of time, using high temperature and pressure (Luo et al., 2021). Otherwise, the microwave synthesis method involves mixing the chemicals needed for the reaction and the solvent together and then putting the mixture in a microwave reactor. This method is useful because the reaction is relatively fast, taking only a few tens of minutes, compared to the longer reaction time of solvothermal synthesis. Also, the microwave method allows the formation of nanoscale MOF particles because it provides uniform heating (Luo et al., 2021).

It is known that some unit operations can modify the size, structure, and morphology of MOF particles during processing (Marshall et al., 2019; Wang et al., 2013; Xin et al., 2015) (**Figure 2**).

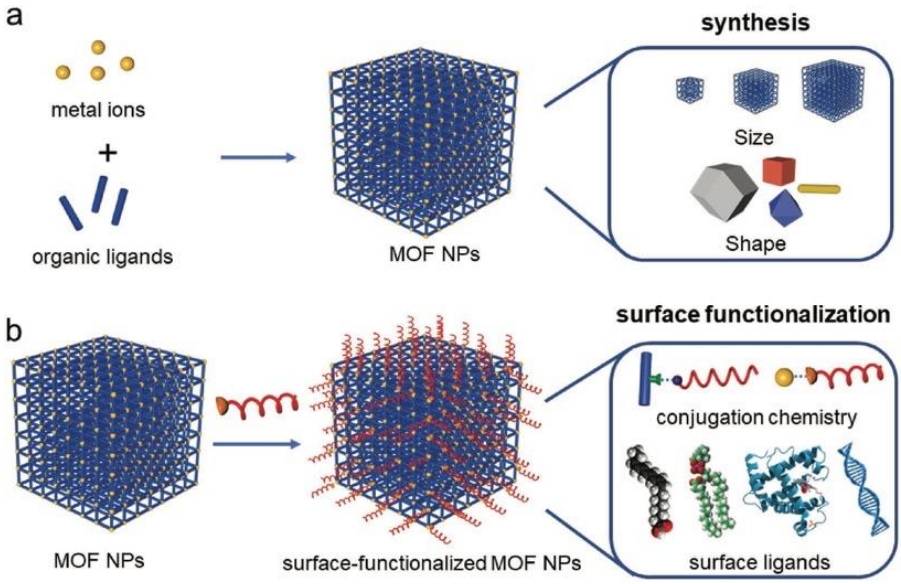

Figure 2. Schematic representation of (a) the modular synthesis of MOF NPs, with control over size and morphology, and (b) the post-synthetic external surface functionalization with multiple conjugation strategies and types of surface ligands. Taken from Wang et al., 2018. Copyright 2018, Wiley-VCH.

In fact, the potential efficiency of MOF NPs can be exceptionally improved by finely adjusting their size and morphology (Liu et al., 2018). Some of the synthesis methods mentioned before having been reported to control MOF morphologies based on varying solvents, introducing surfactant or template agents (Liao et al., 2019). In addition, the incorporation of monotopic ligands that mimic the functionality of the multitopic MOF linkers into solvothermal syntheses, specifically named coordinating modulating, has gradually become a widely used method for adjusting the chemical and physical properties of the MOF NPs by manipulating their morphology, defect rate, exposed crystal facets, surface chemistry, and other factors (**Figure 3**) (Forgan, 2020). This method involves introducing a modulator, usually a monotopic analog of the linker, to control the growth of MOF crystals. The modulator often contains a carboxylic acid as the linker because it can serve two functions: acting as a surface capping ligand to stop the growth of MOF crystals and modify the MOF surface and acting as an acid to adjust the rate of metal-linker complexation for crystal growth by interfering with linker deprotonation (Li et al., 2023). For example, CuBDC-NBA with different morphology and size were achieved at room temperature through coordination modulation. Indeed, with increased 4-n-Butylbenzoic Acid (NBA, modulator) addition, the morphological transformation from nanosheet to

nanoflower then to sheet, and the size transformation from smaller nanosheet to larger sheet were observed (Li et al., 2023).

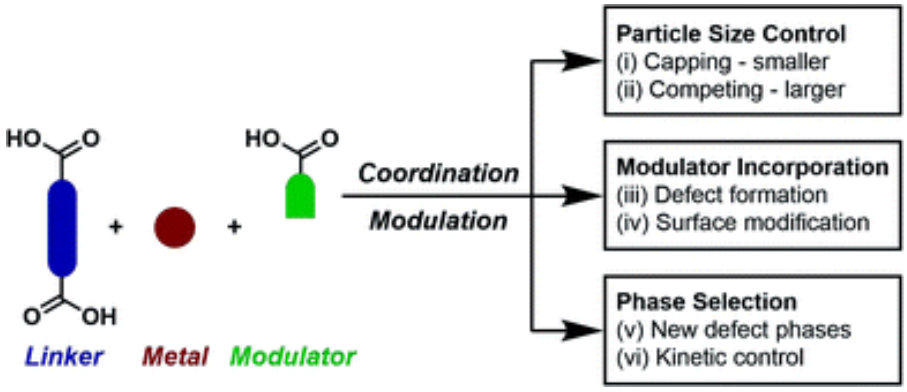

Figure 3. Schematic of coordination modulation, with a range of different potential outcomes. Taken from Forgan, 2020. Copyright 2020, Royal Society of Chemistry.

2.2 Physicochemical Properties Play a Critical Role in Nanoparticle-Induced Macrophage Polarization and Reprogramming

The biological effects of NPs are largely dictated by their unique physicochemical properties, for example, chemical composition, shape, size, and surface properties. Among these parameters, particle morphology seems to contribute significantly to the inflammation-modulating property of nanoparticles (Liu et al., 2018).

2.2.1 How does the shape of nanoparticles influence cell behavior?

Several studies revealed that particle shape contributes significantly to its inflammation-modulating property. For example, hydroxyapatite NPs with fiber and dot morphology caused higher acute inflammation *in vivo* as compared to the NPs with sheet morphology. This study demonstrated that fibers were incompletely phagocytosed and internalized by monocytes and macrophages, and subsequently, superoxide anions and other peroxide radicals were released to the outside of the cell, eventually leading to chronic inflammation (Pujari-Palmer et al., 2016). Similarly, three different shapes of poly(3,4-ethylenedioxythiophene) (PEDT) nanomaterials were shown to have different effects on ROS production and pro-inflammatory response, with pro-inflammatory cytokines being induced from macrophages by PEDT nanomaterial-treated cells, depending on the shape and concentration of the nanomaterial. Besides, the cytotoxicity and apoptosis of the

nanomaterials increased with their decreasing aspect ratio (Oh et al., 2010). Another study demonstrated that $Ce0_2$ nanorods/nanowires exhibiting shorter lengths and lower aspect ratios may induce inflammasome activation (Ji et al., 2012). The importance of NPs shape in the activation of macrophages was also analyzed by the synthesis of four different morphologies of iron oxide nanoparticles (IONPs) with similar composition and surface charge (Liu et al., 2018). This study concluded that morphology is a critical factor for IONP-induced IL-1β release by macrophages, with octopod morphology exhibiting significantly greater activity than cube and sphere IONPs. In this case, the differential ability of the four IONPs to modulate inflammasomes was not due to the difference in cellular internalization. Instead, the intracellular mechanisms, including ROS generation, lysosomal damage, and potassium efflux, three well-known mechanisms for nanoparticle-facilitated inflammasome activation, were found to be responsible for the observed difference of the four IONPs in inducing inflammasome activation (Liu et al., 2018). Thus, taken together, these data suggest that the formulation and shape of NPs are characteristics that must be considered for the development of NPs with applications for reprogramming macrophages and cancer treatment.

2.2.2 How does the size of nanoparticles influence cell behavior?

In addition to varying in shape, these NPs also differ in size, resulting in distinct effects on inflammation modulation (Miao et al., 2017). For instance, Ma *et al*. showed that graphene oxide (GO) NPs induce macrophages to polarize to the M1 subtype in a size-dependent manner (Ma et al., 2015). The largest GO nanosheets, with a size range between 750 nm and 1300 nm, secreted the highest levels of pro-inflammatory cytokines whereas the lowest levels of pro-inflammatory cytokines were observed in the smallest GO nanosheets, with a size range between 50 nm and 350 nm (Ma et al., 2015). Further studies demonstrated that, although the smallest GO had a greater cellular uptake than the largest ones, it could not activate the TLR4 signaling and NF-κB pathways to induce macrophage polarization (Miao et al., 2017).

Besides, other studies revealed that NPs with smaller sizes could have a more potent effect on inducing inflammatory responses than their larger counterparts. In particular, one of these studies demonstrated that the smallest Au NPs were more potent in the induction of macrophages into the M1 subtype, expressing a higher level of pro-inflammatory

cytokines such as IL-1, IL-6, and TNF-α, which can be due to the fact that the cytotoxicity of Au NPs decreases as its size increases (Nishanth et al., 2011). Likewise, for most metallic NPs, the degree of induced macrophage polarization toward the M1 subtype was associated with the size of the NPs. For example, as the Ag, Al, and Au NP sizes decrease, there is a greater effect on M1 macrophage polarization, as suggested by the release of TNF-α and IL-6 in macrophages (Nishanth et al., 2011).

In summary, NPs' size plays a decisive factor in inducing macrophage polarization, independently of whether the smaller or larger NPs are more likely to drive macrophage polarization.

2.2.3 How does the surface charge of nanoparticles influence cell behavior?

It has also been demonstrated that the surface charge of NPs significantly modifies their ability to modulate the inflammatory response of TAMs (Ding et al., 2023). In general, NPs with a charged surface induce the polarization of M1 or M2 more easily than neutral ones. Additionally, NPs with a positive surface charge have often been associated with an increased cellular uptake compared to negatively charged NPs (González-García et al., 2022). For instance, an interesting *in vitro* study evaluated whether SPIONs with different charges have distinct effects on macrophage polarization (Zhang et al., 2020). The results revealed that IONPs with positive and negative charges exhibit higher cellular uptake and polarization effects on macrophages (from M2-like TAM to M1) when compared to IONPs with neutral charges that exhibit lower uptake and cell toxicity, as well as inefficiency-inducing macrophage polarization. However, it has also been shown that IONPs with a negative charge present higher cellular toxicity than IONPs with a positive charge (Zhang et al., 2020). It was hypothesized that the neutral surface limited the nanoparticles' internalization by cells, and thus restrained the M1 polarization of SPIONs. Consistently, a previous study has reported that PMA-coated IONPs significantly induced M1 polarization in RAW 264.7 macrophages, while further modifying IONPs with PEG (polyethylene glycol) outside the original layer dramatically reduced the effect of M1 polarization (Cheng et al., 2019). This decrease is likely due to the limited uptake and endocytosis of PEGylation of nanoparticles by macrophages, resulting in a lower amount of particle accumulation and decreased activation of cellular signals and immune response (Andrade et al., 2021). Meanwhile, the difference in cellular uptake of distinct surface-modified nanoparticles is supported by

another study where both anionic and cationic silica NPs coated with numerous poly(amino acid)s (PAAs) were used to study the charge effect, evaluating the activation of DCs and their IL-1β induction (Kakizawa et al., 2017). Interestingly, anionic NPs and cationic NPs did not show a significant difference in IL-1β production. However, between cationic NPs, poly(arginine)-coated NPs (Arg NPs) induced higher IL-1β production than poly(lysine) NPs (Lys NPs) probably because the hydrophobicity of Arg is higher than Lys revealing a hydrophobicity-dependent IL-1β production effect (Kakizawa et al., 2017).

2.3 Biomedical Applications: Cancer

Cancer is characterized by the uncontrolled growth and spread of abnormal cells, that invade other organs and ultimately lead to the patient's death (Zaorsky et al., 2017). It remains one of the leading diseases that threaten the health of humans, and its burden continues to grow globally, exerting tremendous physical, emotional, and financial pressure on individuals, families, communities, and health systems (Peng et al., 2022). The International Agency for Research on Cancer (IARC) recently estimated that about 10 million deaths worldwide were due to cancer, with 19.3 million new cases per year being reported worldwide (Ferlay et al., 2021). In addition to these numbers, the burden of cancer is expected to increase to 23.6 million new cancer cases per year by 2030 (*Level of Human Development (HDI) Mort Prev*, 2014).

2.3.1 Conventional Cancer Therapy

Currently, traditional tumor treatment methods include surgery, radiotherapy, and chemotherapy. Although these treatments contribute to the recovery of many patients, they still exhibit unsatisfactory clinical benefits and severe side effects during anti-neoplastic treatment, such as risks of injury or toxicity to normal tissues (Peng et al., 2022). In fact, the most common cancer treatment strategies include surgical removal of tumors, followed by radiotherapy using X-rays and/or chemotherapy (Debela et al., 2021). Surgery is most effective when the cancer is in the early stages of development. Radiotherapy can harm healthy cells, organs, and tissues. While chemotherapy can be effective in reducing morbidity and mortality, it can also damage healthy cells, especially those that are rapidly dividing and growing. Moreover, a common problem with chemotherapy is drug resistance, in which cancer cells that were initially suppressed by an anti-cancer drug develop resistance

to it. This can be caused by reduced drug uptake and increased drug efflux (Bukowski et al., 2020). Other limitations of chemotherapy include difficulty in selecting the proper dosage, lack of specificity, rapid drug metabolism, and harmful side effects (Debela et al., 2021). In summary, the success rate of cancer treatments has resulted in an increase in the number of long-term survivors with a wide range of chronic health problems (Debela et al., 2021).

Although substantial efforts have been developed to overcome cancer, current therapeutics are not always effective in preventing the progression of the disease and the high mortality rate among cancer patients. Therefore, there is an urgent need to explore and develop research focused on new therapeutic approaches with high efficiency and few side effects (Nascimento et al., 2021). Nanotechnology, for example, can be used as a strategy to target drug delivery and minimize its side effects, by using ligands that target the overexpressed transporters and receptors on the cancer cell membrane (Qu et al., 2022; Wu et al., 2022).

2.3.2 Cancer Immunotherapy

The immune system plays an important role in preventing tumor development. In fact, in 1893, William Coley, an American orthopedic surgeon, accidentally discovered that suppurative streptococcal infection after surgery caused tumor regression in patients with sarcoma (Zhang et al., 2020). This breakthrough marked the beginning of tumor immunotherapy, which, after a century of development, has introduced novel treatment options for numerous challenges to treat many cancer types (Peng et al., 2022). Besides, in 2011, the US Food and Drug Administration (FDA) approved the first immune checkpoint inhibitor (anti-CTLA-4 monoclonal antibody, Ipilimumab) for the treatment of advanced melanoma, which marked a new era of cancer immunotherapy (Vaddepally et al., 2020). Generally, cancer immunotherapy is a new strategy that employs intrinsic immune system activity to combat cancer, boosting the host's immune system to detect specific cancer cells for efficient elimination (Cai et al., 2020). Furthermore, the antitumor immune response initiated by immunotherapy could promote systemic immune monitoring, allowing the elimination of local and distant metastasis (Duan et al., 2019; Zhang et al., 2020). Also, immunotherapy could build up long-term immune memory, regulate immune protection, and prevent tumor reappearance (Chen et al., 2019).

Despite significant developments accompanied by therapeutic efficacy, there are still

clinical failures and some obstacles in cancer immunotherapy, such as the pharmaceutical kinetics, which is limited, and the overall response rate from immunotherapy remains relatively low, normally between 10% to 30% depending on the type of cancer (Fisher et al., 2020; Lee Ventola, 2017). This is mainly because the tumor develops multiple resistance pathways, the molecular, cellular, and TME levels (Fisher et al., 2020). Regulating antitumor immunity demands accurate activation of a complex immunological system, which does not happen in common cancer treatments (Das et al., 2017). For example, many immunotherapy approaches aim to generate or release a large number of highly effective cytotoxic T lymphocytes (CTLs) that can quickly infiltrate tumor tissues and destroy cancer cells. However, the effectiveness of this type of therapy can be reduced due to the immunosuppressive environment of the tumor, often characterized by the presence of immunosuppressive cells, with tumor-associated macrophages (TAMs) being the most prevalent type (Mahoney et al., 2015).

2.3.2.1 Immunological Tumor Microenvironment

Tumors have evolved distinctive microenvironments throughout their development, differing from normal tissues. The TME plays a crucial role in the initiation and expansion of tumors by offering a nurturing setting for cancer cell proliferation (Sadeghi Rad et al., 2021). The TME is characterized by an acidic pH, high levels of ROS and glutathione, hypoxia, increased enzyme activity, and high levels of adenosine triphosphate (ATP). The TME promotes tumor angiogenesis and metastasis and can also contribute to treatment resistance and failure. TME has become an important target for cancer treatment and is often used as a stimulus for drug release in immunotherapy (Peng et al., 2022).

2.3.2.1.1 Immunosuppressive Tumor-Associated Macrophages

Different immune cells have been studied as potential targets in cancer immunotherapy. Recently, a great interest on TAMs as potential therapeutics has been registered because these cells represent one of the most abundant leukocytes in the TME. Clinically, they have been linked to worse patient outcomes in various types of cancer, including breast, lung, and lymphoma.

2.3.2.1.1.1 Characterization of the Polarized Macrophage Phenotype

Macrophages, fundamental cells of the mononuclear phagocytic system (MPS), are highly plastic and heterogeneous immune cells that serve a multitude of functions, including the elimination of pathogens, clearance of cellular debris, tissue development, and hemostasis, and regulation of inflammatory responses (Anderson et al., 2021; Miao et al., 2017). Postnatal development of macrophages is driven by the differentiation of circulating monocytes through the macrophage colony-stimulating factor (M-CSF) or granulocyte macrophage-stimulating colony factor (GM-CSF). These monocytes have their origins in the bone marrow from myeloid-derived progenitor cells and the resulting macrophages can display a broad spectrum of phenotypic states. Without any stimulation or in the resting cells, the phenotype of the macrophage is referred to as an M0 macrophage. M0 macrophages can be induced by environmental signals toward M1 and M2 polarization, which are the two main activated states of macrophages (Miao et al., 2017). While the M1/M2 model is commonly used to classify macrophages, it is important to note that this model is oversimplified and does not fully capture the complexity of macrophage function. Macrophages are highly plastic and can exhibit overlapping functions and markers between subsets, and it may be more accurate to consider their activation as a continuum of functional states rather than discrete M1 and M2 subsets (Martinez et al., 2014; Murray et al., 2014).

M1 macrophages perform a pro-inflammatory function and are polarized by lipopolysaccharide and some cytokines such as interferon-gamma (IFN-γ) or GM-CSF to display strong effector functions against pathogens and cancer cells (*e.g.*, trap, phagocytose, and lyse tumor cells) (Yunna et al., 2020). Moreover, M1 macrophages not only have high phagocytic ability but also overexpress CD80, CD86, and CD16/32 and produce increased levels of pro-inflammatory cytokines, including interleukin 12 (IL-12), interleukin 23 (IL-23), and tumor necrosis factor-alpha (TNF-α), which facilitate leukocyte recruitment and activation during injury (**Figure 4**). In addition, the enhanced tumor antigen-presenting ability of M1 promotes other leukocytes' cytotoxic functions (Liu et al., 2021). For example, $CD8^+$ T cells and NK cells can be strengthened by immuno-stimulatory cytokines from M1 phenotype macrophages (Dungan et al., 2014).

Conversely, polarization by interleukin 4 (IL-4) and interleukin 13 (IL-13) can result in

alternatively activated M2 macrophages that perform anti-inflammatory functions (Sylvestre et al., 2020). The expression of arginase-1 (Arg1), mannose receptor (CD206), anti-inflammatory factor (IL-10), and chemokines CCL17 and CCL22 are elevated in M2 macrophages, acting as an immune-suppressor in tumor nest (**Figure 4**). In fact, while M2 macrophages have a critical role in maintaining normal immune function and homeostasis, like promoting Th2 responses, combating parasites, contributing to wound healing and tissue regeneration through the clearance of debris and the release of growth factors such as transforming growth factor beta (TGF-β), platelet-derived growth factor (PDGF), and vascular endothelial growth factor (VEGF) (Sylvestre et al., 2020), specific subsets of M2 macrophages also play a pivotal role in supporting tumor progression (Anderson et al., 2021). On one hand, due to weakened tumor antigen-presenting ability, the pro-inflammatory potential of M2 phenotype macrophages is dramatically descended. On the other hand, M2 phenotype macrophages are educated to be tumor promoting by releasing growth factors forming a positive feedback loop in accordance with cytokines and factors of tumor cells (IL-4, IL-6, IL-10, among others) (Liu et al., 2021).

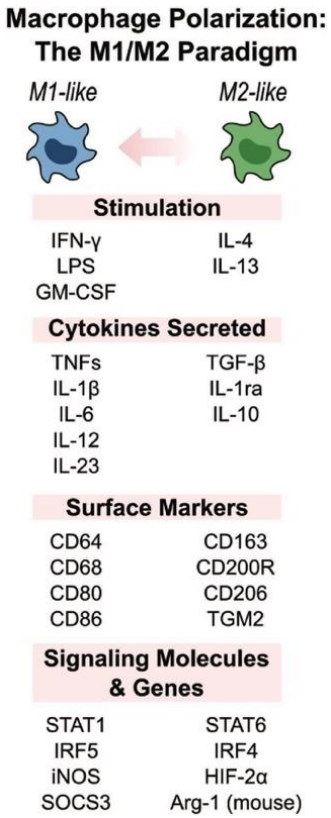

Figure 4. Macrophages that have been activated can generally be grouped into two categories: M1-like and M2-like macrophages. These types of macrophages are activated by different stimuli, have different characteristics, and perform different functions. Taken from Sylvestre et al., 2020.

Copyright 2020, Wiley-VCH.

Tumors recruit both circulating monocytes and resident tissue macrophages to the TME and polarize them toward an M2 phenotype via a variety of soluble and mechanical factors, creating TAMs. These cells can influence both tumor progression and antitumor response through a variety of mechanisms (Crezee et al., 2020) (**Figure 5**). On one hand, TAMs can promote the growth and spread of cancer by promoting genetic instability, supporting the formation of new blood vessels, and releasing growth factors and enzymes that break down the extracellular matrix and basement membrane. In addition, they can stimulate cancer cell migration through paracrine signaling C-C motif ligand 18 (CCL18), as well as prepare distant metastatic sites for seeding (Williams et al., 2016). On the other hand, they can also suppress the immune system, making it harder for the body to fight cancer, through upregulation of immunosuppressive surface proteins, secretion of ROS, production of cytokines to suppress T-cell function, secretion of chemokines that recruit regulatory T cells (Anderson et al., 2021), and inhibition of B cell signaling (Guo et al., 2016; Timosenko et al., 2017). Thus, nowadays, different research approaches have sought to develop strategies to reprogram TAMs to perform an antitumor action (Anfray et al., 2020).

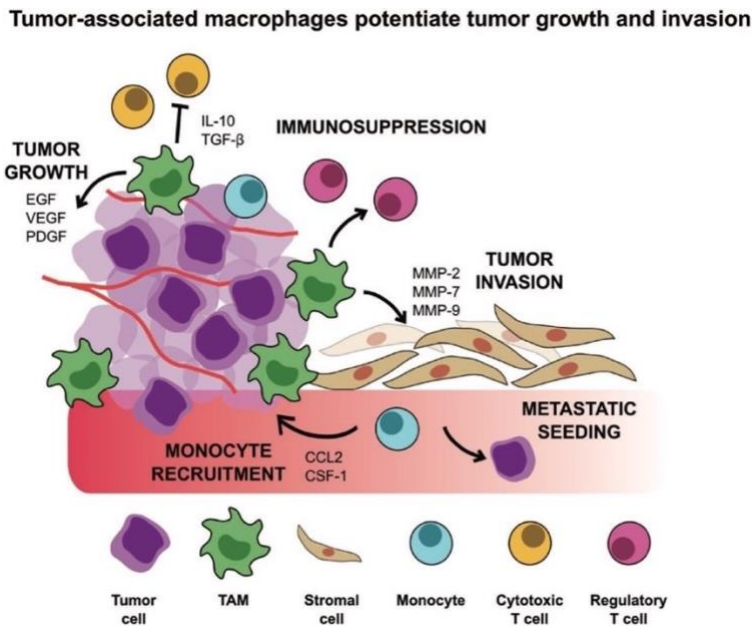

Figure 5. TAMs contribute to the growth and spread of tumors in several ways, such as by suppressing the immune system, recruiting monocytes, and creating environments suitable for distant metastasis. They also help tumors invade surrounding tissues by releasing enzymes that dissolve the basement membrane and secreting angiogenic growth factors. Taken from Sylvestre et al., 2020. Copyright 2020, Wiley-VCH.

2.3.2.1.1.2 Mechanisms of Macrophage Polarization

Since macrophages play an important role in regulating the body's immune response and metabolism, the direction of macrophage polarization can be modulated to change to the desired phenotype. Macrophage polarization is defined as the dynamic process in which resting macrophages experience various functional changes to adjust to the changing of the residing milieu. For example, regulating the acidity of the TME is an effective strategy for changing the polarization phenotype of macrophages, since their phagocytic function is closely related to the pH of lysosomes (Lavine et al., 2018; Murray et al., 2014). While M2 macrophages repair damaged tissues by phagocytosis, the basic property of M1 macrophages is to promote tissue damage (Yunna et al., 2020). Therefore, altering the pH of lysosomes may be an effective approach for resetting the polarization phenotype of macrophages. Alkaline agents such as chloroquine (CQ) are known to be trapped in the lysosomal compartment, increasing lysosomal pH and allowing TAMs to be reset from M2 to the M1 phenotype (Chen et al., 2018). Additionally, due to the rapid growth of malignant tumors, there is an area of hypoxia inside the tumor (Wang et al., 2019), that is involved in the induction of epithelial-metabolism and TAMs infiltration. Hypoxia may have a deep effect on the polarization of macrophages due to the preferential accumulation of macrophages in hypoxic tumor areas and the retention of relatively immature cell types (Chen et al., 2013). The hypoxic TME stimulates macrophages to secrete exosomes rich in immunoregulatory proteins and chemokines, which promote macrophage polarization to the M2 phenotype, thereby stimulating angiogenesis, metastasize, and inhibiting host immunity (Jeong et al., 2017; Park et al., 2019). Therefore, improving the hypoxic TME is an efficient method to regulate the polarization phenotype of macrophages. Furthermore, the development of some diseases like cancer is accompanied by changes in the composition of the ECM (extracellular matrix), a highly dynamic and complex macromolecular network, and contributes to the development of the disease (Mouw et al., 2014). Among them, the ECM component in the TEM has a regulatory effect on macrophage polarization. For example, proteases and their inhibitors are key physiological regulators of ECM remodeling. The extracellular serine protease inhibitor (serpin) serpinE2 is overexpressed in various human cancers and participates in tumor progression and metastasis. By inhibiting the expression of serpinE2, M2-like macrophages can be promoted to M1-like phenotype polarization and

inhibit vascular invasion and tumor spread (Smirnova et al., 2016). Finally, it is well-known that nanocarriers cause macrophage polarization phenotype changes *in vivo* mainly through macrophage internalization, leading to changes in cellular uptake and secretion of cytokines and chemokines (Yunna et al., 2020). Remarkably, material parameters such as porosity (Sussman et al., 2014), stiffness (Blakney et al., 2012), and nanotopography (Lee et al., 2011) change the inflammatory response. Therefore, understanding how nanocarriers affect macrophage polarization and inflammatory response is an effective strategy to promote the clinical application of nanocarriers. Various engineered drug-free nanocarriers were used to reset the macrophage polarization phenotype as it can be used to induce TAM polarization from the M2 phenotype to the M1 phenotype (Pal et al., 2016; Zanganeh et al., 2016).

2.4 *In vitro* models

Several different biological cell models are being used to explore NPs' safety and efficacy. Recently, different cell lines have been used as models because they maintain representative functional features, that enable the clear analysis of a well-known cell response. Cell lines such as human cervical adenocarcinoma (HeLa) (Schirinzi et al., 2017) and human epithelial colorectal adenocarcinoma (Caco-2) (Wu et al., 2019) have been used as a model of anatomical barriers. Likewise, human embryonic kidney cells (HEK 293) have been widely used in biomedical research as a model system due to their high transfection efficiency and reliable growth. On the other hand, human peripheral blood monocyte cells (PBMCs), human monocytic (UP37 and THP-1), mouse macrophage (DMBM-2) (Prietl et al., 2014), and murine macrophages (RAW 264.7) have been used as immune cell models for *in vitro* evaluation of NPs effect (Aguilar-Guzmán et al., 2022).

RAW 264.7 cells are adherent macrophage-like cells derived from tumors, inoculated with Abelson murine leukemia virus. These cells are immortalized, relatively stable, and mature and have been used for models of macrophage activation in numerous studies (Bastos, 2016). According to previous studies, the murine leukemic monocyte-macrophage cell line RAW 264.7 is a representative and versatile macrophage cell line worldwide accepted as a macrophage model. It has been an amenable *in vitro* model as it exhibits key characteristics representative of different macrophage types *in vivo* (Bordbar et al., 2012).

3. Materials & Methods

3.1 Synthesis of Cu MOF Nanoparticles with Different Shapes

An overview of the different methods used in the synthesis of Cu MOF NPs with different shapes is reported in **Figure 6**. In this work, to produce MOF NPs with a similar composition, the metal source used was Cu^{2+} from copper (II) nitrate trihydrate ($Cu(NO_3)_2.3H_2O$) and the ligands were benzene-1,4-dicarboxylic acid (H_2BDC), benzene-1,3,5-tricarboxylic acid (H_3BTC), and 1,2,4,5-benzenetetracarboxylic acid (H_4BTC). Herein, BDC will be used to define benzene dicarboxylic acid and BTC to benzene tri- or tetra-carboxylic acids. The following sections describe each fabrication protocol in detail.

3.1.1 Preparation of Cu-H_3BTC Crystals (Hexagon shape)

To produce $[Cu_3(BTC)_2]_n$ crystals with hexagon shapes, the following protocol was adapted from Umemura *et al.* (Umemura et al., 2011). $Cu(NO_3)_2.3H_2O$ (2.1 mg, 0.0085 mmol) and octanoic acid (118.88 mg, 0.825 mmol) were dissolved in 10 mL of butanol. The mixed solution was heated with a heat gun until a transparent solution was obtained. H_3BTC (1 mg, 0.165 mmol) was added and the mixture was heated by microwave irradiation at 413 K for 60 min. The resulting blue powder was isolated by centrifugation (Eppendorf Centrifuge 5430 R) and washed with ethanol (3x3 mL). Centrifugation was performed at 7800 rpm, at 4°C for 20 min. Then, the solutions were sonicated (Sonics Vibra-Cell) at 20% amplitude for 1 min (3 sec pulses of ultrasound, with 1 sec spacing in between each pulse).

3.1.2 Preparation of Cu-H_2BDC Crystals (Needle shape)

3.1.2.1 Preparation of ligand solution

Two solutions were prepared separately by dissolving 2-Methylimidazole (2-MIM) (40 mg) in 1 mL of water (40 mg/mL) and $Cu(N0_3)_2.3H_2O$ (10 mg) in 1 mL of water (10 mg/mL).

Then, H_2BDC (13 mg, 0.08 mol) was dissolved in 2-MIM, keeping in a 1:3.2 molar ratio, and H_2O was added to make a final volume of 4 mL. The sonication bath (Transsonic 690) was used to promote ligand dissolution in 2-MIM/H_2O. Thus, an organic ligand solution was prepared as indicated in **Table 1**, and the pH was measured.

Table 1. Volumes of 2-MIM and H_2O added to prepare the ligand solution.

Molar Ratio H_2BDC: 2-MIM	2-MIM (μL)	H_2O (μL)	pH
1:3.2	514	3486	7.84

3.1.2.2 Preparation of MOF NPs

The ligand solution prepared previously was used for the production of MOF NPs. Thus, 400 μL of pure ethanol and 400 μL of water were first added to each Eppendorf, and then, under stirring (600 rpm), 100 μL of the ligand solution and 94.5 μL of the copper solution were added at room temperature, to keep the molar ratio 1:2. The reaction mixture was stirred vigorously for an additional 8 h at room temperature. The resulting blue powder was isolated by centrifugation (Eppendorf Centrifuge 5417 R) and washed with ethanol (3x3 mL). Centrifugation was performed at 14 000 rpm, at 23°C for 10 min.

3.1.3 Preparation of Cu MOF NPs (Spherical and Square shape)

3.1.3.1 Preparation of ligand solutions

The ligand solutions were synthesized by dissolving each of the ligands [H_2BDC (16 mg, 0.096 mmol) (square shape) and H_4BTC (16 mg, 0.063 mmol) (spherical shape)] in 4 mL of dimethylformamide (DMF).

3.1.3.2 Preparation of MOF NPs with different molar ratios between the ligand and the metal

A copper solution was prepared by dissolving $Cu(N0_3)_2.3H_2O$ (50 mg) in 5 mL of DMF (10 mg/mL). First, 3 mL of DMF and 1 mL of each ligand solution prepared previously were mixed, and then different amounts of 0.04 M $Cu(N0_3)_2.3H_2O$ solution were added under stirring (**Table 2**). To explore the effect of the concentration of the metal ion, the molar ratios between the Cu (II) salt and each ligand (BDC^{2-}, BTC^{4-}) were fixed at 1:1 and 2:1, respectively. The reaction solution was stirred vigorously overnight at 80°C using an oil bath. The resulting blue power was isolated by centrifugation (Eppendorf Centrifuge 5430 R) and washed 3 times (3x3 mL), first with DMF and then with ethanol. Centrifugation was performed at 7800 rpm, at 4°C for 20 min.

Table 2. Volumes of $Cu(NO_3)_2$ added to the reaction mix according to the molar ratio established.

Molar Ratio $Cu(NO_3)_2$: BDC/BTC	$Cu(NO_3)_2$ to H_2BDC (µL)	$Cu(NO_3)_2$ to H_4BTC (µL)
1:1	604	**386****
2:1	**1208***	773

Represent the final volume values used to synthesize the *square and **spherical Cu MOF NPs, after testing both molar ratios.

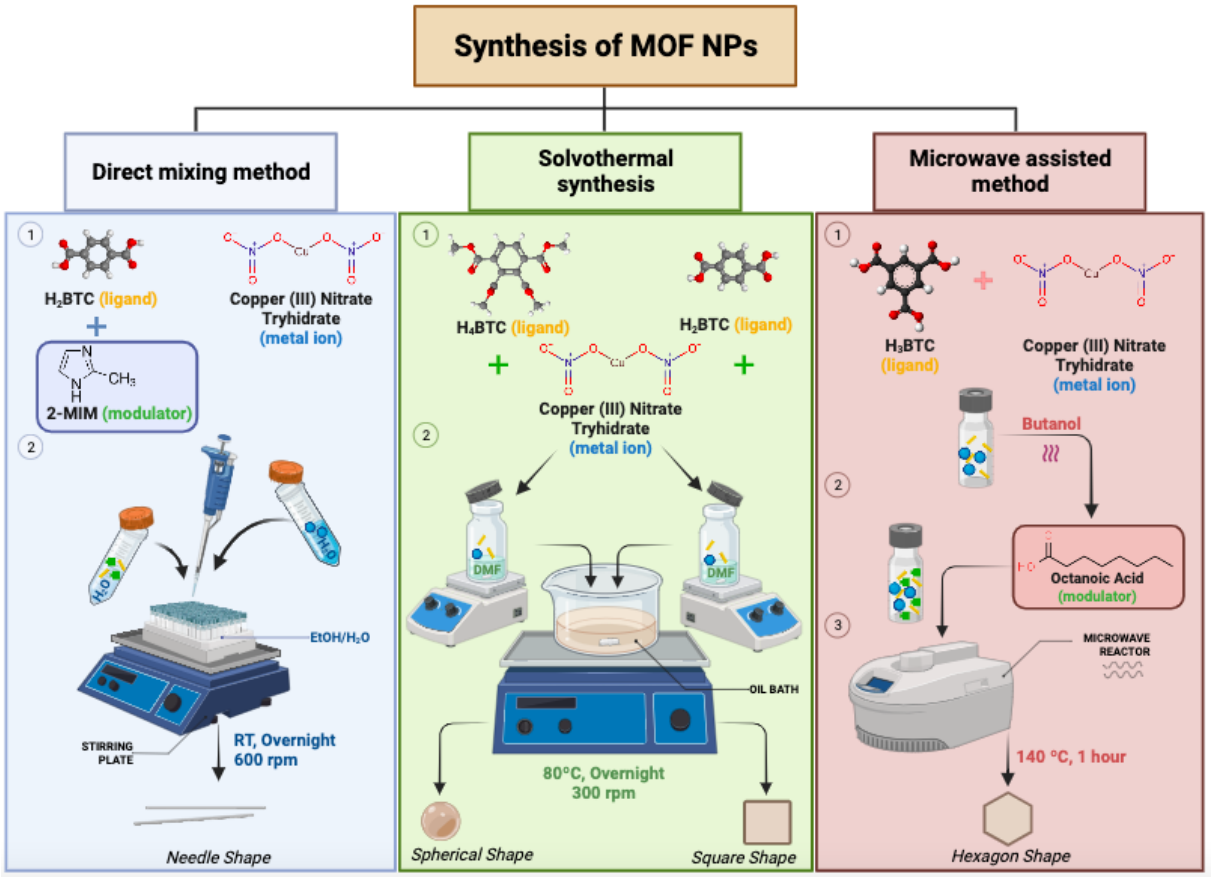

Figure 6. Schematic description of the methods used in the synthesis of Cu MOF NPs with different shapes. Created with BioRender.com.

3.2 Dynamic Light Scattering and Nanoparticle Tracking Analysis

Dynamic light scattering (DLS) is a non-invasive, well-established technique for measuring the size, size distribution, and zeta potential of molecules and particles dispersed or dissolved in a liquid, typically in the submicron region, and with the latest technology, lower than 1 nm (Falke et al., 2019). This approach involves the measurement of light

interference based on the Brownian motion of particles or molecules in suspension, and on the correlation of particle velocity with their size using the Stokes-Einstein relationship (Joudeh et al., 2022).

Nanoparticle Tracking Analysis (NTA) utilizes the properties of both light scattering and Brownian motion to obtain the hydrodynamic particle size, zeta potential, concentration, fluorescence, and colocalization of samples in liquid suspension. Each individual particle is counted and tracked in short video clips, creating accurate concentration calculations and particle size distributions. Moreover, these measurements are combined with micro-electrophoresis, for the determination of zeta potential (Joudeh et al., 2022; Malloy et al., 2006).

The properties of synthesized NPs were evaluated by DLS (Malvern ZetaSizer SZ) and NTA (ZetaView® PMX-420 QUATT equipped with the software version 8.05.19 SP3). For each assay, 3 runs were performed. NP size measurements by DLS were done at 25°C with a scattering angle of 173º and using disposable polystyrene cuvettes (Sarstedt Ag & Co., DE), while zeta potential measurements were conducted at 25°C with a period stabilization of 120 sec using a disposable folded capillary cell (DTS1070, Malvern, U.K.). NTA and DLS measurements were conducted in pure deionized water.

3.3 Transmission Electron Microscopy

Transmission Electron Microscopy (TEM) is a microscopy technique capable of providing very high-resolution images down to the scale of several Angstroms (~0.19 nm), in which a beam of electrons passes through a thin sample to produce an image. The electron beam is impacted by the sample's thickness/density, composition, and, in some cases, crystallinity. By monitoring what has happened to the beam of electrons in transit it is possible to image the fine structure (by contrast) of the sample as well as describe physical and chemical characteristics (Winey et al., 2014).

TEM was used to observe the shape of the synthesized Cu MOF NPs. Then, for TEM analysis, 10 μL of samples were mounted in a specific grid and left standing for 30 sec. The liquid in excess was removed with filter paper. The analysis was performed on a microscope from Thermo Scientific, USA and the model is Talos F200i. The grids used are Formvar/Carbon 200 Mesh, Copper (FCF200-CU-50, 50, pk) from Electron Microscopy Sciences.

3.4 Transmission Electron Microscopy and Energy Dispersive X-ray Analysis

Energy dispersive X-ray spectroscopy (EDX) is a standard method for identifying and quantifying elemental compositions in a very small sample of material. Energy dispersive X-ray systems are typically used in conjunction with electron microscopy techniques such as transmission electron microscopy or scanning electron microscopy (Bergström, 2015). EDX analysis is based on the emission of characteristic X-rays from a specimen when it is bombarded with a beam of high-energy charged particles, such as electrons or protons. When an electron from a higher binding energy level falls into a core hole, an X-ray is emitted with an energy equal to the difference in binding energies of the two levels. This process generates a spectrum that shows peaks corresponding to the elemental composition of the sample being analyzed. In addition, the elemental mapping of a sample can be created with this characterization method (Bergström, 2015; Colpan et al., 2018; Raval et al., 2019).

EDX analysis was also done with transmission electron microscopy (Thermo Scientific Talos F200) to ensure the composition mapping of Cu MOF NPs. The Super-X Detection System features 4 SDDs and Velox Software were used for the elemental analysis.

3.5 Scanning Electron Microscopy

Scanning electron microscopy (SEM) is another technique where a small amount of material may be used to determine particle size, shape, and texture. In SEM a fine beam of electrons scans across the prepared sample in a series of parallel tracks. Therefore, the electrons interact with the sample and produce several different signals which can be detected and displayed on the screen of a cathode ray tube. Moreover, since the depth of focus is so much greater than that of the light microscope, information on particle surface texture can be generated (Ferreira et al., 2018).

For SEM analysis, 10 μL of the light-blue solids stored in ethanol were dispersed and deposited on carbon adhesive tabs (77825-12 EMS) or silicon wafer chips (G3391 Agar Scientific) and then coated with chrome120 for measurement using a high vacuum sputter coater (Leica EM ACE200). The images were obtained from a ZEISS Model Supra 55 SEM system operating at 3.0 kV.

3.6 Cell Culture, Differentiation, and Exposure

The murine macrophage cell line, RAW 264.7 (twentieth passage), was cultured in DMEM Glutamax (Gibco) supplemented with 10% (v/v) heat-inactivated fetal bovine serum (FBS) and 1% (v/v) penicillin-streptomycin (PS). Cells were grown in 75 cm^2 cell culture flasks (Greiner CELLSTAR) and were maintained at 37°C, in a 5% CO_2 and 100% humidity incubator (Eppendorf CellXpert C170), with sub-culturing occurring approximately every 2-3 days. Thus, cells were passaged after reaching 90% confluence, detached with a cell scraper, and subcultivated in a 1:20 ratio in T-75 flasks.

The cell lines HeLa (Lacks' cervical cancer cells) and HEK 293 (human embryonic kidney 293 cells) were cultured in T-75 culture flasks (Greiner CELLSTAR) in DMEM Glutamax (Gibco) supplemented with 10% (v/v) FBS and 1% (v/v) PS. Every 2 days, the culture medium was changed to a fresh medium of the same type until confluence reached 70-80% and kept in the same conditions as the initial ones. The two types of cells were incubated at 37°C in a humidified 5% CO_2 incubator (Eppendorf CellXpert C170). After reaching 70-80% confluence, cells were passed onto new culture flasks. The culture supernatant was discarded, and the monolayer was washed twice with the addition of 10 mL of PBS solution. Then, 2 mL of Trypsin was added, and the T flask was taken to an incubator at 37°C, where it was kept for 2 minutes. After checking the cell detachment under the microscope, the process was stopped by adding 8 mL of supplemented culture medium, and the cell suspension was homogenized using a serological pipette and transferred to a centrifuge tube. The centrifugation process was performed at 1000 rpm for 5 min. After centrifugation, the supernatant was discarded, and the cells were diluted in 5 or 10 mL of DMEM, according to the pellet formed.

The THP-1 cell line (human monocytic leukemia cell) was cultured in an RPMI 1640 GlutaMAX medium (Gibco) supplemented with 10% (v/v) FBS. Cells were cultured at a density of 150,000 cells per mL in a humidified incubator at 37°C and 5% CO_2. For the experiments, the cells were differentiated into macrophage-like (M0 state) cells by cultivation in a culture medium supplemented with 100 nM phorbol-12-myristate-13-acetate (PMA) for 24 h. Then, the PMA-containing medium was removed, and the cells were washed with culture medium and incubated for 24 h in a complete medium without PMA.

3.7 Cell Viability Assay

Cell viability of all cell lines used (RAW 264.7 cells, THP-1 cells, HeLa cells, and KEK 293 cells) after 24 h and 48 h incubation, with different concentrations of Cu MOF NPs was evaluated (**Figure 7**). The viability assay used evaluates metabolic activity and is called "AlamarBlue". The AlamarBlue assay uses resazurin as a REDOX (reduction-oxidation) indicator that changes color in response to cellular metabolic reduction. When cells are respiring and metabolically active, resazurin is reduced to its pink fluorescent form, resorufin. The intensity of the fluorescence produced is directly proportional to the number of living cells present. Therefore, AlamarBlue is a reliable indicator of cell health because it measures the level of oxidation occurring during respiration, which allows for the quantitative determination of cell viability and cytotoxicity.

Viability tests were carried out in 96-well plates (Greiner CELLSTAR). Cells at 80% of confluence, were previously seeded overnight before the experiment at a density of 5×10^3 cells/well in 100 μL of culture medium. For cell cultures, the differently shaped particle suspensions were prepared in complete culture media consisting of DMEM supplemented with 10% (v/v) FBS and 1%(v/v) antibiotic solution and were sonicated and briefly vortexed to resuspend the particles prior to the cell culture study. The particle suspensions were sonicated using a bath sonicator (Transsonic 690). Cells were allowed to attach and achieve approximately 80% confluence prior to starting the experiments. Then, cells were exposed to different MOF NP concentrations (10 μg/mL, 25 μg/mL, 50 μg/mL, 75 μg/mL, 100 μg/mL, 150 μg/mL, and 200 μg/mL) during 24 and 48 h at 37°C.

To study the effect of NPs composition on RAW 264.7 cells, the same procedure was repeated to evaluate the cell viability for different concentrations of each of the compounds (metal ion, ligand, and modulators) used in synthesizing Cu MOF NPs. Specifically, 10 mg of copper nitrate and 2-MIM (modulator) were dissolved in 1 mL of supplemented medium with 10% FBS and 1% PS and then diluted to reach the desired concentrations (10 μg/mL, 25 μg/mL, 50 μg/mL, 75 μg/mL, 100 μg/mL, 150 μg/mL, and 200 μg/mL). For the linker, H_4BTC, and the capping agent, octanoic acid, as they can't dissolve in an aqueous solution, initially 2 mg of each component was dissolved in 10 μL of Dimethylsulfoxide (DMSO) and then diluted with supplemented medium to established different concentrations. Hence, since DMSO is toxic to the cells, its concentration was maintained below 0.1% when the compound was

finally added to the culture.

After incubation, supernatants were removed, and cells were washed twice with Phosphate Buffered Saline (PBS) to eliminate dead cells and cellular debris. To perform the assay, 100 µL of a 9:1 (v/v) mixture of supplemented medium and AlamarBlue reagent, respectively, was added to each well and mixed for 2 minutes. After 1h incubation at 37°C and 5% CO_2 in a cell culture incubator (protected from direct light), the emitted fluorescence was detected using a plate reading luminometer (BioTek Synergy H1 Plate Reader). The fluorescence was read using a fluorescence excitation wavelength of 540–570 nm (peak excitation is 570 nm) and a fluorescence emission at 580–610 nm (peak emission is 585 nm). Thus, the cell viability can be calculated based on the fluorescence (**Eq.1**):

$$\text{Cell viability (\%)} = \frac{\text{sample} - \text{blank}}{\text{positive control} - \text{blank}} \times 100 \ (\mathbf{Eq.1})$$

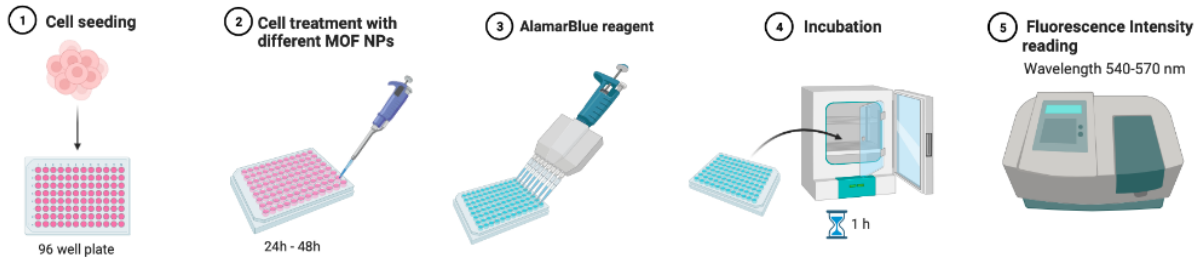

Figure 7. Cell Viability assay protocol. Created with BioRender.com.

3.8 RAW 264.7 Morphological Analysis

To assess the effect of different shapes of Cu MOF NPs on RAW 264.7 macrophage cellular morphology, the cells were photographed under an inverted microscope (Leica DM IL) after 24 and 48 h of incubation.

3.9 Flow Cytometry Analysis of CD206 and CD86 Expression

Flow cytometry is a technology that rapidly analyzes single cells as they flow past single or multiple lasers while suspended in a buffered salt-based solution. Each cell is analyzed for visible light scatter and one or multiple fluorescence parameters. Visible light scatter is measured in two different directions, the forward direction (Forward Scatter or FSC) which can indicate the relative size of the cell, and at 90° (Side Scatter or SSC) which indicates the

internal complexity or granularity of the cell. Light scatter is independent of fluorescence. Samples are prepared for fluorescence measurement through transfection and expression of fluorescent proteins (*e.g.*, Green Fluorescent Protein, GFP), staining with fluorescent dyes (*e.g.*, Propidium Iodide, DNA) or staining with fluorescently conjugated antibodies (*e.g.*, CD3 FITC) (McKinnon, 2018).

RAW 264.7 cells (2×10^5 cells/mL) were seeded in 6-well plates and treated with four different types of MOF NPs at 75 μg/mL for 24 and 48 h. Then, cells from all groups were collected and washed once with cold PBS. After being washed, cells were blocked and then incubated for 20 min at 4°C in a dark room with APC-conjugated CD86 and FITC-conjugated CD206. Followed by washing twice with stain buffer, and the cell polarity was measured by flow cytometry. The results were acquired using a FAC Scan platform (Agilent NovoCyte Quanteon Flow Cytometer) and analyzed with FlowJo v10 software. This analysis has been performed on the cells in triplicate.

3.10 Real-time PCR Analysis of Gene Expression in RAW 264.7 cells

Reverse transcription-polymerase chain reaction (RT-PCR) is a variant of polymerase chain reaction (PCR) that is commonly used to amplify and quantify specific RNA molecules. RT-PCR involves two steps: reverse transcription and PCR amplification. In the reverse transcription step, RNA is converted into complementary DNA (cDNA), using a reverse transcriptase enzyme. The cDNA is then amplified using PCR with specific primers that target one or more genes of interest. RT-PCR is highly sensitive and can be used to quantify RNA from very small sample sizes, including individual cells (Bridge, 2017).

3.10.1 PCR primers

Real-Time quantitative PCR was conducted to detect the transcriptional levels of CD86, CD206, iNOS, and Arg1 in RAW 264.7 cells. These primers were selected for evaluation based on the high frequency of their use in other related studies (Lu et al., 2020). The transcriptional levels of target genes were normalized to that of glyceraldehyde-3-phosphate dehydrogenase (GAPDH). The primer sequences of CD86, CD206, iNOS, Arg1, and GAPDH that were used for RT-PCR were presented in **Table 3**. Unfortunately, due to unknown reasons, the iNOS primer didn't work properly. The detailed protocol is described below.

Table 3. Primers of genes used in the qRT-PCR analysis.

Primer	Forward 5'-3'	Reverse 5'-3'
CD86	TGGTTCTGTACGAGCACTATTT	GTAGAGTCCAGTTGTTCCTGTC
CD206	GTGGTCCTCCTGATTGTGATAG	CACTTGTTCCTGGACTCAGATTA
iNOS	GAACGGAGAACGTTGGATTTG	TCAGGTCACTTTGGTAGGATTT
Arg1	TGGTGTGGTGGCAGA GGTCCA	ACTGCCAGACTGTGGTCTCCACC
GAPDH	GCATCCTGGGCTACACTGAG	TGGTCCTCAGTGTAGCCCAAG

3.10.2 RNA Extraction and cDNA Synthesis

Total RNA was extracted from the treated and control RAW 264.7 cells using InviTrap® Spin Universal RNA Mini Kit and stored at −80°C until required. NanoDrop 1000 Spectrophotometer (Thermo Scientific) was used to measure the concentration and purity of the isolated RNA. Then, the RNA samples with OD_{260}/OD_{280} ratios between 1.8 and 2.2 and a total amount of 0.5μg were used for cDNA synthesis to ensure the precision of the trial. The cDNA was synthesized from the RNA using reverse transcriptase and the iScript™ Bio-Rad cDNA Synthesis Kit, by following the manufacturer's instructions. The complete reaction mix was incubated in a thermal cycler (Bio-Rad iCycler®) using the protocol presented in **Table 4**.

Table 4. Reaction Protocol used for cDNA synthesis.

Cycle Step	Reaction Conditions
Priming	5 min at 25°C
Reverse Transcription	30 min at 42°C
RT inactivation	5 min at 85°C
Optional step	5 min at 4°C

The synthesized cDNA was stored at −20°C, until use for subsequent reaction.

3.10.3 Quantitative Real-Time PCR Analysis

The qRT-PCR reactions were set up using cDNA (6 µL), forward/reverse primer (0.8 µL), DNase-free water (1.6 µL) and iQ™ SYBR® Green Supermix (5 µL), according to the manufacturer's instructions. The obtained cDNA was diluted 1:20 with DNase-free water. Then, the reaction mix was pipetted in the plate using a pipetting robot specifically developed for qPCR setup (Corbett CAS-1200™). The reactions were carried out in a 384-well PCR reaction plate, which was centrifuged briefly and introduced in a CFX384™ Real-Time system (BIO-RAD), using the following program: 3 minutes at 95°C, 10 seconds at 95°C, 30 seconds in a range of temperatures from 61.5°C to 68.5°C (step repeated 40 times), and 5 seconds ranging from 65°C to 95°C for 60 times. All the sample analyses were performed in duplicate.

3.10.4 Gene Expression Data Analysis

The relative gene expression values were calculated as fold changes compared to the untreated control, normalized to a reference gene (GAPDH), through $\Delta\Delta$Ct method using Microsoft Excel. The threshold cycle (CT) is the cycle at which the fluorescence level reaches a certain amount (the threshold). This method directly uses the CT information generated from the qPCR system to calculate relative gene expression in target and reference samples, using a reference gene as the normalizer. Housekeeping genes are commonly used as reference genes because their expression levels remain relatively stable in response to any treatment (Rao et al., 2013). Data are presented as $2^{-\triangle\triangle Ct}$. A fold change of 1 indicates no difference in gene expression, while a fold change greater than 1 indicates upregulation and a fold change less than 1 indicates downregulation.

3.11 Enzyme-linked Immunosorbent Assay (ELISA)

ELISA is a highly sensitive laboratory technique used to detect and quantify soluble substances like proteins, peptides, hormones, and antibodies in a sample. This method relies on the interaction between antibodies and antigens to produce a measurable result. Antibodies are proteins produced by the immune system that have specific regions that bind to specific antigens. Antigens are proteins that can come from some foreign sources and can trigger an immune response when bound to an antibody. In an ELISA, the antigen (target molecule) is first immobilized on a solid surface (microplate) and then complexed with an

antibody that is linked to a reporter enzyme. Detection is achieved by measuring the activity of the reporter enzyme after it has been incubated with a substrate that produces a measurable product. The most crucial element of an ELISA is a highly specific antibody-antigen interaction (Engvall, 2010; Shah et al., 2016).

RAW 264.7 macrophage cells were incubated with the four different types of MOF NPs at 75 μg/mL for 24 h. After 24 h, the culture media were collected and stored at −80°C, until further used to evaluate differences in cytokine release by cells exposed to the differently shaped NPs. The supernatants were tested for the production of pro-inflammatory cytokines, TNF-α and IL-12, and anti-inflammatory cytokines, IL-4 and IL-10, using an ELISA kit (PeproTech TMB ELISA Buffer Kit), following the manufacturer's instructions. The optical density (OD) at 450 nm was determined on a plate reader.

3.11.1 Plate Preparation

The sandwich ELISA starts with a capture antibody coated onto the wells of the plate. It is termed a "sandwich" because the antigens are sandwiched between two layers of antibodies (capture and detection antibodies). Hence, the capture antibody, specific for each cytokine, was first diluted with PBS, according to the manufacturer's instructions, and 100 μL of the diluted solution was added immediately to each ELISA plate well. After adding the capture antibody to the plates, the plates were covered and incubated overnight at room temperature. Once the step was completed, the plates were washed 4 times of any potential unbound antibodies. Each wash consisted of adding 300 μL wash buffer per well, followed by aspiration. After the last wash, the plate was inverted to remove the residual buffer and blot it on a paper towel. Afterward, a 300 μL of blocking buffer was added to each well and the plate was incubated for at least 1 hour at room temperature. Finally, the plate was rewashed 4 times with PBS before the addition of the antigen.

3.11.2 Elisa Protocol

3.11.2.1 Standard/Sample

After washing, 100 μL of standard solutions of each cytokine kit or of the cell culture supernatant samples were added to each well, in triplicate, of the antibody-coated ELISA plates, and incubated for at least 2 h at room temperature, to allow cytokines to bind to the capture antibody.

3.11.2.2 Detection

The plate was rewashed 4 times to remove unbound reactants. Afterwards, 100 µL of the primary detection antibody was immediately added to each well and incubated for another 2 h at room temperature to allow the binding to the captured cytokines, followed by a buffer wash.

3.11.2.3 Avidin-HRP Conjugate

Then, the secondary enzyme-conjugated antibody was added to each well. For that, Avidin-HRP conjugate was diluted 1:2000 in diluent and 100 µL was added per well, followed by incubation for another 30 minutes at room temperature.

3.11.2.4 ABTS Liquid Substrate

The plate was rewashed another 4 times, and 100 µL of the substrate solution (ELISA Colorimetric 2,2'-Azinobis [3-ethylbenzothiazoline-6-sulfonic acid]-diammonium salt (ABTS) reagent) was added to each well, to produce a color change, and incubated at room temperature for 20 minutes, protected from light. During this process, a colored product is formed which allows to indirectly determine the cytokine concentration of each analyzed sample. The color development was monitored with an ELISA plate reader (BioTek Synergy H1 Plate Reader) at 450 nm with a wavelength set at 620 nm.

3.12 Statistical Analysis

Between one and three independent assays were performed for each experiment with three or more replicates per condition. The graphs and statistical tests were executed in GraphPad Prism (version 9.4.0, GraphPad Software) and all results presented in graphs include means $\pm$ standard deviations (SD). The statistical significance of differences between the means of individual groups was calculated using a one-way or two-way analysis of variance (ANOVA) with Dunnett's post hoc test. A *p-value* of ≤0.05 was considered statistically significant. The significant differences between the groups are represented in the graphs by the asterisk (*), where *p<0.05, **p<0.01, ***p<0.001 and ****p<0.0001.

4. Results & Discussion

4.1 Nanoparticle Preparation and Characterization

The physicochemical characterization of NPs intended for immunology research is important as it helps to explain the observed immunological effects. More importantly, it relates the physicochemical and immunological properties to draw meaningful conclusions. Moreover, some of those properties can also influence the biocompatibility, biodistribution, clearance, and immunotoxicity of the nanosystems. Therefore, the physicochemical parameters like size, surface charge (zeta potential), compositional analysis, and morphology are commonly measured to characterize NPs (Clogston, 2021).

In this work, to get differently shaped MOF NPs, some reaction conditions and synthesis methods were modified as described in **Chapter 3** (*Materials and Methods*), while the metal source and the carboxylate ligands remained unchanged. Consequently, Cu MOF NPs properties depend on different parameters like reaction time, temperature, type of solvent, agitation speed, molar ratios between the Cu (II) salt and each carboxylate ligand, and the addition of modulators/capping agents, among others.

Thus, four differently shaped MOF NPs, exhibiting hexagon (**Figure 8A**), needle (**Figure 8B**), square (**Figure 8C**), and spherical (**Figure 8D**) shapes, were obtained. As the magnified TEM images show, the synthesized Cu MOF NPs were highly dispersed, and each revealed a uniform shape with a controlled size (from approximately 250 to 500 nm).

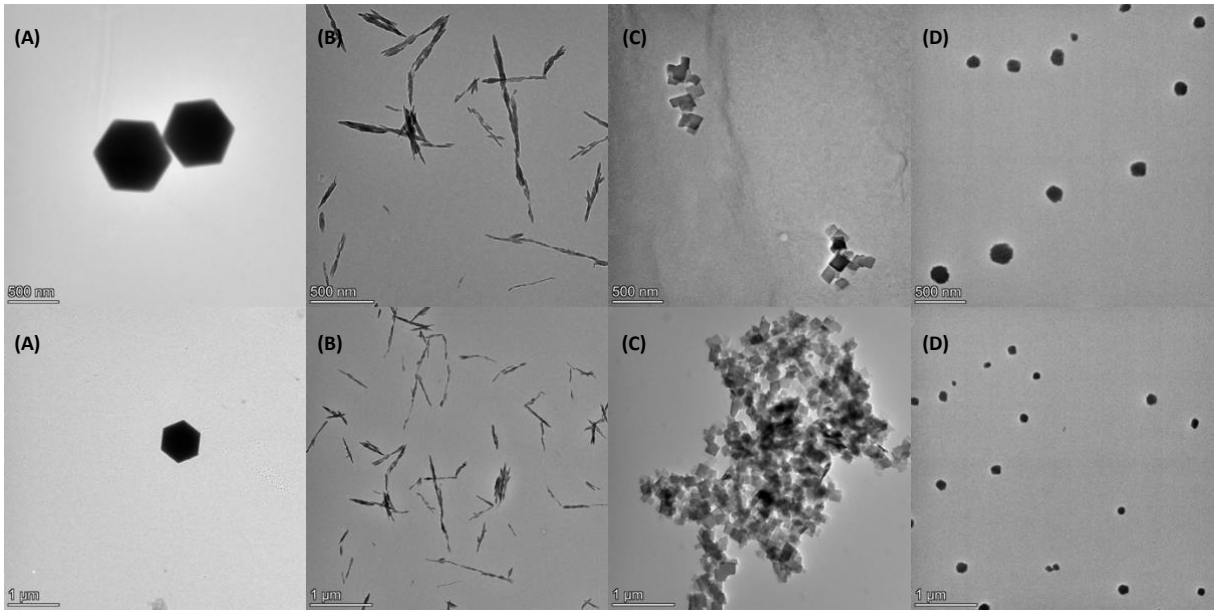

Figure 8. TEM images of different Cu MOF NPs, including (A) Hexagon, (B) Needle, (C) Square, and (D)

Spherical shapes (scale bars: 500 nm and 1 μm).

The synthesis of shape-controlled MOF crystals usually depends on the specific control over MOF nucleation and growth (Guo et al., 2018). The reaction of copper nitrate with a carboxylate ligand gives slow nucleation and then faster crystal growth, which inherently results in $[(Cu)_n(BDC/BTC)_2]_n$ with a better-defined shape (Umemura et al., 2011).

The synthesized hexagon and needle Cu MOF NPs involved the addition of different modulators to get their shapes.

In the case of hexagon MOF NPs, the shape was achieved using octanoic acid as an additive (modulator), which perturbs the coordination between Cu-BTC, thus leading to the anisotropic crystal growth (**Figure 9**). Previous studies suggest that the competitive interaction brought by the monocarboxylic additive leads to the alteration of the nucleation process (Umemura et al., 2011). In fact, when adding octanoic acid as a modulator of the growth process, the attachment of the growth unit is perturbed due to the competition between the modulator and one of the carboxylates in the BTC ligand at the attachment event. At the concentration used of octanoic acid, it seems that all the edges equally grow, *i.e.*, the growth rate on each edge appears to be constant throughout the growth, resulting in hexagonal 2D MOF NPs.

A different modulator (2-methylilimidazole) was incorporated into the needle MOF synthesis process. 2-MIM not only can act as a base to promote the rapid growth of crystals, by accelerating the deprotonation of H_2BDC, but also can serve as a competitive ligand to prevent further growth of the crystal (Guo et al., 2018). Thus, in the presence of 2-MIM, more deprotonated H_2BDC ions were available for coordination with metal ions, resulting in nanosized crystals with a limited and regulated rate of framework extension (or face-selective modulation, **Figure 9**), provided by the competitive effect, which culminates with needle-shaped crystals.

In both cases, the use of modulators also improves the crystallinity of MOF NPs by enhancing the reversibility of MOF formation (Chen et al., 2022), a fact that is comported by TEM images for these two shapes of Cu MOF NPs that appear darker due to the fewer electrons transmitted through these samples, which means higher crystallinity. In addition, modulators may also physically prevent crystal's aggregation, which leads to anisotropic growth (Łuczak et al., 2023).

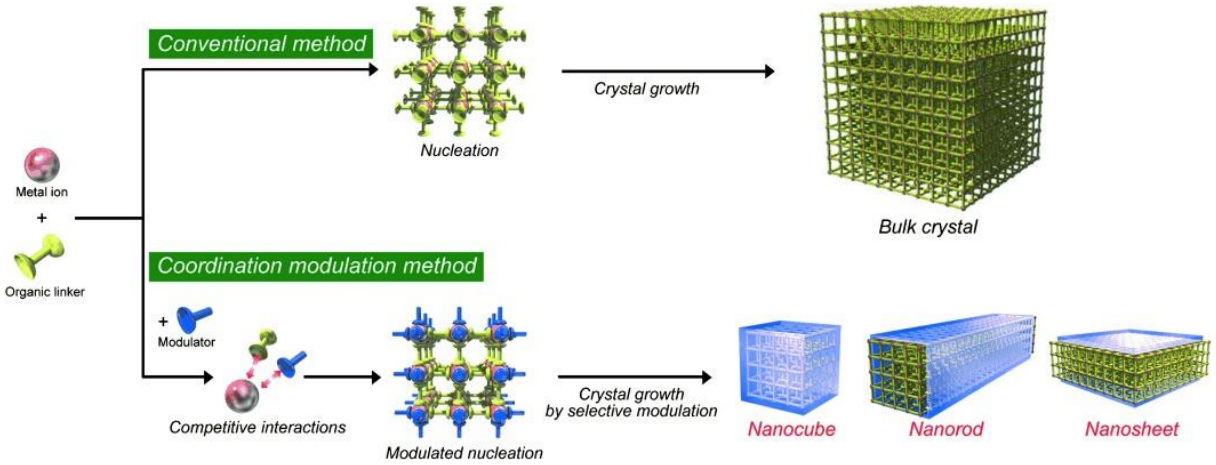

Figure 9. The role of chemical modulators for fabricating MOF nanocrystals. Taken from Tsuruoka et al., 2009. Copyright 2009, Wiley-VCH.

Regarding the synthesis process of spherical and square Cu MOF NPs, without any modulators involved, the only existing differences were the molar ratio between the cupric ions and the ligand and the number of carboxylic groups of the BTC/BDC ligand used in each one, a dicarboxylic ligand in the case of square shape and a tetracarboxylic linker for spherical shape.

Considering the synthesized square Cu MOF NPs, as shown in **Figure 10A**, the copper (II) ions are joined by benzene dicarboxylate ligands, resulting in a two-dimensional square network structure.

Changing the organic linker from linear BDC to quadrangular BTC resulted in a change in Cu MOF shape, which exhibits a spherical-like shape. The use of linker H_4BTC is relatively less reported, probably because, for steric reasons, all of the four carboxyl groups are unlikely to engage in coordination with metal ions (Cao et al., 2002). Yet, through carefully manipulating the reaction conditions (*e.g.*, the molar ratio between the metal ion and the linker), H_4BTC was shown as a versatile building block for the construction of metal-organic complexes through complete or partial deprotonation of its carboxyl groups (**Figure 10B**). Indeed, spherically shaped NPs were obtained by adjusting the metal-ligand molar ratio to 1:1, which differs from that used for square-shaped NPs (2:1).

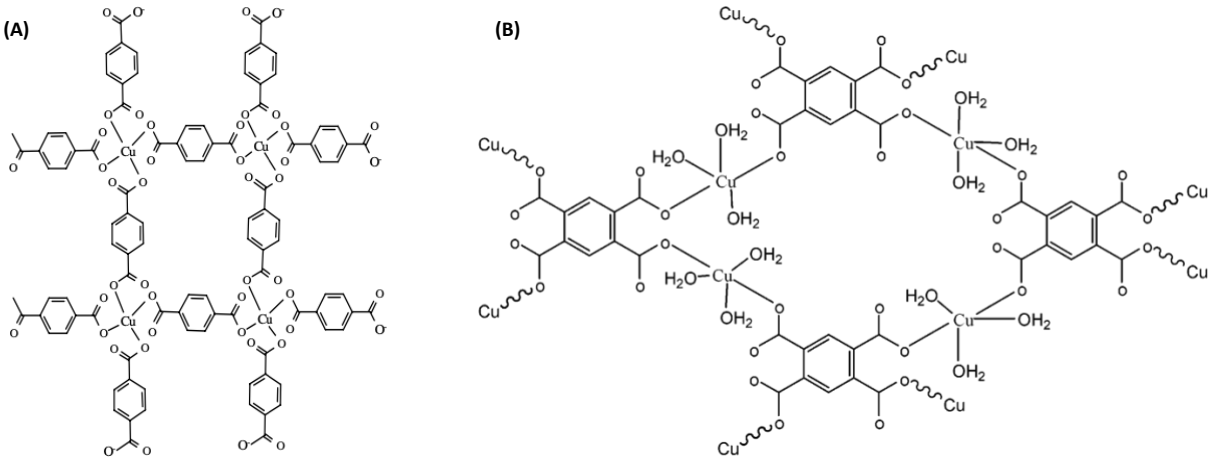

Figure 10. The proposed structure for the synthesized (A) square ("Synthesis, Characterization and Comparative Study of Copper and Zinc Metal-Organic Frameworks," 2013) and (B) spherical (R. Cao et al., 2002) Cu MOF NPs.

The properties of Cu MOF NPs obtained were characterized by NTA revealing a size range from 200 to 400 nm (**Table 5**), which was consistent with TEM results. Moreover, all four Cu MOF NPs were negatively charged when dispersed in water and there were no significant differences in particle concentration between the differently shaped NPs (around 10^{11} particles/mL) when using the same mass concentration of stock solutions, thus offering an ideal system to address the sole impact of Cu MOF NPs shape on macrophage phenotype modulation. DLS was also selected to measure the size and the zeta potential of spherical NPs, 230.9 nm and −14.30 mV, respectively, confirming the measured values by NTA. While spherical particles are described by a single-size parameter, for non-spherical NPs, several dimensions are needed to fully report their dimensions. Although the DLS and NTA methods in their pure form are not suitable for measuring such NPs, since quite often these instruments only measure at one or two angles (Arenas-Guerrero et al., 2018; Doncom et al., 2017), they allow an indirect measurement of the characteristics of liquid dispersions (Monakhova et al., 2023). Thus, in addition to allowing the observation of NPs shape, TEM is an instrument more sophisticated and able to measure in different ranges of angles, which can give advanced information, such as better analysis of multi-modal particle size distributions and information on the interaction between the particles (Monakhova et al., 2023).

Table 5. Cu MOF NPs sizes, zeta potential, and concentrations from NTA. Data are presented as means ± SD.

Group	Size (nm)	ζ Potential (mV)	Concentration* (particles/mL)
Hexagon	392.8 ± 50.3	-23.9 ± 0.4	1.7×10^{11}
Needle	307.5 ± 48.4	-18.8 ± 0.2	2.3×10^{11}
Square	218.1 ± 23.5	-14.4 ± 0.0	2.1×10^{11}
Spherical	170.7 ± 44.7	-11.8 ± 0.7	0.6 ± 10^{11}

* For all the four different types of MOF NPs, the concentration in terms of the number of particles per mL was calculated from a stock solution with a concentration of 75 μg/mL.

The morphological and textural structures of these Cu MOF NPs are further confirmed by comparing their SEM images with those of TEM. Since the main objective of performing SEM analysis was to give a 3D overview of the synthesized MOF NPs, the SEM images of spherical and square Cu MOF NPs were not included here as it was not possible to detect individual NPs and to image them. Only images of NP aggregates were collected, despite the use of sonication to disrupt them, not allowing access to their 3D structure. These aggregates can be related to the synthesis method since these two types of Cu MOF NPs were synthesized by the solvothermal method and without the use of modulators that, as previously mentioned, are well known to improve the crystallinity of materials and to prevent their aggregation.

Both low and high-magnification SEM images (**Figure 11**) show that the samples are highly homogeneous. As could be seen from the **Figure 11A**, the prepared hexagon MOF NPs possessed a truncated octahedron 3D structure, exhibiting faces with hexagonal shapes with the length of each edge around 500 nm, and a clearly very smooth surface, indicating their high crystallinity. Accordingly, the high magnification of **Figure 11B** shows that the prepared needle Cu MOF NPs presented typical lengths ranging from 300 to 500 nm with a smooth surface, very low thickness, and sharp vertices.

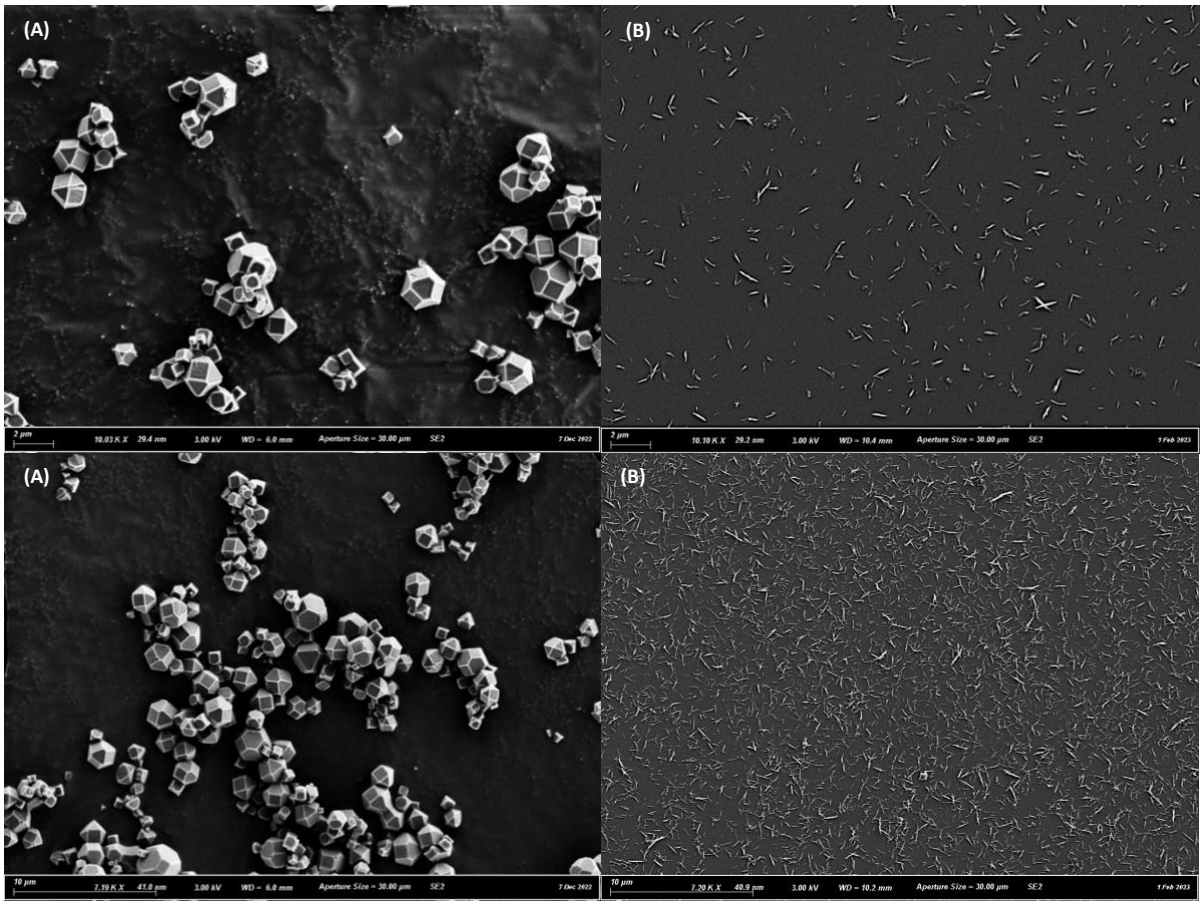

Figure 11. SEM images of different Cu MOF NPs, revealing (A) Hexagon and (B) Needle shapes (scale bars: 2 and 10 μm).

Then, TEM-EDX analysis was employed to analyze the chemical compositions of the as-prepared Cu MOF NPs. **Figure 12** shows the mapping results for each component elemental, confirming the composition of the material. Indeed, several key elements including Cu (Copper), C (Carbon), O (Oxygen), and S (Sulfur) were all identified in the spectrum. The presence of Mo (Molybdenum) in all the samples is derived from the molybdenum grids used for characterization. These findings suggest the successful formation of Cu MOF NPs in agreement with previous studies (Lee et al., 2022; Yusuff et al., 2019).

The EDX spectrum shows the high purity of the synthesized Cu MOF NPs along with oxygen content which indicates the formation of copper particles. The absence of other elements in the EDX spectrum also confirms the purity of Cu MOF NPs.

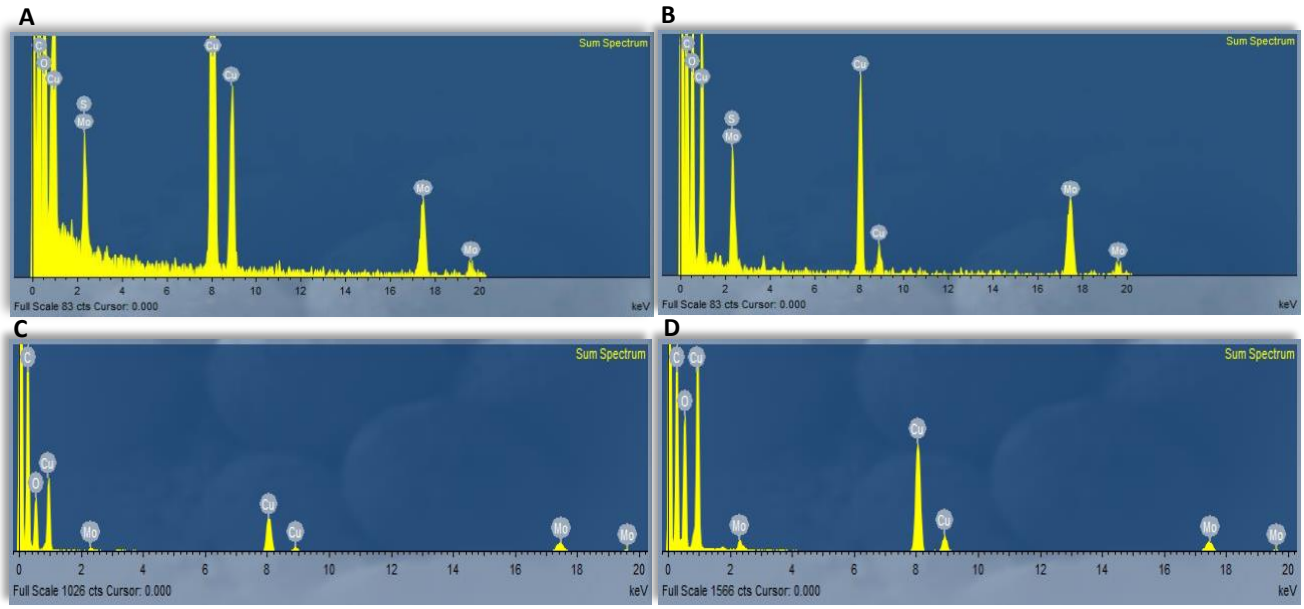

Figure 12. TEM-EDX analysis of Cu MOF NPs with different shapes: (A) Hexagon, (B) Needle, (C) Square, and (D) Spherical shapes.

These results indicated that these four Cu MOF NPs exhibited very similar physicochemical properties except shape and thus would be ideally suited for studies aimed at assessing the impact of shape on a given biological activity.

4.2 Cell Viability Studies

In vitro effects of Cu-based MOF NPs were studied by AlamarBlue assay, in a wide range of concentrations (from 10 to 200 μg/mL), using four distinct cell lines, namely a cancerous cell line (HeLa), a human embryonic kidney cell line (HEK 293) usually used as a normal cell line, a human monocytic cell line (THP-1) following differentiation using PMA, the most widely used model for primary human monocytes/macrophages, and a macrophage-like, leukemia virus-transformed murine macrophage cell-line (RAW 264.7) that is commonly used as the model of mouse macrophages (Li et al., 2021). All types of Cu MOF NPs were very well dispersed in an aqueous solution – a complete culture medium.

4.2.1 The effect of Cu MOF NPs on RAW 264.7 cells

The cell viability of macrophages is significantly impacted by the materials, sizes, and surface modifications of inorganic NPs as the result of differences in cellular uptake and physiological functions (Cheng et al., 2019). To investigate the cytotoxicity, a resazurin assay was performed to assess the cell viability of RAW 264.7 macrophages upon exposure to Cu

MOF NPs for 24 h and 48 h with a wide dose range of 0 - 200 μg/mL. Overall, as shown in **Figure 13**, all four differently shaped Cu MOF NPs reduced the cell viability of RAW 264.7 macrophage cells at higher doses for both time points.

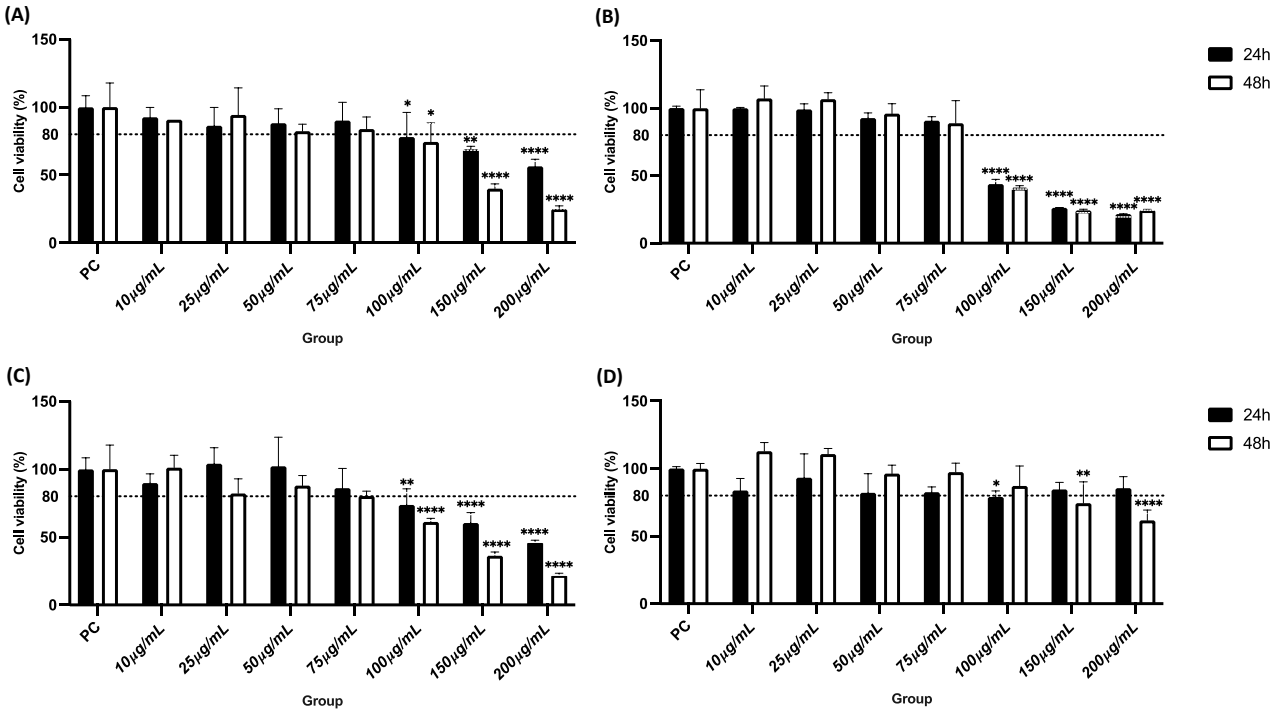

Figure 13. *In vitro* cell viability assay (AlamarBlue) of RAW 264.7 cells treated with (A) Square, (B) Needle, (C) Spherical, and (D) Hexagon NPs. RAW 264.7 cells were treated with various concentrations of Cu MOF NPs for 24 h and 48 h. The dashed line defines the cytotoxicity range: non-cytotoxicity > 80%. The data are presented as means ± SD (n=4). (**p*<0.05; **p*<0.01; *****p*<0.0001).

Regardless of the broad spectrum of Cu MOF shapes, increasing NPs concentrations caused only a statistically significant decrease in RAW 264.7 cell viability in a range of concentrations above 75 μg/mL. These findings indicated that, until this concentration value, the exposure to NPs did not affect the cell's metabolism based on the quantification of resorufin, which is proportional to the number of viable cells, when compared with the control cells. Therefore, 75 μg/mL is the maximum and "safe" concentration to be used of all four differently shaped NPs that was selected to proceed with further experiments.

Additionally, as shown in **Figure 13B**, cells treated with needle-shaped MOF NPs retained high cell viability (above 80%) under a dosage of 75 μg/mL, but it dramatically fell to lower than 50% at 100 μg/mL both at 24 h and 48 h. In contrast, there was no such evident cytotoxicity of hexagon Cu MOF NPs in RAW 264.7 cells when exposed at concentrations higher than 75 μg/mL, demonstrating that the hexagon shape can significantly reduce the

cytotoxicity against cells. Also, square and spherical Cu MOF NPs showed a similar toxicity profile, being more toxic than hexagonally shaped NPs and less toxic compared to needle-shaped NPs. The greater cytotoxicity effects exhibited by needle-shaped NPs at lower concentrations are probably highly related to ambient exposure damage. According to the literature, three probable cytotoxicity mechanisms of Cu MOF NPs via (1) attachment to cell membranes, (2) penetration into the cell, and (3) penetration into the nucleus are proposed based on their shape (Jeevanandam et al., 2020). Consistently, several shape-dependent toxicity studies found that needle-shaped NPs induced lysosomal membrane disruption, caused lysosome enlargement, and subsequently the activation of caspase-3 and DNA damage, both of which eventually led to cell apoptosis (Hao et al., 2022; Zhang et al., 2017). In fact, in a relevant study, particle-cell association and cellular uptake were investigated on BEAS-2B and RAW 264.7 cells after synthesizing the hydroxyapatite NPs with four shapes, including needle, plate, sphere, and rod shapes (Zhao et al., 2013). Results showed that the cytotoxic potential of nanomaterials changed dramatically as the shape of NPs was altered to that which a phagocytic cell has difficulty processing (*e.g.*, less rounded shapes with more defined shapes), resulting in lysosomal disruption. In their study, Zhao *et al.* also showed that needle-shaped hydroxyapatite NPs induced higher ROS levels in RAW 264.7 cells, which according to the literature is directly related to cell apoptosis (Zhao et al., 2013). The impact of the shape of cerium oxide NPs on their *in vitro* cellular toxicity was also studied with macrophages from the RAW 264.7 cell line (Forest et al., 2017). As before, results showed that rod NPs induced a significant and dose-dependent lactate dehydrogenase (LDH) release, which is associated with the loss of cell membrane integrity, whereas that triggered by octahedron particles did not differ from that observed for control cells (Forest et al., 2017). However, the biological response often depends on the cellular context, especially the pH (Franchi et al., 2015) and the difference in sensitivity between cell types (Forest et al., 2017). For this reason, the toxicity of Cu MOF NPs was further studied in different cell lines.

4.2.2 The effect of each compound used on Cu MOF NPs synthesis on RAW 264.7 macrophage cells

To explore the possible involvement of Cu MOF composition, the cytotoxicity effect of each individual compound present in MOF NPs in RAW 264.7 macrophage cells, was assessed. Since the only difference between the carboxylate ligands used in the synthesis of

the differently shaped MOF NPs was the number of carboxyl groups, the cytotoxicity study was only performed for the ligand with a higher number of this functional group, H_4BTC, potentially with more toxic effects than the others.

As shown in **Figure 14**, the most evident viability change occurred in RAW 264.7 cells exposed to the metal ion (cupric ions). Definitely, cell viability was decreased along with the increasing doses of copper nitrate (**Figure 14A**), which is consistent with previous studies, suggesting the dose-dependent cytotoxicity of metal ions (Cao et al., 2012; Taira et al., 2011). The highest dose of copper that could be used without being significantly toxic to RAW 264.7 cells was 50 μg/mL, although until 150 μg/mL the viability was around 80% (see dashed line in the graph), a threshold percentage to be considered as non-cytotoxicity (López-García et al., 2014). Contrarily, no statistically significant changes were found in the cytotoxicity of the 2-MIM modulator in RAW 264.7 cells over a range of concentrations up to 150 μg/mL (**Figure 14B**). Similar results appeared in the study of cytotoxicity effects of carboxylate ligand (**Figure 14C**) and monocarboxylic modulator (**Figure 14D**) in RAW 264.7 cells. In fact, both treated groups preserved a high cell viability (~100%) until a concentration of 200 μg/mL.

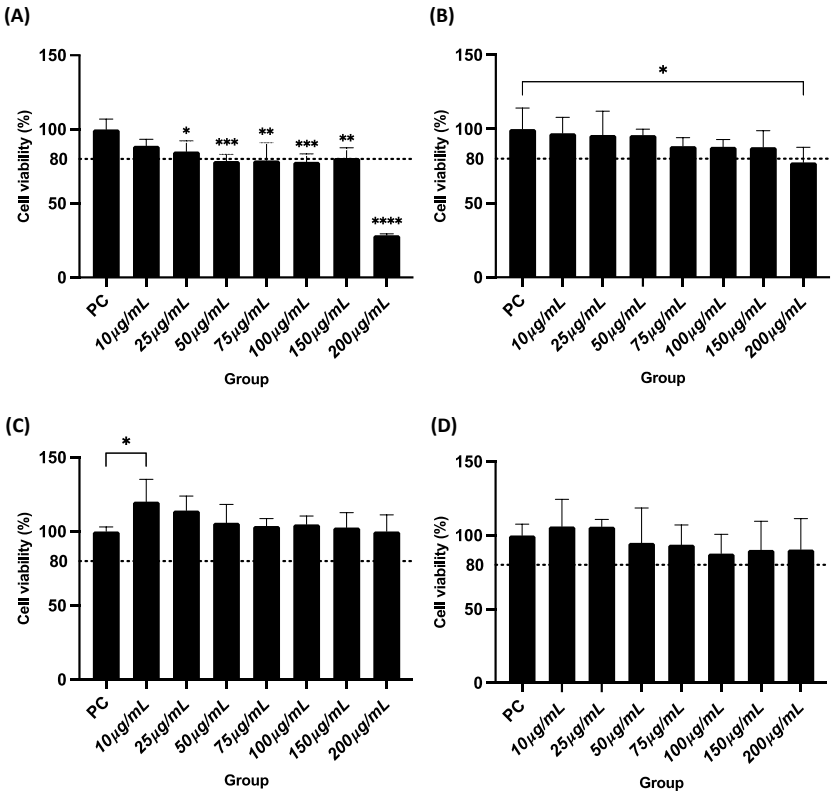

Figure 14. *In vitro* cell viability assay (AlamarBlue) of RAW 264.7 cells treated with each component

used in the synthesis of Cu MOF NPs: (A) Copper Nitrate as metal ion (B) 2-MIM as modulator (C) H_4BTC as ligand (D) Octanoic Acid as capping agent. The dashed line defines the cytotoxicity range: non-cytotoxicity > 80%. The data are presented as means ± SD (n=4). (*p<0.05; **p<0.01; ***p<0.001; ****p<0.0001).

4.2.3 The effect of Cu MOF NPs on THP-1 cells

To fully analyze the effects on macrophages, both mouse and human cell models were selected to evaluate the different tolerances and responses to the stimuli. Therefore, to investigate the effects of Cu MOF NPs on human THP-1-derived macrophages stimulated by PMA, cell viability was also assayed. After treatment with 100 nM PMA for 24 h, cells were further incubated with Cu MOF NPs for 24 h and 48 h. As shown in **Figure 15**, qualitatively distinct results were obtained for differentiated THP-1 cells and for RAW 264.7 cells.

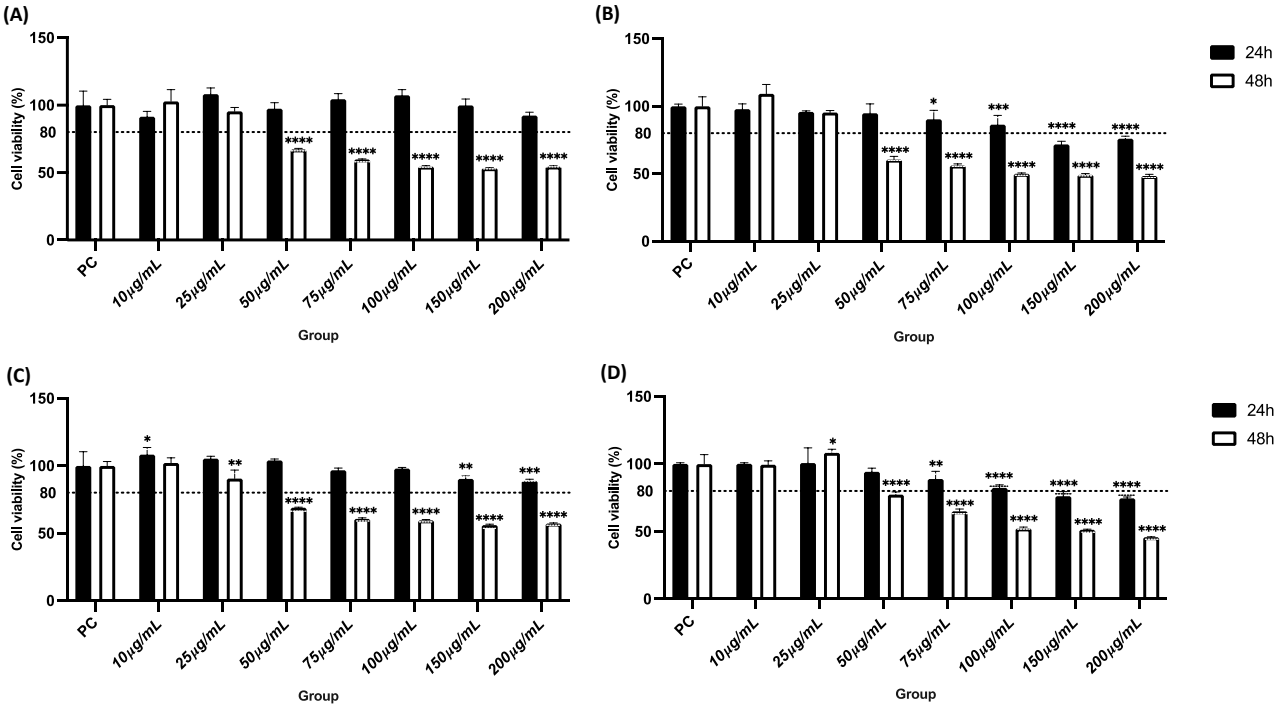

Figure 15. *In vitro* cell viability assay (AlamarBlue) of THP-1 cells treated with (A) Square NPs, (B) Needle NPs, (C) Spherical NPs, and (D) Hexagon NPs. THP-1 cells were treated first with PMA (100 nM) for 24 h and then with various concentrations of Cu MOF NPs for 24 h and 48 h. The dashed line defines the cytotoxicity range: non-cytotoxicity > 80%. The data are presented as means ± SD (n=4). (*p<0.05; **p<0.01; ***p<0.001; ****p<0.0001).

In general, cell viability of all treated groups decreased in a dose and time-dependent manner. During the first 24 h, increasing Cu MOF NPs concentrations caused a negligible decrease until 75 µg/mL, with square and spherical-shaped Cu MOF NPs being the least toxic

(**Figures 15A** and **15C**). Treatment with needle and hexagon Cu MOF NPs in the first 24 h of culture, on the other hand, slightly reduced the total number of viable cells at 75 μg/mL, with noticeable weak cytotoxic effects at higher concentrations (just below 80%), thus revealing more cytotoxic effects on cells (**Figures 15B** and **15D**). Otherwise, when differentiated THP-1 cells were further incubated with all four groups of Cu MOF NPs for 48 h, the cell viability dropped statistically significantly at 50 μg/mL, showing that Cu MOF NPs were toxic at lower concentrations to THP-1 cells than to RAW 264.7 cells, not only because exists interspecies heterogeneity but probably due to a lower proliferation rate of differentiated THP-1 cells (Aldo et al., 2013). Indeed, PMA treatment of THP-1 cells leads to a more mature phenotype with a lower rate of growth (Aldo et al., 2013; Browne et al., 2022). Furthermore, considerable differences were already observed between mouse and human macrophages (Li et al., 2021; Saas et al., 2020), which might be due to the origin of macrophages (Monnier et al., 2022). Overall, previous studies suggested that the increased glycolysis characteristic of murine macrophages with mitochondrial dysfunction appears to play a role in cell survival (Vijayan et al., 2019).

4.2.4 The effect of Cu MOF NPs on HeLa cells

To validate the use of Cu-based MOF NPs for potential biomedical applications, toxicity assessment against normal HEK 293 cells and human cervical cancer cell line HeLa was also performed.

Surprisingly, when comparing the current viability study to the previous ones, the Cu MOF NPs on HeLa cells showed a lack of time-dependent effects on cytotoxicity. In the initial 24 h culture, Cu MOF NPs drastically decreased the HeLa cell viability (lower than 50% at 150 μg/mL for all the treatment groups). However, as shown in **Figure 16**, a considerable increase in viability was observed after 48 h treatment, probably due to the capability of HeLa cells to divide and grow indefinitely, allowing them to bypass cellular senescence and apoptosis when exposed to Cu-based MOF treatment over time (Sheldrake, 2022). A previous study discussed that normal cells undergo proliferating on average every 24 h, while tumor cells have a deregulated cycle length (*i.e.*, 20 h). Thus, the mere loss of circadian rhythmicity is sufficient to increase the tumor cells' growth rate. (Bernard et al., 2006). Indeed, after 48 h, HeLa cells treated with all four differently shaped NPs equally presented viability higher than 70% when incubated at 200 μg/mL. Thus, shorter exposure to Cu MOF

NPs can inhibit HeLa cervical cancer cell viability. Besides, no significant changes in cytotoxicity effects were obtained between the differently shaped NPs at both time points.

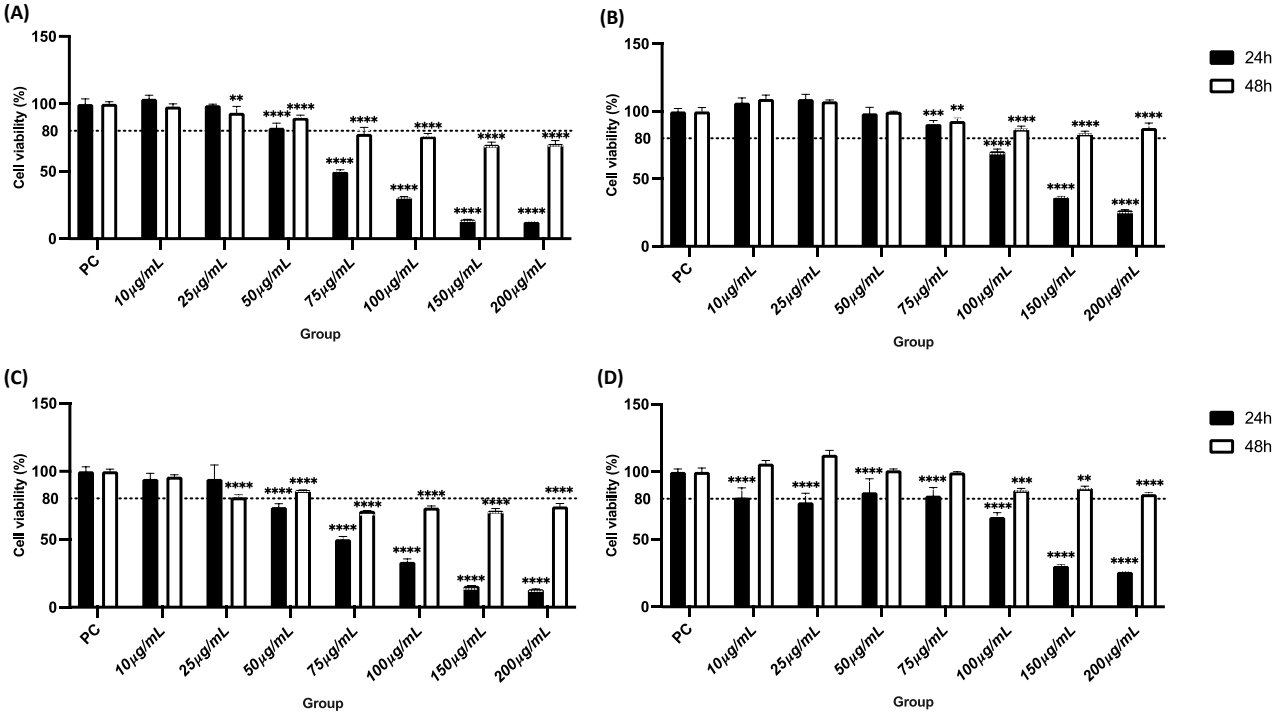

Figure 16. *In vitro* cell viability assay (AlamarBlue) of HeLa cells treated with (A) Square NPs, (B) Needle NPs, (C) Spherical NPs, and (D) Hexagon NPs. HeLa cells were treated with various concentrations of Cu MOF NPs for 24 h and 48 h. The dashed line defines the cytotoxicity range: non-cytotoxicity > 80%. The data are presented as means ± SD (n=4). (**p<0.01; ***p<0.001; ****p<0.0001).

4.2.5 The effect of Cu MOF NPs on HEK 293

Assessment of cytotoxicity to kidneys is critical in clinical practice (Liu et al., 2021). Indeed, NPs enter the body, circulate in the bloodstream, and mainly accumulate in the liver, spleen, and kidney (Tekie et al., 2020). Since urinary excretion of Cu MOF NPs is one of the available routes to clear out Cu^{2+}, the renal hazards of Cu MOF NPs should be investigated. Therefore, to identify the toxicity profile of Cu MOF NPs on normal HEK 293 cells, a cell viability assay was employed, and the results are presented in **Figure 17**.

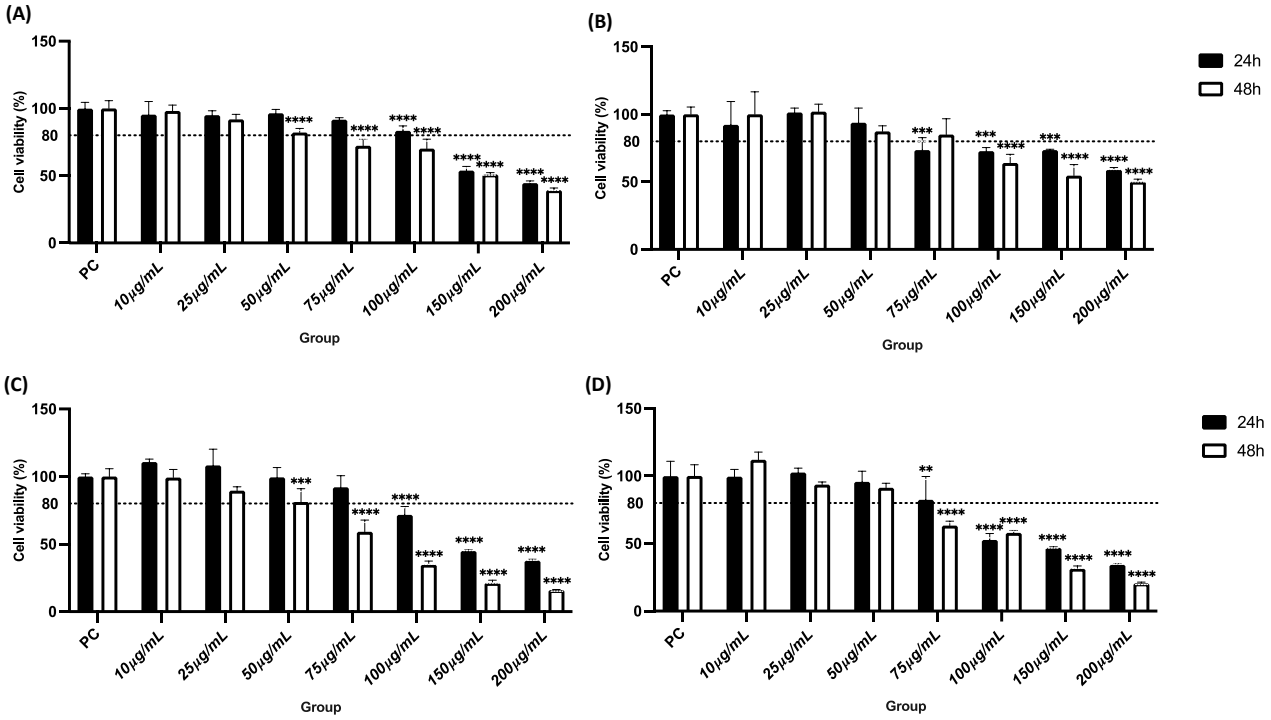

Figure 17. *In vitro* cell viability assay (AlamarBlue) of HEK 293 cells treated with (A) Square NPs, (B) Needle NPs, (C) Spherical NPs, and (D) Hexagon NPs. HEK 293 cells were treated with various concentrations of Cu MOF NPs for 24 h and 48 h. The dashed line defines the cytotoxicity range: non-cytotoxicity > 80%. The data are presented as means ± SD (n=4). (***p*<0.01; ****p*<0.001; *****p*<0.0001).

As can be seen, the above results indicated that cell viability was clearly time and concentration dependent. Overall, after 24 h of exposure, square-shaped Cu MOF NPs were observed to be less toxic to HEK 293 cells, with the cell viability above ~80% at concentrations below 100 μg/mL (**Figure 17A**). Also, during the first 24 h of incubation, HEK 293 cells seemed to be resistant to exposure at increasing concentrations of MOF NPs, exhibiting toxicity only at concentrations exceeding 75 μg/mL, except for the needle-shaped NPs treated group (**Figure 17B**), which showed statistically significant reduced cell viability at this concentration exposure. Nevertheless, spherical and hexagon NPs-treated groups (**Figures 17C** and **17D**) reached lower viability values (lower than 20%) after exposure at the highest concentrations studied, a range from 100 μg/mL to 200 μg/mL, at both 24 h and 48 h, compared with needle and square NPs-treated groups (~50% and ~40%, respectively). Thus, NPs' shape plays a crucial role in this cytotoxicity tendency. Woźniak *et al*. compared the *in vitro* cytotoxicity profiles of different shapes and sizes of bare (non-coated) AuNPs in cancer (HeLa) and normal (HEK 293) cell lines. They found that Au nanospheres had higher

cytotoxicity than star-, flower- and prism-shaped AuNPs due to a higher uptake (Woźniak et al., 2017). Given that spherical NPs are known to have higher cellular uptake in HEK 293 cells (Awashra et al., 2023; Woźniak et al., 2017), a possible interpretation for this trend is that, after a long-time interval of exposure at high concentrations, a higher cellular uptake of spherical and hexagon NPs compared with needle and square shapes can led to a greater cytotoxicity (Awashra et al., 2023). Yet, short-term exposure at lower concentrations of needle-shaped MOF NPs showed higher toxic effects than incubation with spherical and hexagon NPs. Further studies, *e.g.,* confocal microscopy analysis of cellular uptake of NPs, are required to understand this phenomenon.

An additional critical result is that, after treatment for 48 h, the Cu MOF NPs were almost three-fold toxic towards HEK 293 cells in comparison to the HeLa cells. It is worth noting that various types of cell lines can react differently after incubation with NPs (Woźniak et al., 2017). As previously reported by Woźniak *et al*., the HEK 293 cell line is more sensitive than HeLa cell line, and its viability depends on the concentration and time interval of incubation with NPs (Woźniak et al., 2017). In this experiment, Cu MOF NPs increased early cell death in HeLa cells, but only late cell death in HEK 293 cells, which is in agreement with previous studies for other types of NPs (Yang et al., 2020).

Since it was found that RAW 264.7 cells exposure to 75 μg/mL of MOF NPs for both 24 h and 48 h did not potently affect the cells, for this next series of experiences, this concentration was used as the highest safe concentration tested.

4.3 Comparison of effects of different Cu MOF NPs shapes on RAW 264.7 cell morphology and proliferation

Because the M2-like macrophages and M1-like macrophages exhibit distinct morphologies, the phenotypic transformation of macrophages can be indicated by an obvious change in cell morphology (Rodell et al., 2018). **Figures 18** and **19** show the cell morphology of the macrophage RAW 264.7 cells under treatment with Cu MOF NPs at 75 μg/mL. The cells were monitored under an optical microscope (20×) after 24 h and 48 h incubation.

Striking differences were observed among non-NP-treated cells and Cu MOF NP-treated cells. In the untreated cells (M0) (**Figure 18A**), the cell morphology generally showed a round form with a cortical ring of actin filaments, dense cytoplasm mostly in the peri-nuclear areas,

and limited cytoplasmic extensions or spreading (Dabare et al., 2023). Also, vacuoles were absent in the majority of unstimulated cells. However, most of RAW 264.7 cells treated with different shapes of Cu MOF NPs had changed to an irregular form with accelerated spreading and forming pseudopodia, and a few becoming elongated with a spindle-shaped morphology. In fact, in contrast to cells cultured in medium alone, cells incubated with Cu MOF NPs generally presented the following features: flattened stellar morphologies associated with cells presenting three or more short cytoplasmic projections or lamellipodial extensions, together with a granular cytoplasm with several vacuolations visible in many cells (Sigola et al., 2016). This morphological behavior is consistent with a pro-inflammatory phenotype (M1) (Sigola et al., 2016) and was mostly remarked at 24 h incubation (**Figure 18**) with needle-shaped Cu MOF NPs (**Figure 18E**). Indeed, these cells exhibited podosomes that have been described as zones of close contact to the substratum, which combine several key abilities including cell adhesion, matrix degradation, and mechanosensing (Neacsu et al., 2014). This suggests that the needle-like shape of NPs is prone to provoke a pro-inflammatory response, probably because it presents a challenge to macrophages attempting to engulf and clear these long and straight structures (Nel, 2023). Additionally, these qualitative morphological results indicated that, after treatment for 24 h, the number of M2 cone-shaped cells also increased, but apparently much less, in cells treated with the differently shaped Cu MOF NPs compared with the control group. This M2 macrophage morphological behavior, characterized by an elongated morphology with only two or fewer pseudopods (Yang et al., 2021), looked more obvious in the group treated with spherical Cu MOF NPs (**Figure 18D**).

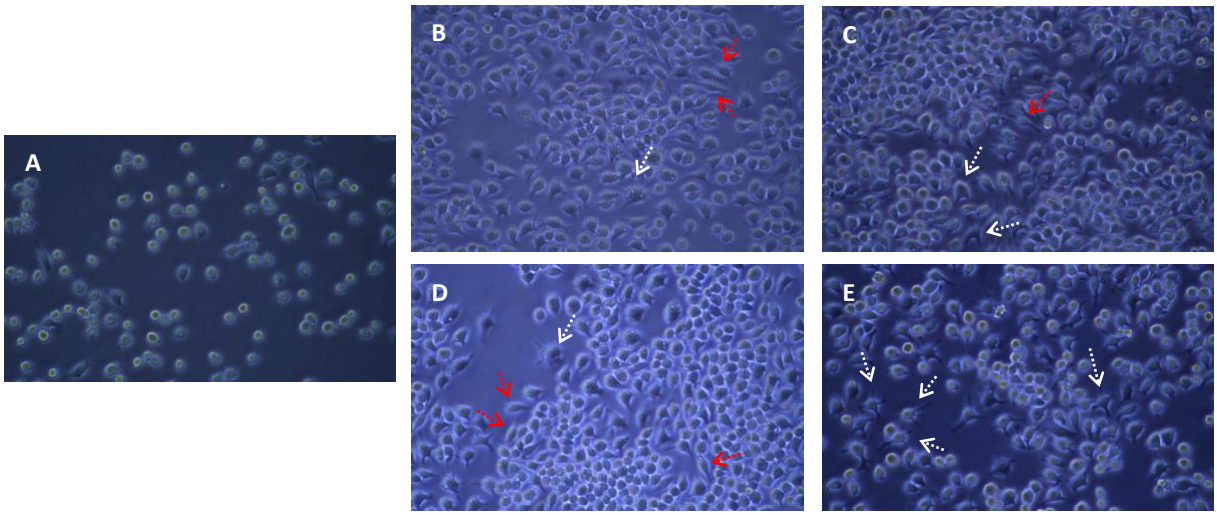

Figure 18. RAW 264.7 macrophages untreated (A). Effects of (B) Hexagon (C) Square (D) Spherical

and (E) Needle MOF NPs on RAW 264.7 macrophage cell morphology after 1 day of incubation with different Cu MOF NPs. White arrows point to M1 macrophages and red arrows indicate M2 macrophage. Images were obtained using an inverted light microscopy under phase contrast. All the micrographs in this figure were taken at the same magnification (20×).

Similarly, after 48 h, the majority of RAW 264.7 cells in the control group (without stimulation by Cu MOF NPs) were small and round (**Figure 19A**). However, more significantly in the square and needle groups, the cells showed a flat and pancake-like morphology with many synaptic structures (Yang et al., 2021) (**Figures 19C** and **19E**). On the contrary, spherical-shaped Cu MOF NPs, after 2 days of incubation, did not induce morphological changes in RAW 264.7 cells when compared with the control group (**Figure 19D**).

In conclusion, these results showed that square and needle-shaped MOF NPs induced a higher percentage of M1 macrophages and suggested that this trend was more significant after two days of culture.

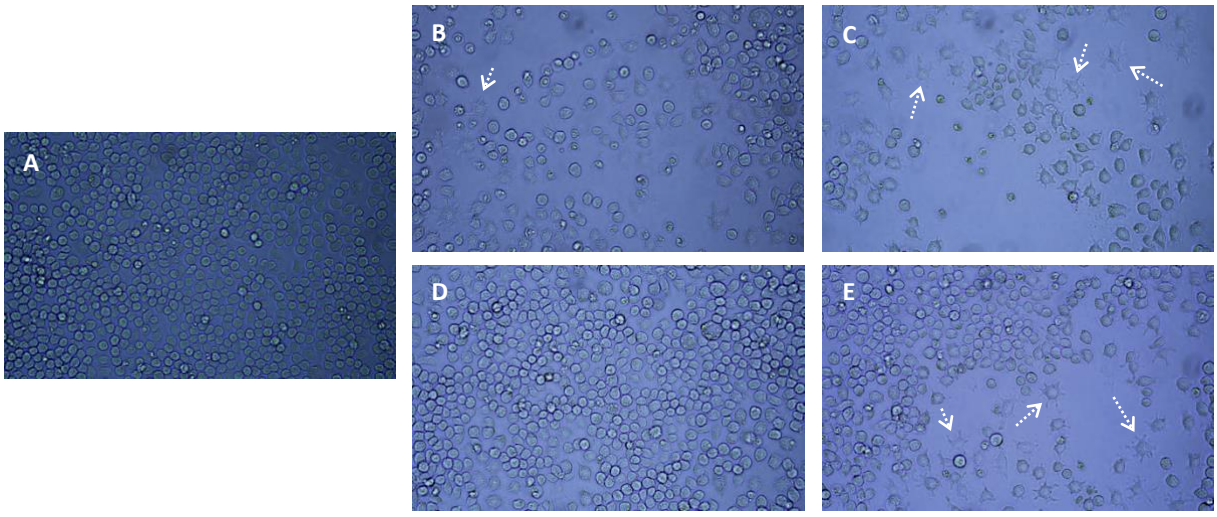

Figure 19. RAW 264.7 macrophages untreated (A). Effects of (B) Hexagon (C) Square (D) Spherical and (E) Needle MOF NPs on RAW 264.7 macrophage cell morphology after 2 days of incubation with different Cu MOF NPs. White arrows point to M1 macrophages. Images were obtained using an inverted light microscopy under phase contrast. All the micrographs in this figure were taken at the same magnification (20×).

The morphological results were qualitative, as macrophages presented a continuous spectrum between the different phenotypes. To quantify these observations, gene expression, cytokine production, and flow cytometry *in vitro* were further explored.

4.4 Real-Time PCR Analysis of gene expression in RAW 264.7 cells

The gene expression levels of the two macrophage phenotype markers in RAW 264.7 cells, determined by RT-qPCR after 24 h and 48 h of incubation with 75 µg/mL of Cu-based MOF NPs, are depicted in **Figure 20**. M1 and M2 macrophages express common or exclusive marker genes (Zhang et al., 2020). Among the top distinct genes in M1 and M2 macrophages, several studies have shown that CD86 is expressed in and used as a M1 marker, and CD206 and Arg1 as M2 markers, in both mouse and humans (Orecchioni et al., 2019; Taciak et al., 2018). Thus, these set of genes was selected to evaluate the phenotypic profile of RAW 264.7 macrophages post-incubation with Cu MOF NPs. The results are expressed as the fold change compared with the untreated control cells, *i.e.*, the ratio of gene expression between each treated group and the control group, and those genes altered at least 2-fold ($p<0.05$) were statistically different expressed (Mccarthy et al., 2009). The concentration and purity ratio (A260/280) of extracted RNA are presented in Appendix 1. The ratio of absorbance at 260 nm and 280 nm for all RNA samples was ~ 2.0, providing a rough indication of purity and considered suitable for use in cDNA synthesis.

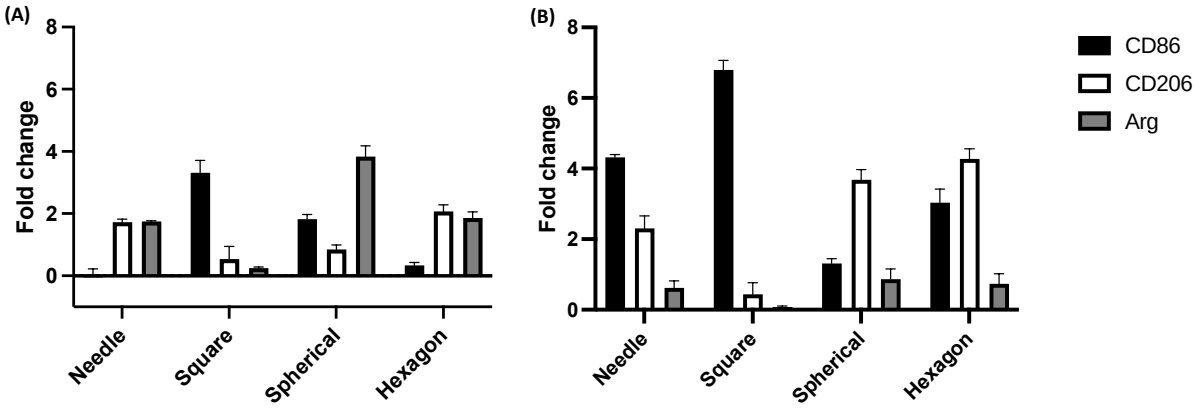

Figure 20. Histograms depicting fold change in RAW 264.7 cells gene expression, determined by quantitative real-time PCR analysis, after 1 (A) and 2 (B) days of treatment with Cu MOF NPs. An untreated condition (RAW 264.7 cells without Cu MOF NPs stimulation) was used to determine the relative expression, and the transcript expression of target genes (CD86, CD206, Arg1) was normalized to the expression of endogenous housekeeping gene glyceraldehyde-3-phosphate dehydrogenase (GAPDH).

The gene expression of CD86, representing M1 macrophages, was significantly upregulated in the group treated with square-shaped Cu MOF NPs both at days 1 and 2 of culture compared to the control group (mean fold change: 3.32 and 6.80, respectively),

while much lower levels of Arg1/CD206 gene expression (M2 macrophage markers) were induced at both time points. Likewise, compared with the untreated group, both needle and hexagon Cu MOF NPs induced relatively high levels of CD86 gene expression but only on day 2 of treatment (mean fold change: 4.32 and 3.03, respectively). Even though the expression of M2 marker genes was upregulated (around 2-fold or less) in response to needle-like Cu MOF NPs, there was not a statistically significant difference, so in cells treated with this group for 2 days was highly induced the M1-associated gene. However, after 2 days of incubation, RAW 264.7 cells treated with hexagon-shaped NPs also expressed higher levels of CD206 (mean fold change: 4.27) compared with the non-treated cells, thus coexisting the two macrophage phenotypes. By contrast, for the spherical-like Cu MOF NPs, the CD86 gene expression levels were almost consistent over time, and not statically significant (approximately 2-fold increase), lower than the expression of M2 macrophage marker genes, Arg1 at 1 day of culture, and CD206 after 2 days of treatment, that reached 3.68-fold increase.

Therefore, the above results indicated not only that RAW 264.7 cells treatment with square and needle Cu MOF NPs for 2 days clearly induced the immune response toward M1 polarization, but also that the treatment with spherical MOF NPs just promotes, in a significant way, an M2 polarization phenotype, thus revealing that a variation in shape could alter the ability of Cu MOF NPs to elicit macrophage polarization. Additionally, comparing these results with cytotoxicity analysis on RAW 264.7, it seems that the cytotoxicity of the four MOF NPs largely correlated with their respective ability to induce macrophage polarization, since it has been observed that needle-shaped Cu MOF NPs were more cytotoxic than hexagon and spherical ones. In fact, previous studies proposed that the cytotoxicity of different inorganic NPs is closely related to their impact on immunological response (Miao et al., 2017). For instance, Nishanth *et al.* reported that Au and Ag NPs with smaller sizes had a more potent effect on inducing M1 polarization than their larger counterparts, as determined by a higher expression of TNF-α and IL-6 in RAW 264.7 and J774A.1 macrophages. Also, they found that NPs cytotoxicity increased as their size decreased, which could be a reason for their size-dependent macrophage polarization (Nishanth et al., 2011; Yen et al., 2009). Thus, the degree of induced macrophage polarization toward the M1 subtype by NPs has previously been related to their greater cytotoxicity.

4.5 Cytokine Production Measure by ELISA

To assess the capability of differently shaped Cu MOF NPs to induce macrophage polarization, the cytokine release by RAW 264.7 cells was evaluated after treatment with MOF NPs at 75 μg/mL for 24 h and 48 h. The levels of pro-inflammatory cytokines (TNF-α and IL-12) and anti-inflammatory cytokines (IL-4 and IL-10) are presented in **Figure 21**. Standard curves were generated for each cytokine, by plotting the mean absorption against cytokine concentration (Appendix 2), allowing to determine cytokine concentrations for each experimental condition.

Cytokine production was roughly in line with gene expression data. As shown in **Figure 21A**, the pro-inflammatory cytokine, TNF-α, was significantly upregulated in cells treated with the square and needle Cu MOF NPs, when compared with the non-treated group, both at days 1 and 2. Likewise, the spherical Cu MOF NPs-treated group expressed higher concentrations of TNF-α compared with the control group, albeit the difference was only statistically significant at 2 days of culture. By contrast, there were no statistically significant differences in TNF-α concentration between the hexagon-shaped Cu MOF NPs-treated group and the control group, either at day 1 or day 2.

Additionally, quantified results using ELISA revealed that all four MOF NPs induced significant release of IL-12 (**Figure 21B**) at both time points, with the needle, spherical and square shapes exhibiting a stronger effect than the hexagon shape. In fact, the IL-12 levels secreted by hexagon Cu MOF NPs-treated cells demonstrated a time-dependent reduction, therefore suggesting the absence of a persistent inflammatory response.

The anti-inflammatory cytokine, IL-10 at day 1 was downregulated in all the cells treated with differently shaped Cu MOF NPs except on cells incubated with hexagon MOF NPs, where there was a statistically significant increase (**Figure 21C**). The decrease in IL-10 was more obvious and there was a statistically significant difference between the square-shaped Cu MOF NPs-treated group and the untreated group at 2 days after treatment.

The concentration of another anti-inflammatory cytokine, IL-4, was also measured (**Figure 21D**) but, in general, the concentrations were quite low, close to the recommended detection range (8 pg/mL according to the ELISA kit). Note that the maximum value of the y-axis is 20 pg/mL, unlike the other represented graphs. One possible explanation for this is that IL-4 is mainly secreted by Th2 cells as reported by many previous studies (Bao et al.,

2015). Despite that, the lowest amount of cytokine was secreted at day 1 by the RAW 264.7 cells incubated with square and spherical MOF NPs. No other statistically significant differences were observed.

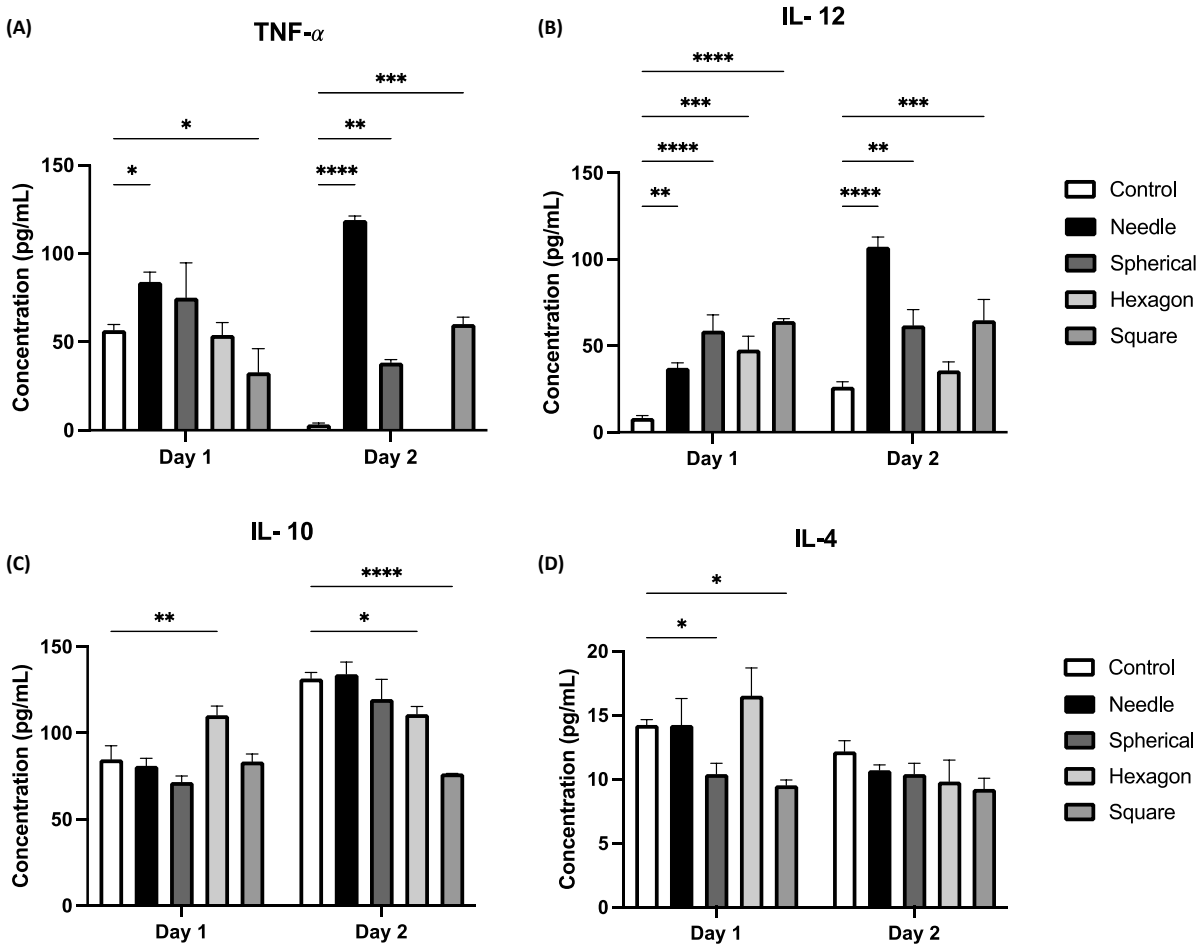

Figure 21. ELISA results of cytokine production by RAW 264.7 cells: (A) TNF-α and (B) IL-12, both pro-inflammatory cytokines; (C) IL-10 and (D) IL-4 both anti-inflammatory cytokines. The data are presented as means ± SD (n=3). (**p*<0.05; ***p*<0.01; ****p*<0.001; *****p*<0.0001).

Altogether, these data were consistent with previous observations and indicated that the treatment with square and needle Cu MOF NPs increased the secretion of two pro-inflammatory cytokines (TNF-α and IL-12) and, in the case of square-shaped NPs, significantly decreased the secretion of anti-inflammatory cytokine IL-10, which is characteristic of an upregulation of inflammation and shift toward M1 macrophage activation (Ding et al., 2023). In contrast, treatment with the hexagon-shaped Cu MOF NPs for 24 h increased anti-inflammatory cytokine secretion as compared to non-treated cells, whereas after 2 days, RAW 264.7 cells exhibited lower expression levels of anti-inflammatory cytokines.

Although the exact mechanism requires further investigation, it was hypothesized that the differential ability of the four Cu MOF NPs to modulate macrophage polarization could be not only due to the differences in cellular internalization but also to the intracellular mechanisms, including ROS generation and lysosomal damage, as reported in previous studies for other types of NPs (Baranov et al., 2021; Ding et al., 2023).

Activation of cellular signal and immune response, in turn, likely depends on the amount of NP intracellular accumulation, that is determined by NPs uptake and endocytosis by macrophage (Andrade et al., 2021). As discussed above, it was hypothesized that Cu MOF NPs shape could affect its ability to enter cells or, in other words, the endocytic uptake of NPs. For example, Li *et al*. have found that spherical glycol-nanoparticles (GNPs) were internalized more by RAW 264.7 macrophages than cylindrical GNPs. Besides that, they discovered that the differences in the endocytosis pathways between spherical and cylindrical GNPs could explain this observation (Li et al., 2016). Endocytosis is usually subdivided into two internalization mechanisms, namely phagocytosis and pinocytosis. Pinocytosis occurs in all cells through four main engulfment mechanisms, specifically macropinocytosis, clathrin-mediated endocytosis, caveolae-mediated endocytosis, and clathrin- and caveolin-independent endocytosis (Hadji et al., 2022). According to the literature, particles >0.5µm are ingested by phagocytosis, while smaller particles are internalized by endocytosis which can be clathrin or caveolin-mediated (Baranov et al., 2021). Since some of the shapes of the Cu MOF NPs synthesized (*e.g.*, needle-shaped NPs) can reach this size threshold, these three endocytic pathways (phagocytosis and clathrin or caveolin-mediated endocytosis) were hypothesized as possible routes for NPs to enter the cells. Also, Cu MOF NPs can be described by their aspect ratio (AR), which is the ratio between their length axis (axis a, see **Figure 22**) over their diameter axis (axis b) (*e.g.*, spherical-like particles AR=1). The AR is commonly used to compare different shapes of NPs (Awashra et al., 2023).

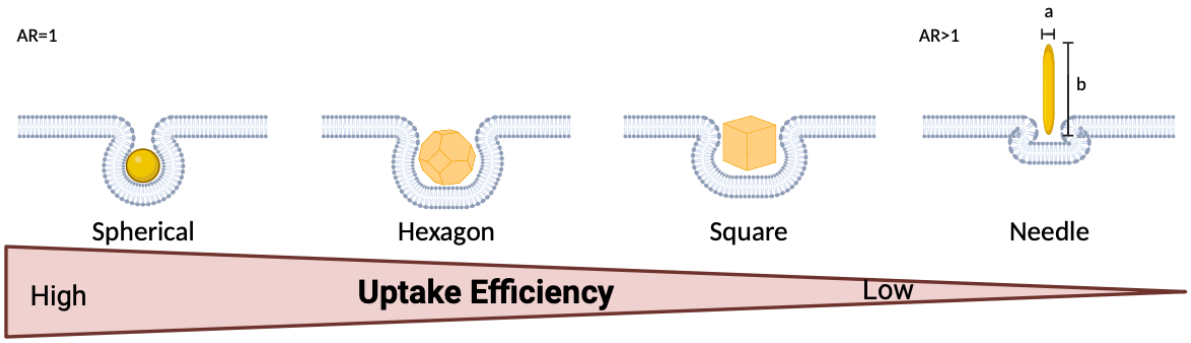

Figure 22. Theoretical predictions of uptake efficiency of spherical and non-spherical Cu MOF NPs (hexagon, square, and needle) determined by their shape. Created with BioRender.com.

During nonphagocytic endocytosis, the energy of uptake depends on the bending properties of the membrane and the strength of receptor interactions, and overall endocytosis is more efficient (lower free energy requirement) with a stronger adhesiveness and a larger contact area (Agudo-Canalejo et al., 2015). Because of this, spherical NPs are predicted to be engulfed more efficiently than needle and square NPs (**Figure 22**), since they have an optimal contact area and therefore are engulfed faster (Baranov et al., 2021). In contrast, particles with extreme shapes, characterized by either high or low ARs, probably possessed hindered uptake because of the reduced contact area, which leads to less ligand-receptor interactions, and due to the greater membrane wrapping time required for the extended NPs (Baranov et al., 2021; Li et al., 2016). Similarly, NPs with high or low ARs are expected to exhibit negligible phagocytosis compared to spherical NPs mainly due to differences in the actin structure formed when the NP interacted with the macrophage surface. In fact, when the NP attaches to the cell, actin polymerizes at points of contact but fails to create the adequate actin structure necessary to engulf the NP (Hadji et al., 2022). As a result of this frustrated uptake, it has been observed that macrophages engulfing needle-shaped crystals and fibers can end up being pierced by the needle-like structures and, consequently, start inflammation (Ernst et al., 2021). For instance, as reviewed elsewhere (Baranov et al., 2021), needle-like particles can result in inflammasome activation, as is well-understood for needle-shaped particles of titanium reticule, poly(ethylene oxide), gold and carbon, and other materials (Lebre et al., 2017; Palomäki et al., 2011). The activation of the inflammasome by needle-shaped particles depends on ROS production and cathepsin B, and although the precise mechanism and the contribution of membrane destabilization in this process are less clear, it likely relates to frustrated endocytosis/phagocytosis and the leakage

of ROS and lytic enzymes in the extracellular environment (Rabolli et al., 2016). Several studies revealed that macrophages displayed M1-like phenotypic characteristics when the inflammatory free radical levels of ROS were upregulated (Rakshe, 2018). In future investigations, to determine the uptake mechanisms of various Cu MOF NPs, specific inhibitors can be selected to treat the cells before incubation with different Cu MOF NPs.

Still, RAW 264.7 macrophages are known to register higher levels of particle uptake due to the phagocytic nature of these cells (Zhao et al., 2013). Thus, if internalized, previous studies indicated that the shape of NPs also influences the trafficking of nanomaterial inside the cell (Panariti et al., 2012). Nanoparticles' internalization, transportation, and degradation (**Figure 23**) greatly depend on the intracellular membrane structure-based organelle system such as endosomes, autophagosomes, and lysosomes. After their cell uptake, most NPs are confined in early endosomes, which mature into late endosomes and then lysosomes before exocytosis (Hadji et al., 2022). Herein, the co-localization of NPs with lysosomes sometimes causes lysosome dysfunctions with high-permeable membranes, thus releasing their containing enzymes like cathepsin B and triggering NLRP3-mediated inflammation, which contributes to M1-like polarization (Ding et al., 2023).

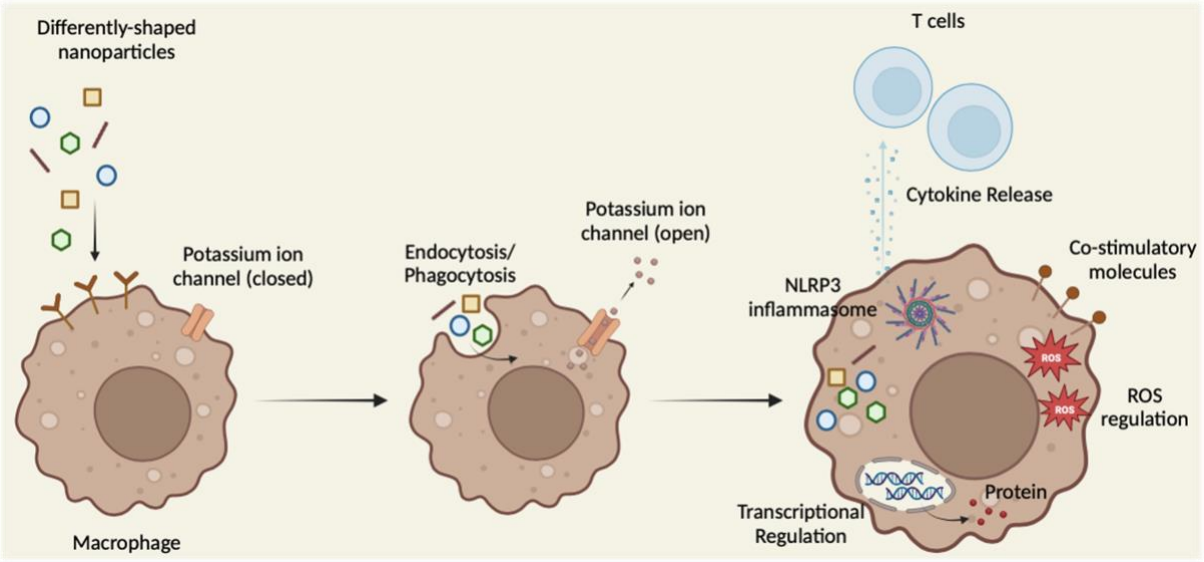

Figure 23. Schematic illustration of the shape effect of Cu MOF NPs on immune response. Created with BioRender.com.

Thus, based on the macrophage polarization data, it was also hypothesized that the needle-shaped Cu MOF NPs, defined by a critical length (*i.e.*, high aspect ratio), could induce lysosomal damage leading to triggering inflammatory cellular responses. Subsequently,

macrophage-derived cathepsins B from disturbed lysosomes may have induced IL-1β and TNF-α secretion. Although it was not investigated the function effects of lysosome injury by Cu MOF NPs, in further investigations, confocal microscopy can be used to visualize the localization of a fluorescent cathepsin B substrate in RAW 264.7 cells (Ji et al., 2012).

It is also important to note that here, macrophage polarization refers to the activation state of a macrophage at a singular point in time (Boutilier et al., 2021; Sylvestre et al., 2020). However, due to the high plasticity of macrophages, their polarization state is not fixed and can be altered based on the integration of multiple signals from other cells or environmental changes such as cytokines and growth factor secretion (Boutilier et al., 2021).

4.6 Surface Molecule Expression Assessed by Flow Cytometry

To confirm the previous results, flow cytometry was employed to assess the percentages of different macrophage phenotypes (**Figure 24**). According to the cell viability results, 75 μg/mL was the concentration used for the detection of cell polarization by flow cytometry. Cells were incubated with fluorescein isothiocyanate (FITC)-conjugated CD206 and allophycocyanin (APC)-conjugated CD86. Thus, the macrophages were identified by two specific markers, CD206 (M2) and CD86 (M1).

Firstly, the use of specific macrophage phenotype markers showed that only two days after incubation, flow cytometry revealed a significant increase in the number of CD86 and CD206 positive cells. Even so, after 24 h of incubation, the most significant differences in macrophage proportions were verified in cells incubated with square Cu MOF NPs. In fact, after being stimulated by square-like NPs, the proportion of $CD206^{+}CD86^{-}$ (M2) and $CD206^{-}CD86^{+}$ (M1) macrophages in the treated group was 9.75% and 11.4%, respectively. This change became more obvious at day 2 post-incubation.

Thus, on day 2, the square-shaped Cu MOF-treated group (**Figure 24A**) contained the lowest percentage of CD206-positive cells (M2) and a higher percentage of CD86-positive cells (M1) (61.6% and 81.8%, respectively). Likewise, as shown in **Figures 24B** and **24C**, CD86 was expressed in around 82% of RAW 264.7 cells exposed to both needle and hexagon-like NPs whereas just 74.2% of these cells expressed CD206 M2 marker. Albeit slightly higher than in square-shaped-stimulated cells, lower percentages of macrophages expressed the signature marker of M2 cells. Similar percentages of spherical-like Cu MOF NPs-treated

macrophages (**Figure 24D**) expressed both CD206 and CD86 markers (80.0% and 85.0%, respectively).

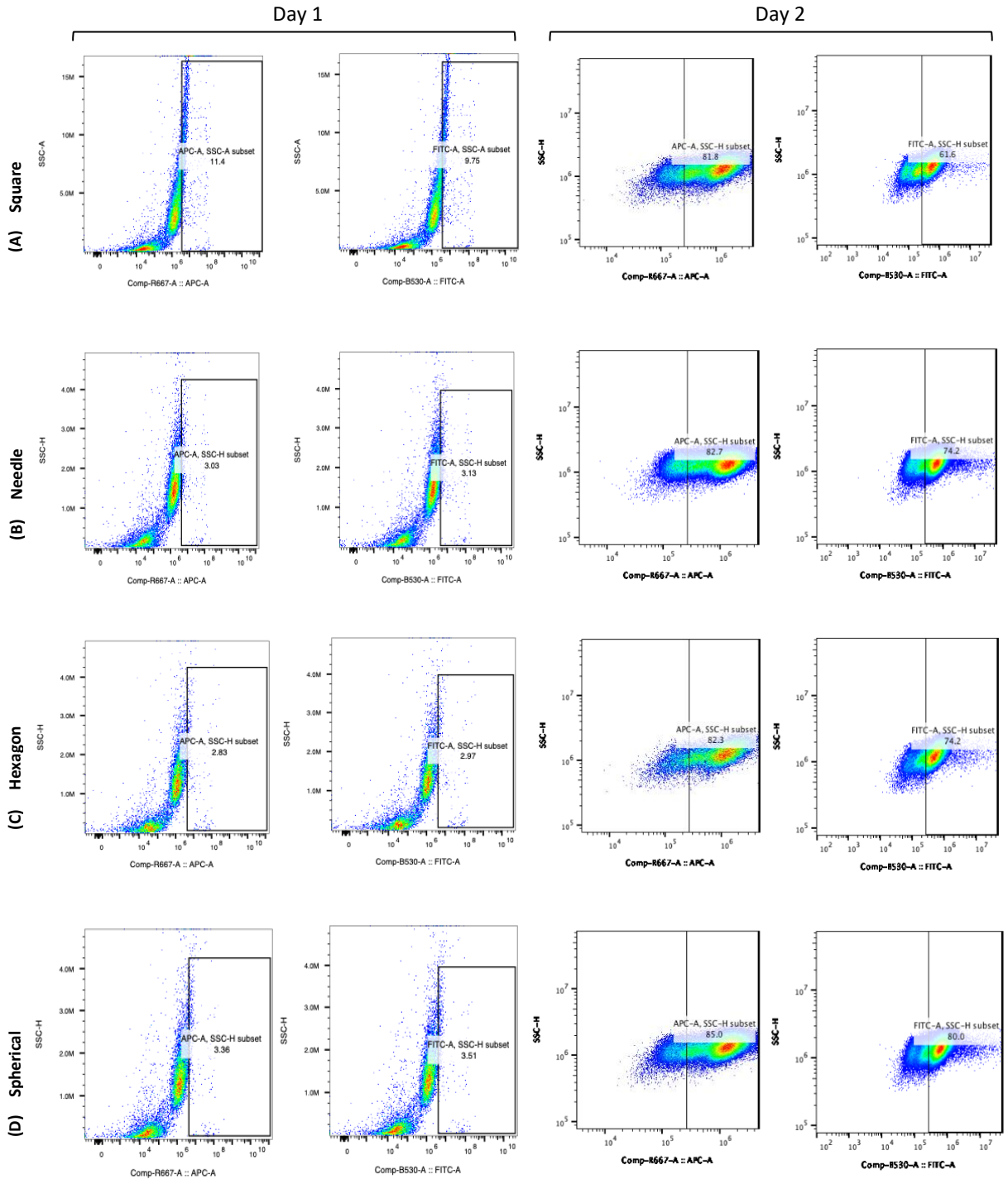

Figure 24. Multicolor flow cytometry panel to identify M1 and M2 macrophages. Flow Cytometry analysis of CD206 and CD86 expression of RAW 264.7 cells treated with (A) Square, (B) Needle, (C) Hexagon, and (D) Spherical Cu MOF NPs after 1 day and 2 days incubation. CD206 was used to identify M2 macrophages and CD86 was used to identify M1 macrophages. Cellular debris and events

too small to be cells were excluded from all events. Samples were initially gated on single cells using FSC-H/FSC-A gating, thereby excluding doubles (data not shown). From the live macrophage population, the cells were further separated based on CD206 and CD86 expression. Then, the percentages of $CD206^+$ and $CD86^+$ populations were calculated.

Altogether, these results were consistent with those obtained from the gene expression and cytokine production analysis that square-shaped MOF NPs highly induced macrophage polarization towards the M1 type, indicating that the shape of Cu MOF NPs plays crucial roles in macrophage uptake and immune response. Thus, this evidence can provide guidance for the further design of Cu MOF NPs as immunological therapeutic candidates.

5. Conclusions & Future Perspectives

The polarization of tumor macrophages can transform TAMs from a phenotype that promotes cancer growth (M2) to one that actively kills cancer cells (M1), serving as a predictive indicator of treatment effectiveness. The present project aimed to investigate the impact of shape-tunable MOF NPs for modulating macrophage phenotype, providing insights on cancer immunotherapy.

Herein, Cu MOF NPs with different shapes (needle, hexagon, square, and spherical) were fabricated by controlling synthesis compositions and conditions. It was possible to understand that various parameters influenced the shape of Cu MOF NPs, allowing precise control and fine tuning in a very wide range. While the synthesized hexagon and needle Cu MOF NPs involved the addition of different modulators to obtain their shapes, changing the organic linker from linear BDC to quadrangular BTC as well as its molar ratio with cupric ions resulted in a change in Cu MOF shape from square to spherical.

The synthesized particles were evaluated for their cytotoxicity against several distinct cell lines, including human and murine macrophage cell lines, cancer, and normal cell lines. Shape-dependent cytotoxicity of Cu MOF NPs in all the tested cell lines was observed, where needle-shaped NPs exhibited more significant cytotoxic effects at lower concentrations. The effect of each compound used in MOFs' synthesis on the viability of RAW 264.7 macrophages was also studied, indicating that, after 24 h, only copper nitrate induced significantly high toxicity (~30%) at the highest tested dose (200 μg/mL). Additionally, the *in vitro* toxicity studies showed that (1) after exposure for 48 h, the Cu MOF NPs were more toxic at lower concentrations to the human THP-1 cells than to RAW 264.7 cells, a model of murine macrophages, (2) after incubation for 48 h, the Cu MOF NPs were almost three-fold toxic towards normal HEK 293 cells comparing to the cancer HeLa cells and (3) shorter exposure to Cu MOF NPs can inhibit the viability of HeLa cervical cancer cells. A 24-hour incubation significantly reduced HeLa cell viability, whereas a notable increase in viability was observed after 48 h of treatment.

The murine macrophage cell line, RAW 264.7, was selected as the cellular model to study the impact of differently shaped Cu MOF NPs on the modulation of macrophage phenotype. The optimal concentration of all four Cu MOF NPs was also determined (75 μg/mL) by considering the biocompatible profile on tested cell lines.

Finally, the capability of differently shaped NPs to properly polarize M0 into a pro-inflammatory phenotype M1 was assessed. NPs shape was a critical determinant for Cu MOF NPs induced macrophage polarization, with the square and needle MOF NPs exhibiting significantly higher activity than the spherical and hexagon MOF NPs. Square and needle-shaped Cu MOF NPs were observed to markedly stimulate RAW 264.7 cells to release TNF-α and IL-12, pro-inflammatory cytokines, and, after 2 days of incubation, significantly increased the gene expression of CD86, representing M1 macrophages, compared with the control cells (approximately 7-fold and 4-fold, respectively). Consistently, morphological evaluation of the cells revealed small healthy round shaped cells in the control group but, groups exposed to needle-shaped Cu MOF NPs, after 2 days, induced morphological changes that included: cells revealed a flattened stellar morphology, together with three or more short cytoplasmic projections and presented a granular cytoplasm with visible vacuolations. Considering the results obtained and conclusions taken in previous studies, it was hypothesized that the differential ability of the four Cu MOF NPs to modulate macrophage polarization could be not only due to the differences in cellular internalization but also to the intracellular mechanisms, including ROS generation and lysosomal damage (Liu et al., 2018). However, given that the signaling pathways involved in macrophage activation are relatively complex, the exact mechanism for the effect of the Cu MOF shape could not be clearly elucidated and requires more detailed studies. According to our knowledge, this is the first-ever report to compare the shape-dependent effect of MOF NPs on driving macrophage polarization towards a particular phenotype. Thus, hereafter, it will be interesting, to use qualitative and quantitative methods to conclude the different endocytosis pathways involved and quantify NPs uptake and intracellular localization. For instance, one possible approach to study NP uptake by cells involves the use of chemical and pharmacological inhibitors to selectively block each type of endocytic route. Then, intracellular particle distribution can be determined using confocal laser scanning microscopy. Furthermore, oxidative stress can be evaluated by the assessment of the amount of ROS produced by cells. In future studies, in order to enhance the antitumor effect, Cu MOF NPs can be loaded with anticancer drugs, like cisplatin and doxorubicin (DOX) (Wang et al., 2022), and/or functionalized with polymer coating to improve tumor-targeting ability (Tran et al., 2023). It is also crucial to consider the potential routes of administration of MOF NPs and to study their absorption, distribution, metabolism, and excretion in relevant whole organisms *in vivo*

models, in addition to studies *in vitro*.

In conclusion, this study showed the importance of the shape of NPs in modulating macrophage phenotypes, a factor that has been often overlooked. The present work might have potential implications for the rational design of shape-adjustable Cu MOF NPs for combinatory tumor immunotherapy to yield additional or synergistic therapeutic effects.

6. References

Agudo-Canalejo, J., & Lipowsky, R. (2015). Adhesive Nanoparticles as Local Probes of Membrane Curvature. Nano Letters, 15(10), 7168–7173. https://doi.org/10.1021/acs.nanolett.5b03475

Aguilar-Guzmán, J. C., Bejtka, K., Fontana, M., Valsami-Jones, E., Villezcas, A. M., Vazquez-Duhalt, R., & Rodríguez-Hernández, A. G. (2022). Polyethylene terephthalate nanoparticles effect on RAW 264.7 macrophage cells. Microplastics and Nanoplastics, 2(1). https://doi.org/10.1186/s43591-022-00027-1

Ahmad, J., Albarqi, H. A., Ahmad, M. Z., Orabi, M. A. A., Md, S., Bandopadhyay, R., Ahmed, F., Khan, M. A., Ahamad, J., & Mishra, A. (2022). Utilization of Nanotechnology to Improve Bone Health in Osteoporosis Exploiting Nigella sativa and Its Active Constituent Thymoquinone. Bioengineering, 9(11), 631. https://doi.org/10.3390/bioengineering9110631

Ahmed, A., McHugh, D., & Papatriantafyllopoulou, C. (2022). Synthesis and Biomedical Applications of Highly Porous Metal–Organic Frameworks. In Molecules (Vol. 27, Issue 19). MDPI. https://doi.org/10.3390/molecules27196585

Aldo, P. B., Craveiro, V., Guller, S., & Mor, G. (2013). Effect of culture conditions on the phenotype of THP-1 monocyte cell line. American Journal of Reproductive Immunology, 70(1), 80–86. https://doi.org/10.1111/aji.12129

Al-Musawi, S., Albukhaty, S., Al-Karagoly, H., Sulaiman, G. M., Jabir, M. S., & Naderi-Manesh, H. (2020). Dextran-coated superparamagnetic nanoparticles modified with folate for targeted drug delivery of camptothecin. Advances in Natural Sciences: Nanoscience and Nanotechnology, 11(4). https://doi.org/10.1088/2043-6254/abc75b

Anderson, N. R., Minutolo, N. G., Gill, S., & Klichinsky, M. (2021). Macrophage-based approaches for cancer immunotherapy. In Cancer Research (Vol. 81, Issue 5, pp. 1201–1208). American Association for Cancer Research Inc. https://doi.org/10.1158/0008-5472.CAN-20-2990

Andrade, R. G. D., Reis, B., Costas, B., Lima, S. A. C., & Reis, S. (2021). Modulation of macrophages m1/m2 polarization using carbohydrate-functionalized polymeric nanoparticles. In Polymers (Vol. 13, Issue 1, pp. 1–18). MDPI AG. https://doi.org/10.3390/polym13010088

Anfray, C., Ummarino, A., Andón, F. T., & Allavena, P. (2020). Current strategies to target tumor-associated-macrophages to improve anti-tumor immune responses. In Cells (Vol. 9, Issue 1). MDPI. https://doi.org/10.3390/cells9010046

Arenas-Guerrero, P., Delgado, Á. V., Donovan, K. J., Scott, K., Bellini, T., Mantegazza, F., & Jiménez, M. L. (2018). Determination of the size distribution of non-spherical nanoparticles by electric birefringence-based methods. Scientific Reports, 8(1). https://doi.org/10.1038/s41598-018-27840-0

Astruc, D. (2016). Introduction to nanomedicine. In Molecules (Vol. 21, Issue 1). MDPI AG. https://doi.org/10.3390/molecules21010004

Awashra, M., & Młynarz, P. (2023). The toxicity of nanoparticles and their interaction with cells: an in vitro metabolomic perspective. In Nanoscale Advances (Vol. 5, Issue 10, pp. 2674–2723). Royal Society of Chemistry. https://doi.org/10.1039/d2na00534d

Bakhshi, A., Saravani, H., Sargazi, G., & Shahbakhsh, M. (2021). Ultrasound-assisted efficient synthesis of a novel Nd–MOF polymer as a new candidate for electrocatalytic activity in hydrogen storage. Journal of Applied Electrochemistry, 51(3), 399–410. https://doi.org/10.1007/s10800-020-01504-2

Bao, K., & Reinhardt, R. L. (2015). The differential expression of IL-4 and IL-13 and its impact on type-2 immunity. In Cytokine (Vol. 75, Issue 1, pp. 25–37). Academic Press. https://doi.org/10.1016/j.cyto.2015.05.008

Baranov, M. V., Kumar, M., Sacanna, S., Thutupalli, S., & van den Bogaart, G. (2021). Modulation of Immune Responses by Particle Size and Shape. In Frontiers in Immunology (Vol. 11). Frontiers Media S.A. https://doi.org/10.3389/fimmu.2020.607945

Barry, M., Pearce, H., Cross, L., Tatullo, M., & Gaharwar, A. K. (2016). Advances in Nanotechnology for the Treatment of Osteoporosis. In Current Osteoporosis Reports (Vol. 14, Issue 3, pp. 87–94). Current Medicine Group LLC 1. https://doi.org/10.1007/s11914-016-0306-3

Bastos, V. (2016). Do silver nanoparticles induce cytotoxicity and genotoxicity to skin, liver and blood cell lines?

Bergström, J. (2015). 2 - Experimental Characterization Techniques. In J. Bergström (Ed.), Mechanics of Solid Polymers (pp. 19–114). William Andrew Publishing. https://doi.org/https://doi.org/10.1016/B978-0-323-31150-2.00002-9

Bernard, S., & Herzel, H. (2006). Why do cells cycle with a 24 hour period? https://www.researchgate.net/publication/6329668

Blakney, A. K., Swartzlander, M. D., & Bryant, S. J. (2012). Student award winner in the undergraduate category for the society of biomaterials 9th World Biomaterials Congress, Chengdu, China, June 1–5, 2012. Journal of Biomedical Materials Research Part A, 100A(6), 1375–1386. https://doi.org/https://doi.org/10.1002/jbm.a.34104

Bordbar, A., Mo, M. L., Nakayasu, E. S., Schrimpe-Rutledge, A. C., Kim, Y. M., Metz, T. O., Jones, M. B., Frank, B. C., Smith, R. D., Peterson, S. N., Hyduke, D. R., Adkins, J. N., & Palsson, B. O. (2012). Model-driven multi-omic data analysis elucidates metabolic immunomodulators of macrophage activation. Molecular Systems Biology, 8. https://doi.org/10.1038/msb.2012.21

Boutilier, A. J., & Elsawa, S. F. (2021). Macrophage polarization states in the tumor microenvironment. In International Journal of Molecular Sciences (Vol. 22, Issue 13). MDPI. https://doi.org/10.3390/ijms22136995

Bridge, J. A. (2017). Reverse transcription–polymerase chain reaction molecular testing of cytology specimens: Pre-analytic and analytic factors. In Cancer Cytopathology (Vol. 125, Issue 1, pp. 11–19). John Wiley and Sons Inc. https://doi.org/10.1002/cncy.21762

Browne, E., Kavanagh, S., & Devery, S. (2022). The Cytotoxicity of Phorbol 12- Myristate 13-Acetate and Lipopolysaccharide on THP-1 Cells and an Optimized Differentiation Protocol. 5. https://doi.org/10.3390/bitap-12785

Bukowski, K., Kciuk, M., & Kontek, R. (2020). Mechanisms of multidrug resistance in cancer chemotherapy. In International Journal of Molecular Sciences (Vol. 21, Issue 9). MDPI AG. https://doi.org/10.3390/ijms21093233

Burtch, N. C., Heinen, J., Bennett, T. D., Dubbeldam, D., & Allendorf, M. D. (2018). Mechanical Properties in Metal–Organic Frameworks: Emerging Opportunities and Challenges for Device Functionality and Technological Applications. Advanced Materials, 30(37), 1704124. https://doi.org/https://doi.org/10.1002/adma.201704124

Cai, L., Xu, J., Yang, Z., Tong, R., Dong, Z., Wang, C., & Leong, K. W. (2020). Engineered biomaterials for cancer immunotherapy. In MedComm (Vol. 1, Issue 1, pp. 35–46). Blackwell Publishing Inc. https://doi.org/10.1002/mco2.8

Cao, B., Zheng, Y., Xi, T., Zhang, C., Song, W., Burugapalli, K., Yang, H., & Ma, Y. (2012). Concentration-dependent cytotoxicity of copper ions on mouse fibroblasts in vitro: Effects of copper ion release from TCu380A vs TCu220C intra-uterine devices. Biomedical Microdevices, 14(4), 709–720. https://doi.org/10.1007/s10544-012-9651-x

Cao, R., Shi, Q., Sun, D., Hong, M., Bi, W., & Zhao, Y. (2002). Syntheses and characterizations of copper(II) polymeric complexes constructed from 1,2,4,5-benzenetetracarboxylic acid. Inorganic Chemistry, 41(23), 6161–6168. https://doi.org/10.1021/ic0258577

Chen, D., Xie, J., Fiskesund, R., Dong, W., Liang, X., Lv, J., Jin, X., Liu, J., Mo, S., Zhang, T., Cheng, F., Zhou, Y., Zhang, H., Tang, K., Ma, J., Liu, Y., & Huang, B. (2018). Chloroquine modulates antitumor immune response by resetting tumor-associated macrophages toward M1 phenotype. Nature Communications, 9(1). https://doi.org/10.1038/s41467-018-03225-9

Chen, F. E., Pitt, T. A., Okong'o, D. J., Wetherbee, L. G., Fuentes-Rivera, J. J., & Milner, P. J. (2022). A Structure-Activity Study of Aromatic Acid Modulators for the Synthesis of Zirconium-Based Metal-Organic Frameworks. Chemistry of Materials, 34(7), 3383–3394. https://doi.org/10.1021/acs.chemmater.2c00241

Chen, P., & Bonaldo, P. (2013). Chapter One - Role of Macrophage Polarization in Tumor Angiogenesis and Vessel Normalization: Implications for New Anticancer Therapies. In K. W. Jeon (Ed.), International Review of Cell and Molecular Biology (Vol. 301, pp. 1–35). Academic Press. https://doi.org/https://doi.org/10.1016/B978-0-12-407704-1.00001-4

Chen, Q., Chen, J., Yang, Z., Xu, J., Xu, L., Liang, C., Han, X., & Liu, Z. (2019). Nanoparticle-Enhanced Radiotherapy to Trigger Robust Cancer Immunotherapy. Advanced Materials, 31, 1802228. https://doi.org/10.1002/adma.201802228

Cheng, J., Zhang, Q., Fan, S., Zhang, A., Liu, B., Hong, Y., Guo, J., Cui, D., & Song, J. (2019). The vacuolization of macrophages induced by large amounts of inorganic nanoparticle uptake to enhance the immune response. Nanoscale, 11(47), 22849–22859. https://doi.org/10.1039/c9nr08261a

Cheng, R., Jiang, L., Gao, H., Liu, Z., Mäkilä, E., Wang, S., Saiding, Q., Xiang, L., Tang, X., Shi, M., Liu, J., Pang, L., Salonen, J., Hirvonen, J., Zhang, H., Cui, W., Shen, B., & Santos, H. A. (2022). A pH-Responsive Cluster Metal–Organic Framework Nanoparticle for Enhanced Tumor Accumulation and Antitumor Effect. Advanced Materials, 34(42). https://doi.org/10.1002/adma.202203915

Clogston, J. D. (2021). The importance of nanoparticle physicochemical characterization for immunology research: What we learned and what we still need to understand. In Advanced Drug Delivery Reviews (Vol. 176). Elsevier B.V. https://doi.org/10.1016/j.addr.2021.113897

Colpan, C. O., Nalbant, Y., & Ercelik, M. (2018). 4.28 Fundamentals of Fuel Cell Technologies. In I. Dincer (Ed.), Comprehensive Energy Systems (pp. 1107–1130). Elsevier. https://doi.org/https://doi.org/10.1016/B978-0-12-809597-3.00446-6

Crezee, T., Rabold, K., de Jong, L., Jaeger, M., & Netea-Maier, R. T. (2020). Metabolic programming of tumor associated macrophages in the context of cancer treatment. Annals of Translational Medicine, 8(16), 1028–1028. https://doi.org/10.21037/atm-20-1114

Dabare, P. R. L., Bachhuka, A., Quek, J. Y., Marsal, L. F., Hayball, J., & Vasilev, K. (2023). Nano-Roughness-Mediated Macrophage Polarization for Desired Host Immune Response. Small Science. https://doi.org/10.1002/smsc.202300080

Das, M., Zhu, C., & Kuchroo, V. K. (2017). Tim-3 and its role in regulating anti-tumor immunity. In Immunological Reviews (Vol. 276, Issue 1, pp. 97–111). Blackwell Publishing Ltd. https://doi.org/10.1111/imr.12520

Debela, D. T., Muzazu, S. G., Heraro, K. D., Ndalama, M. T., Mesele, B. W., Haile, D. C., Kitui, S. K., & Manyazewal, T. (2021). New approaches and procedures for cancer treatment: Current perspectives. SAGE Open Medicine, 9, 205031212110343. https://doi.org/10.1177/20503121211034366

Dhakshinamoorthy, A., Li, Z., & Garcia, H. (2018). Catalysis and photocatalysis by metal organic frameworks. In Chemical Society Reviews (Vol. 47, Issue 22, pp. 8134–8172). Royal Society of Chemistry. https://doi.org/10.1039/c8cs00256h

Ding, H., Zhang, Y., Mao, Y., Li, Y., Shen, Y., Sheng, J., & Gu, N. (2023). Modulation of macrophage polarization by iron-based nanoparticles. In Medical Review (Vol. 3, Issue 2, pp. 105–122). Walter de Gruyter GmbH. https://doi.org/10.1515/mr-2023-0002

Doncom, K. E. B., Blackman, L. D., Wright, D. B., Gibson, M. I., & O'Reilly, R. K. (2017). Dispersity effects in polymer self-assemblies: A matter of hierarchical control. In Chemical Society Reviews (Vol. 46, Issue 14, pp. 4119–4134). Royal Society of Chemistry. https://doi.org/10.1039/c6cs00818f

Duan, X., Chan, C., & Lin, W. (2019). Nanoparticle-Mediated Immunogenic Cell Death Enables and Potentiates Cancer Immunotherapy. In Angewandte Chemie - International Edition (Vol. 58, Issue 3, pp. 670–680). Wiley-VCH Verlag. https://doi.org/10.1002/anie.201804882

Dungan, L. S., Mcguinness, N. C., Boon, L., Lynch, M. A., & Mills, K. H. G. (2014). Innate IFN-γ promotes development of experimental autoimmune encephalomyelitis: A role for NK cells and M1 macrophages. European Journal of Immunology, 44(10), 2903–2917. https://doi.org/10.1002/eji.201444612

Engvall, E. (2010). The ELISA, enzyme-linked immunosorbent assay. In Clinical Chemistry (Vol. 56, Issue 2, pp. 319–320). https://doi.org/10.1373/clinchem.2009.127803

Ernst, L. M., Casals, E., Italiani, P., Boraschi, D., & Puntes, V. (2021). The interactions between nanoparticles and the innate immune system from a nanotechnologist perspective. In Nanomaterials (Vol. 11, Issue 11). MDPI. https://doi.org/10.3390/nano11112991

Falke, S., & Betzel, C. (2019). Dynamic Light Scattering (DLS) (pp. 173–193). https://doi.org/10.1007/978-3-030-28247-9_6

Ferlay, J., Colombet, M., Soerjomataram, I., Parkin, D. M., Piñeros, M., Znaor, A., & Bray, F. (2021). Cancer statistics for the year 2020: An overview. International Journal of Cancer, 149(4), 778–789. https://doi.org/10.1002/ijc.33588

Fernandes, P. D., Magalhães, F. D., Pereira, R. F., & Pinto, A. M. (2023). Metal-Organic Frameworks Applications in Synergistic Cancer Photo-Immunotherapy. In Polymers (Vol. 15, Issue 6). MDPI. https://doi.org/10.3390/polym15061490

Ferreira, L. M. B., Kiill, C. P., Pedreiro, L. N., Santos, A. M., & Gremião, M. P. D. (2018). Chapter 5 - Supramolecular design of hydrophobic and hydrophilic polymeric nanoparticles. In A. M. Grumezescu (Ed.), Design and Development of New Nanocarriers (pp. 181–221). William Andrew Publishing. https://doi.org/https://doi.org/10.1016/B978-0-12-813627-0.00005-3

Fisher, J., Zeitouni, N., Fan, W., & Samie, F. H. (2020). Immune checkpoint inhibitor therapy in solid organ transplant recipients: A patient-centered systematic review. In Journal of the American Academy of Dermatology (Vol. 82, Issue 6, pp. 1490–1500). Mosby Inc. https://doi.org/10.1016/j.jaad.2019.07.005

Forest, V., Leclerc, L., Hochepied, J. F., Trouvé, A., Sarry, G., & Pourchez, J. (2017). Impact of cerium oxide nanoparticles shape on their in vitro cellular toxicity. Toxicology in Vitro, 38, 136–141. https://doi.org/10.1016/j.tiv.2016.09.022

Forgan, R. S. (2020). Modulated self-assembly of metal-organic frameworks. In Chemical Science (Vol. 11, Issue 18, pp. 4546–4562). Royal Society of Chemistry. https://doi.org/10.1039/d0sc01356k

Franchi, L. P., Manshian, B. B., de Souza, T. A. J., Soenen, S. J., Matsubara, E. Y., Rosolen, J. M., & Takahashi, C. S. (2015). Cyto- and genotoxic effects of metallic nanoparticles in untransformed human fibroblast. Toxicology in Vitro, 29(7), 1319–1331. https://doi.org/10.1016/j.tiv.2015.05.010

Gao, P., Chen, Y., Pan, W., Li, N., Liu, Z., & Tang, B. (2021). Antitumor Agents Based on Metal–Organic Frameworks. Angewandte Chemie International Edition, 60(31), 16763–16776. https://doi.org/https://doi.org/10.1002/anie.202102574

Gao, X., Hai, X., Baigude, H., Guan, W., & Liu, Z. (2016). Fabrication of functional hollow microspheres constructed from MOF shells: Promising drug delivery systems with high

loading capacity and targeted transport. Scientific Reports, 6. https://doi.org/10.1038/srep37705

Gharagozloo, M., Majewski, S., & Foldvari, M. (2015). Therapeutic applications of nanomedicine in autoimmune diseases: From immunosuppression to tolerance induction. In Nanomedicine: Nanotechnology, Biology, and Medicine (Vol. 11, Issue 4, pp. 1003–1018). Elsevier Inc. https://doi.org/10.1016/j.nano.2014.12.003

González-García, L. E., Macgregor, M. N., Visalakshan, R. M., Lazarian, A., Cavallaro, A. A., Morsbach, S., Mierczynska-Vasilev, A., Mailänder, V., Landfester, K., & Vasilev, K. (2022). Nanoparticles Surface Chemistry Influence on Protein Corona Composition and Inflammatory Responses. Nanomaterials, 12(4). https://doi.org/10.3390/nano12040682

Guo, C., Zhang, Y., Guo, Y., Zhang, L., Zhang, Y., & Wang, J. (2018). A general and efficient approach for tuning the crystal morphology of classical MOFs. Chemical Communications, 54(3), 252–255. https://doi.org/10.1039/c7cc07698c

Guo, Q., Jin, Z., Yuan, Y., Liu, R., Xu, T., Wei, H., Xu, X., He, S., Chen, S., Shi, Z., Hou, W., & Hua, B. (2016). New Mechanisms of Tumor-Associated Macrophages on Promoting Tumor Progression: Recent Research Advances and Potential Targets for Tumor Immunotherapy. In Journal of Immunology Research (Vol. 2016). Hindawi Limited. https://doi.org/10.1155/2016/9720912

Guo, Z., Xing, R., Zhao, M., Li, Y., Lu, H., & Liu, Z. (2021). Controllable Engineering and Functionalizing of Nanoparticles for Targeting Specific Proteins towards Biomedical Applications. Advanced Science, 8(24). https://doi.org/10.1002/advs.202101713

Hadji, H., & Bouchemal, K. (2022). Effect of micro-and nanoparticle shape on biological processes. Journal of Controlled Release, 342. https://doi.org/10.1016/j.jconrel.2021.12.032ï

Hajipour, M. J., Saei, A. A., Walker, E. D., Conley, B., Omidi, Y., Lee, K. B., & Mahmoudi, M. (2021). Nanotechnology for Targeted Detection and Removal of Bacteria: Opportunities and Challenges. In Advanced Science (Vol. 8, Issue 21). John Wiley and Sons Inc. https://doi.org/10.1002/advs.202100556

Hao, F., Yan, Z. Y., & Yan, X. P. (2022). Recent Advances in Research on the Effect of Physicochemical Properties on the Cytotoxicity of Metal–Organic Frameworks. In Small Science (Vol. 2, Issue 9). John Wiley and Sons Inc. https://doi.org/10.1002/smsc.202200044

Jeevanandam, J., Chan, Y. S., Danquah, M. K., & Law, M. C. (2020). Cytotoxicity Analysis of Morphologically Different Sol-Gel-Synthesized MgO Nanoparticles and Their In Vitro Insulin Resistance Reversal Ability in Adipose cells. Applied Biochemistry and Biotechnology, 190(4), 1385–1410. https://doi.org/10.1007/s12010-019-03166-z

Jeong, S. K., Kim, J. S., Lee, C. G., Park, Y. S., Kim, S. D., Yoon, S. O., Han, D. H., Lee, K. Y., Jeong, M. H., & Jo, W. S. (2017). Tumor associated macrophages provide the survival resistance of tumor cells to hypoxic microenvironmental condition through IL-6 receptor-mediated signals. Immunobiology, 222(1), 55–65. https://doi.org/10.1016/j.imbio.2015.11.010

Ji, Z., Wang, X., Zhang, H., Lin, S., Meng, H., Sun, B., George, S., Xia, T., Nel, A. E., & Zink, J. I. (2012). Designed synthesis of CeO 2 nanorods and nanowires for studying toxicological effects of high aspect ratio nanomaterials. ACS Nano, 6(6), 5366–5380. https://doi.org/10.1021/nn3012114

Joudeh, N., & Linke, D. (2022). Nanoparticle classification, physicochemical properties, characterization, and applications: a comprehensive review for biologists. In Journal of Nanobiotechnology (Vol. 20, Issue 1). BioMed Central Ltd. https://doi.org/10.1186/s12951-022-01477-8

Kakizawa, Y., Lee, J. S., Bell, B., & Fahmy, T. M. (2017). Precise manipulation of biophysical particle parameters enables control of proinflammatory cytokine production in presence of TLR 3 and 4 ligands. Acta Biomaterialia, 57, 136–145. https://doi.org/10.1016/j.actbio.2017.01.025

Karimi, M., Zare, H., Bakhshian Nik, A., Yazdani, N., Hamrang, M., Mohamed, E., Zangabad, P. S., Basri, S. M. M., Bakhtiari, L., & Hamblin, M. R. (2016). Nanotechnology in diagnosis and treatment of coronary artery disease. In Nanomedicine (Vol. 11, Issue 5, pp. 513–530). Future Medicine Ltd. https://doi.org/10.2217/nnm.16.3

Khodabandehloo, H., Zahednasab, H., & Hafez, A. A. (2016). Nanocarriers usage for drug delivery in cancer therapy. International Journal of Cancer Management, 9(2). https://doi.org/10.17795/ijcp-3966

Kim, D., Jeong, Y. Y., & Jon, S. (2010). A drug-loaded aptamer - Gold nanoparticle bioconjugate for combined ct imaging and therapy of prostate cancer. ACS Nano, 4(7), 3689–3696. https://doi.org/10.1021/nn901877h

Kratz, J. D., Chaddha, A., Bhattacharjee, S., & Goonewardena, S. N. (2016). Atherosclerosis and Nanotechnology: Diagnostic and Therapeutic Applications. Cardiovascular Drugs and Therapy, 30(1), 33–39. https://doi.org/10.1007/s10557-016-6649-2

Kreno, L. E., Leong, K., Farha, O. K., Allendorf, M., Van Duyne, R. P., & Hupp, J. T. (2012). Metal-organic framework materials as chemical sensors. In Chemical Reviews (Vol. 112, Issue 2, pp. 1105–1125). https://doi.org/10.1021/cr200324t

Lan, G., Ni, K., Xu, Z., Veroneau, S. S., Song, Y., & Lin, W. (2018). Nanoscale Metal-Organic Framework Overcomes Hypoxia for Photodynamic Therapy Primed Cancer Immunotherapy. Journal of the American Chemical Society, 140(17), 5670–5673. https://doi.org/10.1021/jacs.8b01072

Lavine, K. J., Pinto, A. R., Epelman, S., Kopecky, B. J., Clemente-Casares, X., Godwin, J., Rosenthal, N., & Kovacic, J. C. (2018). The Macrophage in Cardiac Homeostasis and Disease: JACC Macrophage in CVD Series (Part 4). In Journal of the American College of Cardiology (Vol. 72, Issue 18, pp. 2213–2230). Elsevier USA. https://doi.org/10.1016/j.jacc.2018.08.2149

Lebre, F., Sridharan, R., Sawkins, M. J., Kelly, D. J., O'Brien, F. J., & Lavelle, E. C. (2017). The shape and size of hydroxyapatite particles dictate inflammatory responses following implantation. Scientific Reports, 7(1). https://doi.org/10.1038/s41598-017-03086-0

Lee, J. Y., & Choi, J. H. (2022). Copper-based metal-organic framework for highly efficient adsorption of lead ions from aqueous solution. Materials Research Express, 9(9). https://doi.org/10.1088/2053-1591/ac93ea

Lee, S., Choi, J., Shin, S., Im, Y. M., Song, J., Kang, S. S., Nam, T. H., Webster, T. J., Kim, S. H., & Khang, D. (2011). Analysis on migration and activation of live macrophages on transparent flat and nanostructured titanium. Acta Biomaterialia, 7(5), 2337–2344. https://doi.org/10.1016/j.actbio.2011.01.006

Lee Ventola, C. (2017). Cancer Immunotherapy, Part 3: Challenges and Future Trends (Vol. 42, Issue 8).

Level of human development (HDI) mort prev. (2014). www.cruk.org/cancerstats

Li, M., Zhou, H., Zhang, L., Han, J., Wang, G., Fan, F., Wang, T., Zhang, X., & Fu, Y. (2023). Size and morphology control of two-dimensional metal-organic frameworks through coordination modulation. Microporous and Mesoporous Materials, 348. https://doi.org/10.1016/j.micromeso.2022.112379

Li, P., Hao, Z., Wu, J., Ma, C., Xu, Y., Li, J., Lan, R., Zhu, B., Ren, P., Fan, D., & Sun, S. (2021). Comparative Proteomic Analysis of Polarized Human THP-1 and Mouse RAW264.7 Macrophages. Frontiers in Immunology, 12. https://doi.org/10.3389/fimmu.2021.700009

Li, Q., Liu, Y., Zhang, Y., & Jiang, W. (2022). Immunogenicity-boosted cancer immunotherapy based on nanoscale metal-organic frameworks. In Journal of Controlled Release (Vol. 347, pp. 183–198). Elsevier B.V. https://doi.org/10.1016/j.jconrel.2022.05.003

Li, S., Feng, X., Wang, J., He, L., Wang, C., Ding, J., & Chen, X. (2018). Polymer nanoparticles as adjuvants in cancer immunotherapy. In Nano Research (Vol. 11, Issue 11, pp. 5769–5786). Tsinghua University Press. https://doi.org/10.1007/s12274-018-2124-7

Li, Z., Sun, L., Zhang, Y., Dove, A. P., O'Reilly, R. K., & Chen, G. (2016). Shape Effect of Glyco-Nanoparticles on Macrophage Cellular Uptake and Immune Response. ACS Macro Letters, 5(9), 1059–1064. https://doi.org/10.1021/acsmacrolett.6b00419

Liao, X., Wang, F., Wang, F., Cai, Y., Yao, Y., Teng, B. T., Hao, Q., & Shuxiang, L. (2019). Synthesis of (100) surface oriented MIL-88A-Fe with rod-like structure and its enhanced fenton-like performance for phenol removal. Applied Catalysis B: Environmental, 259. https://doi.org/10.1016/j.apcatb.2019.118064

Liu, B., Vellingiri, K., Jo, S.-H., Kumar, P., Ok, Y. S., & Kim, K.-H. (2018). Recent advances in controlled modification of the size and morphology of metal-organic frameworks. Nano Research, 11(9), 4441–4467. https://doi.org/10.1007/s12274-018-2039-3

Liu, J., Geng, X., Hou, J., & Wu, G. (2021). New insights into M1/M2 macrophages: key modulators in cancer progression. In Cancer Cell International (Vol. 21, Issue 1). BioMed Central Ltd. https://doi.org/10.1186/s12935-021-02089-2

Liu, L., Sha, R., Yang, L., Zhao, X., Zhu, Y., Gao, J., Zhang, Y., & Wen, L. P. (2018). Impact of Morphology on Iron Oxide Nanoparticles-Induced Inflammasome Activation in Macrophages. ACS Applied Materials and Interfaces, 10(48), 41197–41206. https://doi.org/10.1021/acsami.8b17474

Liu, Q., Wu, B., Li, M., Huang, Y., & Li, L. (2022). Heterostructures Made of Upconversion Nanoparticles and Metal–Organic Frameworks for Biomedical Applications. In Advanced Science (Vol. 9, Issue 3). John Wiley and Sons Inc. https://doi.org/10.1002/advs.202103911

Liu, X., Shan, K., Shao, X., Shi, X., He, Y., Liu, Z., Jacob, J. A., & Deng, L. (2021). Nanotoxic effects of silver nanoparticles on normal HEK-293 cells in comparison to cancerous hela cell line. International Journal of Nanomedicine, 16, 753–761. https://doi.org/10.2147/IJN.S289008

López-García, J., Lehocký, M., Humpolíček, P., & Sáha, P. (2014). HaCaT Keratinocytes Response on Antimicrobial Atelocollagen Substrates: Extent of Cytotoxicity, Cell Viability and Proliferation. Journal of Functional Biomaterials, 5(2), 43–57. https://doi.org/10.3390/jfb5020043

Lu, Y., Rong, J., Lai, Y., Tao, L., Yuan, X., & Shu, X. (2020). The Degree of Helicobacter pylori Infection Affects the State of Macrophage Polarization through Crosstalk between ROS and HIF-1 α. Oxidative Medicine and Cellular Longevity, 2020. https://doi.org/10.1155/2020/5281795

Łuczak, J., Kroczewska, M., Baluk, M., Sowik, J., Mazierski, P., & Zaleska-Medynska, A. (2023). Morphology control through the synthesis of metal-organic frameworks. Advances in Colloid and Interface Science, 314, 102864. https://doi.org/10.1016/j.cis.2023.102864

Luo, G., Jiang, Y., Xie, C., & Lu, X. (2021). Metal-organic framework-based biomaterials for biomedical applications. Biosurface and Biotribology, 7(3), 99–112. https://doi.org/10.1049/bsb2.12012

Lv, X. L., Yuan, S., Xie, L. H., Darke, H. F., Chen, Y., He, T., Dong, C., Wang, B., Zhang, Y. Z., Li, J. R., & Zhou, H. C. (2019). Ligand Rigidification for Enhancing the Stability of Metal-Organic Frameworks. Journal of the American Chemical Society, 141(26), 10283–10293. https://doi.org/10.1021/jacs.9b02947

Ma, J., Liu, R., Wang, X., Liu, Q., Chen, Y., Valle, R. P., Zuo, Y. Y., Xia, T., & Liu, S. (2015). Crucial Role of Lateral Size for Graphene Oxide in Activating Macrophages and Stimulating Pro-inflammatory Responses in Cells and Animals. ACS Nano, 9(10), 10498–10515. https://doi.org/10.1021/acsnano.5b04751

Mahoney, K. M., Rennert, P. D., & Freeman, G. J. (2015). Combination cancer immunotherapy and new immunomodulatory targets. Nature Reviews Drug Discovery, 14(8), 561–584. https://doi.org/10.1038/nrd4591

Malloy, A., & Carr, B. (2006). NanoParticle Tracking Analysis – The HaloTM System. Particle & Particle Systems Characterization, 23(2), 197–204. https://doi.org/https://doi.org/10.1002/ppsc.200601031

Marshall, C. R., Staudhammer, S. A., & Brozek, C. K. (2019). Size control over metal-organic framework porous nanocrystals. In Chemical Science (Vol. 10, Issue 41, pp. 9396–9408). Royal Society of Chemistry. https://doi.org/10.1039/c9sc03802g

Martinez, F. O., & Gordon, S. (2014). The M1 and M2 paradigm of macrophage activation: Time for reassessment. F1000Prime Reports, 6. https://doi.org/10.12703/P6-13

Mccarthy, D. J., & Smyth, G. K. (2009). Testing significance relative to a fold-change threshold is a TREAT. Bioinformatics, 25(6), 765–771. https://doi.org/10.1093/bioinformatics/btp053

McKinnon, K. M. (2018). Flow cytometry: An overview. Current Protocols in Immunology, 2018, 5.1.1-5.1.11. https://doi.org/10.1002/cpim.40

Miao, X., Leng, X., & Zhang, Q. (2017). The current state of nanoparticle-induced macrophage polarization and reprogramming research. In International Journal of Molecular Sciences (Vol. 18, Issue 2). MDPI AG. https://doi.org/10.3390/ijms18020336

Mirza, A. Z., & Siddiqui, F. A. (2014). Nanomedicine and drug delivery: a mini review. International Nano Letters, 4(1). https://doi.org/10.1007/s40089-014-0094-7

Monakhova, P. A., Shalaev, P. V., & Gorev, I. N. (2023). Rapid Characterization of Synthesized Nanoparticles' Liquid Dispersions Using Nanoparticle Tracking Analysis. 65. https://doi.org/10.3390/iocn2023-14528

Monnier, M., Paolini, L., Vinatier, E., Mantovani, A., Delneste, Y., & Jeannin, P. (2022). Antitumor strategies targeting macrophages: the importance of considering the differences in differentiation/polarization processes between human and mouse macrophages. In Journal for ImmunoTherapy of Cancer (Vol. 10, Issue 10). BMJ Publishing Group. https://doi.org/10.1136/jitc-2022-005560

Mora-Raimundo, P., Manzano, M., & Vallet-Regí, M. (2017). Nanoparticles for the treatment of osteoporosis. AIMS Bioengineering, 4(2), 259–274. https://doi.org/10.3934/bioeng.2017.2.259

Mouw, J. K., Ou, G., & Weaver, V. M. (2014). Extracellular matrix assembly: a multiscale deconstruction. Nature Reviews Molecular Cell Biology, 15(12), 771–785. https://doi.org/10.1038/nrm3902

Murray, P. J., Allen, J. E., Biswas, S. K., Fisher, E. A., Gilroy, D. W., Goerdt, S., Gordon, S., Hamilton, J. A., Ivashkiv, L. B., Lawrence, T., Locati, M., Mantovani, A., Martinez, F. O., Mege, J. L., Mosser, D. M., Natoli, G., Saeij, J. P., Schultze, J. L., Shirey, K. A., … Wynn, T. A. (2014). Macrophage Activation and Polarization: Nomenclature and Experimental Guidelines. In Immunity (Vol. 41, Issue 1, pp. 14–20). Cell Press. https://doi.org/10.1016/j.immuni.2014.06.008

Nascimento, C. S., Alves, É. A. R., De Melo, C. P., Corrêa-Oliveira, R., & Calzavara-Silva, C. E. (2021). Immunotherapy for cancer: Effects of iron oxide nanoparticles on polarization of tumor-associated macrophages. In Nanomedicine (Vol. 16, Issue 29, pp. 2633–2650). Future Medicine Ltd. https://doi.org/10.2217/nnm-2021-0255

Neacsu, P., Mazare, A., Cimpean, A., Park, J., Costache, M., Schmuki, P., & Demetrescu, I. (2014). Reduced inflammatory activity of RAW 264.7 macrophages on titania nanotube modified Ti surface. International Journal of Biochemistry and Cell Biology, 55, 187–195. https://doi.org/10.1016/j.biocel.2014.09.006

Nel, A. (2023). Carbon nanotube pathogenicity conforms to a unified theory for mesothelioma causation by elongate materials and fibers. Environmental Research, 230. https://doi.org/10.1016/j.envres.2022.114580

Ni, K., Luo, T., Nash, G. T., & Lin, W. (2020). Nanoscale metal-organic frameworks for cancer immunotherapy. Accounts of Chemical Research, 53(9), 1739–1748. https://doi.org/10.1021/acs.accounts.0c00313

Nishanth, R. P., Jyotsna, R. G., Schlager, J. J., Hussain, S. M., & Reddanna, P. (2011). Inflammatory responses of RAW 264.7 macrophages upon exposure to nanoparticles: Role of ROS-NFκB signaling pathway. Nanotoxicology, 5(4), 502–516. https://doi.org/10.3109/17435390.2010.541604

Oh, W.-K., Kim, S., Yoon, H., & Jang, J. (2010). Shape-Dependent Cytotoxicity and Proinflammatory Response of Poly(3,4-ethylenedioxythiophene) Nanomaterials. Small, 6(7), 872–879. https://doi.org/https://doi.org/10.1002/smll.200902074

Orecchioni, M., Ghosheh, Y., Pramod, A. B., & Ley, K. (2019). Macrophage polarization: Different gene signatures in M1(Lps+) vs. Classically and M2(LPS-) vs. Alternatively activated macrophages. In Frontiers in Immunology (Vol. 10, Issue MAY). Frontiers Media S.A. https://doi.org/10.3389/fimmu.2019.01084

Pal, R., Chakraborty, B., Nath, A., Singh, L. M., Ali, M., Rahman, D. S., Ghosh, S. K., Basu, A., Bhattacharya, S., Baral, R., & Sengupta, M. (2016). Noble metal nanoparticle-induced oxidative stress modulates tumor associated macrophages (TAMs) from an M2 to M1 phenotype: An in vitro approach. International Immunopharmacology, 38, 332–341. https://doi.org/10.1016/j.intimp.2016.06.006

Palomäki, J., Välimäki, E., Sund, J., Vippola, M., Clausen, P. A., Jensen, K. A., Savolainen, K., Matikainen, S., & Alenius, H. (2011). Long, needle-like carbon nanotubes and asbestos activate the NLRP3 inflammasome through a similar mechanism. ACS Nano, 5(9), 6861–6870. https://doi.org/10.1021/nn200595c

Panariti, A., Miserocchi, G., & Rivolta, I. (2012). The effect of nanoparticle uptake on cellular behavior: Disrupting or enabling functions? In Nanotechnology, Science and Applications (Vol. 5, Issue 1, pp. 87–100). https://doi.org/10.2147/NSA.S25515

Park, J. E., Dutta, B., Tse, S. W., Gupta, N., Tan, C. F., Low, J. K., Yeoh, K. W., Kon, O. L., Tam, J. P., & Sze, S. K. (2019). Hypoxia-induced tumor exosomes promote M2-like macrophage polarization of infiltrating myeloid cells and microRNA-mediated metabolic shift. Oncogene, 38(26), 5158–5173. https://doi.org/10.1038/s41388-019-0782-x

Peng, S., Xiao, F., Chen, M., & Gao, H. (2022). Tumor-Microenvironment-Responsive Nanomedicine for Enhanced Cancer Immunotherapy. In Advanced Science (Vol. 9, Issue 1). John Wiley and Sons Inc. https://doi.org/10.1002/advs.202103836

Pillai, G., & Ceballos-Coronel, M. L. (2013). Science and technology of the emerging nanomedicines in cancer therapy: A primer for physicians and pharmacists. SAGE Open Medicine, 1, 205031211351375. https://doi.org/10.1177/2050312113513759

Prietl, B., Meindl, C., Roblegg, E., Pieber, T. R., Lanzer, G., & Fröhlich, E. (2014). Nano-sized and micro-sized polystyrene particles affect phagocyte function. Cell Biology and Toxicology, 30(1), 1–16. https://doi.org/10.1007/s10565-013-9265-y

Pujari-Palmer, S., Chen, S., Rubino, S., Weng, H., Xia, W., Engqvist, H., Tang, L., & Ott, M. K. (2016). In vivo and in vitro evaluation of hydroxyapatite nanoparticle morphology on

the acute inflammatory response. Biomaterials, 90, 1–11. https://doi.org/10.1016/j.biomaterials.2016.02.039

Qu, Y., Chu, B., Wei, X., Chen, Y., Yang, Y., Hu, D., Huang, J., Wang, F., Chen, M., Zheng, Y., & Qian, Z. (2022). Cancer-Cell-Biomimetic Nanoparticles for Targeted Therapy of Multiple Myeloma Based on Bone Marrow Homing. Advanced Materials, 34(46), 2107883. https://doi.org/https://doi.org/10.1002/adma.202107883

Rabolli, V., Lison, D., & Huaux, F. (2016). The complex cascade of cellular events governing inflammasome activation and IL- 1β processing in response to inhaled particles. In Particle and Fibre Toxicology (Vol. 13, Issue 1). BioMed Central Ltd. https://doi.org/10.1186/S12989-016-0150-8

Rakshe, V. P. (2018). Shape-specific Effects of Cerium Oxide Nanoparticles (CNPs) on Macrophage Polarization.

Rao, X., Huang, X., Zhou, Z., & Lin, X. (2013). An improvement of the 2ˆ(-delta delta CT) method for quantitative real-time polymerase chain reaction data analysis.

Raval, N., Maheshwari, R., Kalyane, D., Youngren-Ortiz, S. R., Chougule, M. B., & Tekade, R. K. (2019). Chapter 10 - Importance of Physicochemical Characterization of Nanoparticles in Pharmaceutical Product Development. In R. K. Tekade (Ed.), Basic Fundamentals of Drug Delivery (pp. 369–400). Academic Press. https://doi.org/https://doi.org/10.1016/B978-0-12-817909-3.00010-8

Rodell, C. B., Arlauckas, S. P., Cuccarese, M. F., Garris, C. S., Li, R., Ahmed, M. S., Kohler, R. H., Pittet, M. J., & Weissleder, R. (2018). TLR7/8-agonist-loaded nanoparticles promote the polarization of tumour-associated macrophages to enhance cancer immunotherapy. Nature Biomedical Engineering, 2(8), 578–588. https://doi.org/10.1038/s41551-018-0236-8

Saas, P., Chagué, C., Maraux, M., & Cherrier, T. (2020). Toward the Characterization of Human Pro-Resolving Macrophages? Frontiers in Immunology, 11. https://doi.org/10.3389/fimmu.2020.593300

Sadeghi Rad, H., Monkman, J., Warkiani, M. E., Ladwa, R., O'Byrne, K., Rezaei, N., & Kulasinghe, A. (2021). Understanding the tumor microenvironment for effective immunotherapy. In Medicinal Research Reviews (Vol. 41, Issue 3, pp. 1474–1498). John Wiley and Sons Inc. https://doi.org/10.1002/med.21765

Schirinzi, G. F., Pérez-Pomeda, I., Sanchís, J., Rossini, C., Farré, M., & Barceló, D. (2017). Cytotoxic effects of commonly used nanomaterials and microplastics on cerebral and epithelial human cells. Environmental Research, 159, 579–587. https://doi.org/10.1016/j.envres.2017.08.043

Sercombe, L., Veerati, T., Moheimani, F., Wu, S. Y., Sood, A. K., & Hua, S. (2015). Advances and challenges of liposome assisted drug delivery. In Frontiers in Pharmacology (Vol. 6, Issue DEC). Frontiers Media S.A. https://doi.org/10.3389/fphar.2015.00286

Shah, K., & Maghsoudlou, P. (2016). Enzyme-linked immunosorbent assay (ELISA): the basics. British Journal of Hospital Medicine, 77(7), C98–C101. https://doi.org/10.12968/hmed.2016.77.7.C98

Sheldrake, A. R. (2022). Cellular senescence, rejuvenation and potential immortality. In Proceedings of the Royal Society B: Biological Sciences (Vol. 289, Issue 1970). Royal Society Publishing. https://doi.org/10.1098/rspb.2021.2434

Sigola, L. B., Fuentes, A. L., Millis, L. M., Vapenik, J., & Murira, A. (2016). Effects of Toll-like receptor ligands on RAW 264.7 macrophage morphology and zymosan phagocytosis. Tissue and Cell, 48(4), 389–396. https://doi.org/10.1016/j.tice.2016.04.002

Silva Adaya, D., Aguirre-Cruz, L., Guevara, J., & Ortiz-Islas, E. (2017). Nanobiomaterials' applications in neurodegenerative diseases. In Journal of Biomaterials Applications (Vol. 31, Issue 7, pp. 953–984). SAGE Publications Ltd. https://doi.org/10.1177/0885328216659032

Sim, S., & Wong, N. K. (2021). Nanotechnology and its use in imaging and drug delivery (Review). Biomedical Reports, 14(5). https://doi.org/10.3892/br.2021.1418

Smirnova, T., Bonapace, L., Macdonald, G., Kondo, S., Wyckoff, J., Ebersbach, H., Fayard, B., Doelemeyer, A., Coissieux, M.-M., Heideman, M. R., Bentires-Alj, M., & Hynes, N. E. (2016). Serpin E2 promotes breast cancer metastasis by remodeling the tumor matrix and polarizing tumor associated macrophages. In Oncotarget (Vol. 7, Issue 50). www.impactjournals.com/oncotarget/

Sun, W., Zhai, X., & Zhao, L. (2016). Synthesis of ZIF-8 and ZIF-67 nanocrystals with well-controllable size distribution through reverse microemulsions. Chemical Engineering Journal, 289, 59–64. https://doi.org/10.1016/j.cej.2015.12.076

Sun, Y., Zheng, L., Yang, Y., Qian, X., Fu, T., Li, X., Yang, Z., Yan, H., Cui, C., & Tan, W. (2020). Metal–Organic Framework Nanocarriers for Drug Delivery in Biomedical Applications. In Nano-Micro Letters (Vol. 12, Issue 1). Springer. https://doi.org/10.1007/s40820-020-00423-3

Sussman, E. M., Halpin, M. C., Muster, J., Moon, R. T., & Ratner, B. D. (2014). Porous Implants Modulate Healing and Induce Shifts in Local Macrophage Polarization in the Foreign Body Reaction. Annals of Biomedical Engineering, 42(7), 1508–1516. https://doi.org/10.1007/s10439-013-0933-0

Sylvestre, M., Crane, C. A., & Pun, S. H. (2020). Progress on Modulating Tumor-Associated Macrophages with Biomaterials. In Advanced Materials (Vol. 32, Issue 13). Wiley-VCH Verlag. https://doi.org/10.1002/adma.201902007

Synthesis, Characterization and Comparative Study of Copper and Zinc Metal Organic Frameworks. (2013). Chemical Science Transactions, 2(4). https://doi.org/10.7598/cst2013.520

Taciak, B., Białasek, M., Braniewska, A., Sas, Z., Sawicka, P., Kiraga, Ł., Rygiel, T., & Król, M. (2018). Evaluation of phenotypic and functional stability of RAW 264.7 cell line through serial passages. PLoS ONE, 13(6). https://doi.org/10.1371/journal.pone.0198943

Taira, M., Shimoyama, Y., Kagiya, T., Sasaki, M., Nezu, T., Harada, H., & Kimura, S. (2011). Proteome analyses of human macrophages exposed to low cytotoxic IC90 copper (2+) ions. Dental Materials Journal, 30(3), 293–299. https://doi.org/10.4012/dmj.2010-088

Tekie, F. S. M., Hajiramezanali, M., Geramifar, P., Raoufi, M., Dinarvand, R., Soleimani, M., & Atyabi, F. (2020). Controlling evolution of protein corona: a prosperous approach to improve chitosan-based nanoparticle biodistribution and half-life. Scientific Reports, 10(1), 9664. https://doi.org/10.1038/s41598-020-66572-y

Thakur, N., Thakur, S., Chatterjee, S., Das, J., & Sil, P. C. (2020). Nanoparticles as Smart Carriers for Enhanced Cancer Immunotherapy. In Frontiers in Chemistry (Vol. 8). Frontiers Media S.A. https://doi.org/10.3389/fchem.2020.597806

Timosenko, E., Hadjinicolaou, A. V., & Cerundolo, V. (2017). Modulation of cancer-specific immune responses by amino acid degrading enzymes. In Immunotherapy (Vol. 9, Issue 1, pp. 83–97). Future Medicine Ltd. https://doi.org/10.2217/imt-2016-0118

Tran, V. A., Thuan Le, V., Doan, V. D., & Vo, G. N. L. (2023). Utilization of Functionalized Metal–Organic Framework Nanoparticle as Targeted Drug Delivery System for Cancer Therapy. In Pharmaceutics (Vol. 15, Issue 3). MDPI. https://doi.org/10.3390/pharmaceutics15030931

Tsuruoka, T., Furukawa, S., Takashima, Y., Yoshida, K., Isoda, S., & Kitagawa, S. (2009). Nanoporous Nanorods Fabricated by Coordination Modulation and Oriented Attachment Growth. Angewandte Chemie International Edition, 48(26), 4739–4743. https://doi.org/https://doi.org/10.1002/anie.200901177

Umemura, A., Diring, S., Furukawa, S., Uehara, H., Tsuruoka, T., & Kitagawa, S. (2011). Morphology design of porous coordination polymer crystals by coordination modulation. Journal of the American Chemical Society, 133(39), 15506–15513. https://doi.org/10.1021/ja204233q

Vaddepally, R. K., Kharel, P., Pandey, R., Garje, R., & Chandra, A. B. (2020). Review of indications of FDA-approved immune checkpoint inhibitors per NCCN guidelines with the level of evidence. In Cancers (Vol. 12, Issue 3). MDPI AG. https://doi.org/10.3390/cancers12030738

Venna, S. R., Lartey, M., Li, T., Spore, A., Kumar, S., Nulwala, H. B., Luebke, D. R., Rosi, N. L., & Albenze, E. (2015). Fabrication of MMMs with improved gas separation properties using externally-functionalized MOF particles. Journal of Materials Chemistry A, 3(9), 5014–5022. https://doi.org/10.1039/c4ta05225k

Vijayan, V., Pradhan, P., Braud, L., Fuchs, H. R., Gueler, F., Motterlini, R., Foresti, R., & Immenschuh, S. (2019). Human and murine macrophages exhibit differential metabolic responses to lipopolysaccharide - A divergent role for glycolysis. Redox Biology, 22. https://doi.org/10.1016/j.redox.2019.101147

Wang, F., Guo, H., Chai, Y., Li, Y., & Liu, C. (2013). The controlled regulation of morphology and size of HKUST-1 by “coordination modulation method.” Microporous and Mesoporous Materials, 173, 181–188. https://doi.org/10.1016/j.micromeso.2013.02.023

Wang, H., Li, S., Yang, Y., Zhang, L., Zhang, Y., & Wei, T. (2022). Perspectives of metal-organic framework nanosystem to overcome tumor drug resistance. In Cancer Drug Resistance (Vol. 5, Issue 4, pp. 954–970). OAE Publishing Inc. https://doi.org/10.20517/cdr.2022.76

Wang, S., McGuirk, C. M., d'Aquino, A., Mason, J. A., & Mirkin, C. A. (2018). Metal–Organic Framework Nanoparticles. In Advanced Materials (Vol. 30, Issue 37). Wiley-VCH Verlag. https://doi.org/10.1002/adma.201800202

Wang, Y., Shang, W., Niu, M., Tian, J., & Xu, K. (2019). Hypoxia-active nanoparticles used in tumor theranostic. In International Journal of Nanomedicine (Vol. 14, pp. 3705–3722). Dove Medical Press Ltd. https://doi.org/10.2147/IJN.S196959

Wang, Z., Qiao, R., Tang, N., Lu, Z., Wang, H., Zhang, Z., Xue, X., Huang, Z., Zhang, S., Zhang, G., & Li, Y. (2017). Active targeting theranostic iron oxide nanoparticles for MRI and magnetic resonance-guided focused ultrasound ablation of lung cancer. Biomaterials, 127, 25–35. https://doi.org/10.1016/j.biomaterials.2017.02.037

Williams, C. B., Yeh, E. S., & Soloff, A. C. (2016). Tumor-associated macrophages: Unwitting accomplices in breast cancer malignancy. In npj Breast Cancer (Vol. 2, Issue 1). Nature Publishing Group. https://doi.org/10.1038/npjbcancer.2015.25

Winey, M., Meehl, J. B., O'Toole, E. T., & Giddings, T. H. (2014). Conventional transmission electron microscopy. In Molecular Biology of the Cell (Vol. 25, Issue 3, pp. 319–323). https://doi.org/10.1091/mbc.E12-12-0863

Woźniak, A., Malankowska, A., Nowaczyk, G., Grześkowiak, B. F., Tuśnio, K., Słomski, R., Zaleska-Medynska, A., & Jurga, S. (2017). Size and shape-dependent cytotoxicity profile of gold nanoparticles for biomedical applications. Journal of Materials Science: Materials in Medicine, 28(6). https://doi.org/10.1007/s10856-017-5902-y

Wu, B., Wu, X., Liu, S., Wang, Z., & Chen, L. (2019). Size-dependent effects of polystyrene microplastics on cytotoxicity and efflux pump inhibition in human Caco-2 cells. Chemosphere, 221, 333–341. https://doi.org/10.1016/j.chemosphere.2019.01.056

Wu, M.-X., & Yang, Y.-W. (2017). Metal–Organic Framework (MOF)-Based Drug/Cargo Delivery and Cancer Therapy. Advanced Materials, 29(23), 1606134. https://doi.org/https://doi.org/10.1002/adma.201606134

Wu, S.-Y., Wu, F.-G., & Chen, X. (2022). Antibody-Incorporated Nanomedicines for Cancer Therapy. Advanced Materials, 34(24), 2109210. https://doi.org/https://doi.org/10.1002/adma.202109210

Xin, C., Zhan, H., Huang, X., Li, H., Zhao, N., Xiao, F., Wei, W., & Sun, Y. (2015). Effect of various alkaline agents on the size and morphology of nano-sized HKUST-1 for CO2 adsorption. RSC Advances, 5(35), 27901–27911. https://doi.org/10.1039/c5ra03986j

Yang, J., & Yang, Y.-W. (2020). Metal–Organic Frameworks for Biomedical Applications. Small, 16(10), 1906846. https://doi.org/https://doi.org/10.1002/smll.201906846

Yang, S., Zhang, Y., Lu, S., Yang, L., Yu, S., & Yang, H. (2021). CaCO3-Encapsulated Au Nanoparticles Modulate Macrophages toward M1-like Phenotype. ACS Applied Bio Materials, 4(4), 3214–3223. https://doi.org/10.1021/acsabm.0c01608

Yang, Y., Song, Z., Wu, W., Xu, A., Lv, S., & Ji, S. (2020). ZnO Quantum Dots Induced Oxidative Stress and Apoptosis in HeLa and HEK-293T Cell Lines. Frontiers in Pharmacology, 11. https://doi.org/10.3389/fphar.2020.00131

Yeh, Y. C., Huang, T. H., Yang, S. C., Chen, C. C., & Fang, J. Y. (2020). Nano-Based Drug Delivery or Targeting to Eradicate Bacteria for Infection Mitigation: A Review of Recent Advances. In Frontiers in Chemistry (Vol. 8). Frontiers Media S.A. https://doi.org/10.3389/fchem.2020.00286

Yen, H.-J., Hsu, S., & Tsai, C.-L. (2009). Cytotoxicity and Immunological Response of Gold and Silver Nanoparticles of Different Sizes. Small, 5(13), 1553–1561. https://doi.org/https://doi.org/10.1002/smll.200900126

Yoshizaki, Y., Yuba, E., Sakaguchi, N., Koiwai, K., Harada, A., & Kono, K. (2017). pH-sensitive polymer-modified liposome-based immunity-inducing system: Effects of inclusion of cationic lipid and CpG-DNA. Biomaterials, 141, 272–283. https://doi.org/10.1016/j.biomaterials.2017.07.001

Yunna, C., Mengru, H., Lei, W., & Weidong, C. (2020). Macrophage M1/M2 polarization. In European Journal of Pharmacology (Vol. 877). Elsevier B.V. https://doi.org/10.1016/j.ejphar.2020.173090

Yusuff, A. S., Popoola, L. T., & Babatunde, E. O. (2019). Adsorption of cadmium ion from aqueous solutions by copper-based metal organic framework: equilibrium modeling and kinetic studies. Applied Water Science, 9(4). https://doi.org/10.1007/s13201-019-0991-z

Zanganeh, S., Hutter, G., Spitler, R., Lenkov, O., Mahmoudi, M., Shaw, A., Pajarinen, J. S., Nejadnik, H., Goodman, S., Moseley, M., Coussens, L. M., & Daldrup-Link, H. E. (2016). Iron oxide nanoparticles inhibit tumour growth by inducing pro-inflammatory macrophage polarization in tumour tissues. Nature Nanotechnology, 11(11), 986–994. https://doi.org/10.1038/nnano.2016.168

Zaorsky, N. G., Churilla, T. M., Egleston, B. L., Fisher, S. G., Ridge, J. A., Horwitz, E. M., & Meyer, J. E. (2017). Causes of death among cancer patients. Annals of Oncology, 28(2), 400–407. https://doi.org/10.1093/annonc/mdw604

Zeng, Q., Li, H., Jiang, H., Yu, J., Wang, Y., Ke, H., Gong, T., Zhang, Z., & Sun, X. (2017). Tailoring polymeric hybrid micelles with lymph node targeting ability to improve the potency of cancer vaccines. Biomaterials, 122, 105–113. https://doi.org/10.1016/j.biomaterials.2017.01.010

Zhang, B., Sai Lung, P., Zhao, S., Chu, Z., Chrzanowski, W., & Li, Q. (2017). Shape dependent cytotoxicity of PLGA-PEG nanoparticles on human cells. Scientific Reports, 7(1). https://doi.org/10.1038/s41598-017-07588-9

Zhang, F., Miao, Y., Liu, Q., Li, S., & He, J. (2020). Changes of pro-inflammatory and anti-inflammatory macrophages after peripheral nerve injury. RSC Advances, 10(64), 38767–38773. https://doi.org/10.1039/d0ra06607a

Zhang, J., Huang, L., Ge, G., & Hu, K. (2023). Emerging Epigenetic-Based Nanotechnology for Cancer Therapy: Modulating the Tumor Microenvironment. Advanced Science, 2206169. https://doi.org/10.1002/advs.202206169

Zhang, W., Cao, S., Liang, S., Tan, C. H., Luo, B., Xu, X., & Saw, P. E. (2020). Differently Charged Super-Paramagnetic Iron Oxide Nanoparticles Preferentially Induced M1-Like

Phenotype of Macrophages. Frontiers in Bioengineering and Biotechnology, 8. https://doi.org/10.3389/fbioe.2020.00537

Zhang, W., Wang, F., Hu, C., Zhou, Y., Gao, H., & Hu, J. (2020). The progress and perspective of nanoparticle-enabled tumor metastasis treatment. In Acta Pharmaceutica Sinica B (Vol. 10, Issue 11, pp. 2037–2053). Chinese Academy of Medical Sciences. https://doi.org/10.1016/j.apsb.2020.07.013

Zhang, Y., & Zhang, Z. (2020). The history and advances in cancer immunotherapy: understanding the characteristics of tumor-infiltrating immune cells and their therapeutic implications. In Cellular and Molecular Immunology (Vol. 17, Issue 8, pp. 807–821). Springer Nature. https://doi.org/10.1038/s41423-020-0488-6

Zhao, X., Ng, S., Heng, B. C., Guo, J., Ma, L., Tan, T. T. Y., Ng, K. W., & Loo, S. C. J. (2013). Cytotoxicity of hydroxyapatite nanoparticles is shape and cell dependent. Archives of Toxicology, 87(6), 1037–1052. https://doi.org/10.1007/s00204-012-0827-1

Zhuang, J., Kuo, C. H., Chou, L. Y., Liu, D. Y., Weerapana, E., & Tsung, C. K. (2014). Optimized metal-organic-framework nanospheres for drug delivery: Evaluation of small-molecule encapsulation. ACS Nano, 8(3), 2812–2819. https://doi.org/10.1021/nn406590q

Zou, D., & Liu, D. (2019). Understanding the modifications and applications of highly stable porous frameworks via UiO-66. In Materials Today Chemistry (Vol. 12, pp. 139–165). Elsevier Ltd. https://doi.org/10.1016/j.mtchem.2018.12.004

Appendix

Appendix 1. NanoDrop Spectrophotometer results from the different RNA extractions

Table A1. Total RNA concentration and purity assessed by NanoDrop Spectrophotometer.

Samples	24 h incubation		48 h incubation	
	Concentration (µg/ul)	$A_{260/280}$	Concentration (µg/ul)	$A_{260/280}$
Positive Control -1	313.59	2.13	944.57	2.14
Positive Control -2	204.37	2.15	1294.81	2.11
Positive Control -3	382.98	2.11	1284.69	2.13
Needle -1	258.72	2.12	358.79	2.05
Needle -2	309.83	2.13	316.93	2.07
Needle -3	223.06	2.14	734.09	2.08
Square -1	278.91	2.14	917.06	2.12
Square -2	337.56	2.13	1372.81	2.11
Square -3	300.18	2.12	426.23	2.07
Spherical -1	375.49	2.13	1170.90	2.09
Spherical -2	413.08	2.12	1105.22	2.11
Spherical -3	254.89	2.15	928.68	2.12
Hexagon -1	292.03	2.11	856.36	2.13
Hexagon -2	330.65	2.12	1067.02	2.13
Hexagon -3	269.57	2.15	1032.28	2.11

Appendix 2. Calibration curves for ELISA assay

Calibration graph	Concentration range (µg/mL)	Calibration curve (y=mx+b)	r^2
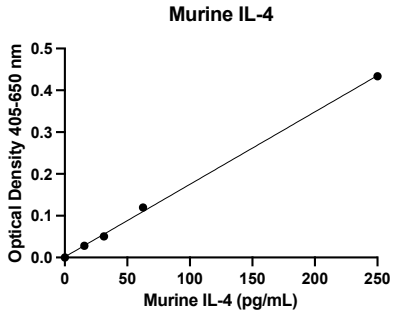	[0;250]	m=0.0017 b=0.0018	0.9989
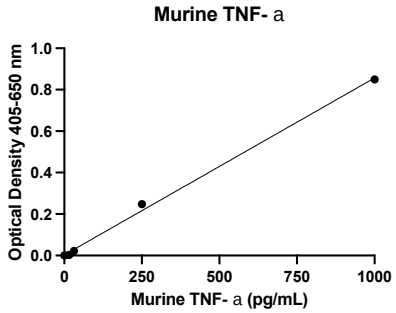	[0;1000]	m=0.0009 b=0.0030	0.9976
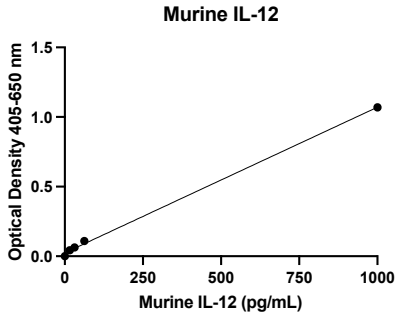	[0;1000]	m=0.0010 b=0.0247	0.9988
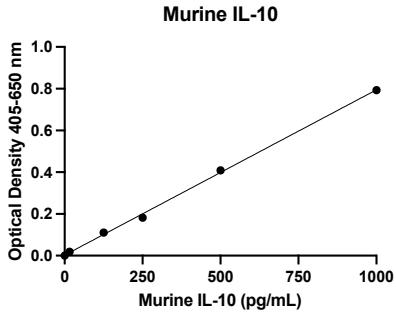	[0;1000]	m=0.0008 b=0.0028	0.9988

Figure A1. Calibration curves for ELISA assay.